RSC Advances

REVIEW

View Article Online
View Journal | View Issue

Cite this: *RSC Adv.*, 2015, **5**, 52269

Methodologies for evaluation of metal–organic frameworks in separation applications†

Rajamani Krishna

Metal–organic frameworks (MOFs) offer considerable potential for separating a wide variety of mixtures. For any given separation, there are several MOFs that could be employed. Therefore, there is a need for reliable procedures for screening and ranking MOFs with regard to their anticipated performance in fixed-bed adsorbers, commonly used in industry. Such fixed-bed adsorbers are invariably operated in a transient mode. The separation performance of fixed-bed adsorbers is governed by a number of factors that include adsorption selectivity, uptake capacity, and intra-crystalline diffusion limitations. We undertake a detailed analysis of the separations of several mixtures that include: C_2H_2/CO_2, CO_2/N_2, CO_2/CH_4, $H_2S/CO_2/CH_4$, $H_2/CO_2/CO/CH_4/N_2$, Xe/Kr, C_2H_2/C_2H_4, C_2H_4/C_2H_6, C_3H_6/C_3H_8, O_2/N_2, N_2/CH_4, hexane isomers, xylene isomers, and styrene/ethylbenzene. For each separation, we compare the performance of a few carefully selected MOFs by using transient breakthrough simulations that are representative of practical operations. These case studies demonstrate that screening MOFs on the basis of adsorption selectivity alone, as is common practice, often leads to wrong conclusions as regards their separation capability in fixed-bed adsorbers. High uptake capacities often compensate for low selectivities. Conversely, low uptake capacities diminish the separation performance of MOFs with high selectivities. Intra-crystalline diffusion limitations lead to distended breakthroughs, and diminished productivities in a number of cases. We also highlight the possibility of harnessing intra-crystalline diffusion limitations to reverse the adsorption selectivity; this strategy is useful for selective capture of nitrogen from natural gas, and in air separations.

Received 29th April 2015
Accepted 8th June 2015

DOI: 10.1039/c5ra07830j

www.rsc.org/advances

1 Introduction

There is increasing research on the synthesis and development of new materials such as metal–organic frameworks (MOFs), and zeolitic imidazolate frameworks (ZIFs) for use as adsorbents in a wide range of separation applications. These materials could offer significant improvements in separation performance as compared to traditionally used adsorbents such as zeolites, and activated carbon. In industrial processing operations, the microporous materials are normally used in

Van 't Hoff Institute for Molecular Sciences, University of Amsterdam, Science Park 904, 1098 XH Amsterdam, The Netherlands. E-mail: r.krishna@contact.uva.nl; Fax: +31 20 525 5604; Tel: +31 20 627 0990

† Electronic supplementary information (ESI) available: This material provides salient structural details of all the adsorbent materials that are evaluated for any specific separation application, along with references to data sources for unary isotherms. Also included as ESI are video animations for transient breakthroughs for every mixture investigated. See DOI: 10.1039/c5ra07830j

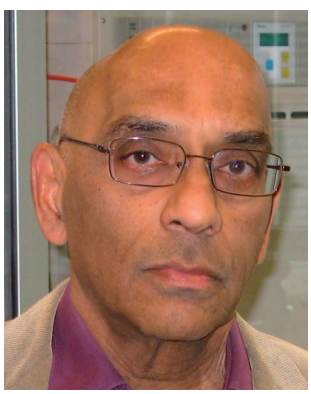

Rajamani Krishna is a Professor at the University of Amsterdam in the Netherlands. His current research focus is on adsorption and diffusion in nanoporous crystalline materials. He has published two text books, 450 peer-reviewed journal articles, and holds several patents. A complete list of his research contributions can be found on Google Scholar: http://scholar.google.nl/citations?user=cKqtQ0MAAAAJ&hl=en. According to the latest statistics on Google scholar, his publications have been cited more than 23 000 times, with an h-index of 80. He is the recipient of the prestigious 2013 ENI award for his research theme Improving Process Technologies with Molecular Insights.

powder or pelleted form in fixed bed adsorbers. Such units are most commonly operated in a transient mode, with adsorption and desorption cycles; they are called either pressure swing adsorbers (PSA) or temperature swing adsorbers (TSA) depending on the regeneration strategy employed. The separation performance of PSA and TSA units are governed by a wide variety of factors that include adsorption selectivity, uptake capacity, and intra-crystalline diffusion.[1] The costs of regeneration are linked, *inter alia*, to the cycle times, and the heats of adsorption.

For any given separation application, it may be possible to identify the microporous material with the ideal pore size, and surface area that offers the right degree of interactions (van der Waals, electrostatic, π-electron exchange) with the guest molecules. In comparison to traditionally used porous materials such as zeolites, MOFs and ZIFs offer significantly higher surface areas and porosities. As illustration, Fig. 1 presents data for surface areas, pore volumes, framework densities, and characteristic channel dimensions of some representative zeolites, MOFs and ZIFs. The commonly used NaX zeolite, for example, has a characteristic size (window aperture) of 7.4 Å, pore volume of 0.28 $cm^3\ g^{-1}$, and surface area of 950 $m^2\ g^{-1}$. Significantly higher surface areas are available with MOFs; for example CuBTC has an area of 2100 $m^2\ g^{-1}$. The accessible pore volumes of MOFs are commonly in the 0.5–2 $cm^3\ g^{-1}$ range. The pore dimensions of MOFs are often significantly larger than for zeolites; NiMOF-74, for example, has one-dimensional (1D) hexagonal-shaped channels of approximately 11 Å.

Framework flexibility has, in most cases, a negligible influence on the adsorption and diffusion characteristics of zeolites;[2] this is because zeolite frameworks are constructed with strong covalent bonds that are rigid.[3] On the other hand, many MOFs, and ZIFs possess soft "dynamic" frameworks that may undergo guest-induced structural changes; such transformations can be exploited to achieve selective separations.[4,5]

MOFs can be synthesized to yield 1D triangular-shaped channels;[6,7] this channel geometry is not feasible with zeolites. Unique separation possibilities emerge; for example, 1,3,5-tri-chlorobenzene (TCB) can be selectively separated from its isomers due to optimum face-to-face stacking within the triangular channels;[8] see Fig. 2. Separations using MOFs with bespoke-tailored triangular channels for separation of TCB isomers may be difficult to surpass with regard to separation performance.

To set the scene for this article, let us consider the separation of $C_2H_2(1)/CO_2(2)$ mixtures. This separation is important in industry for production of pure C_2H_2, that is required for a variety of applications in the petrochemical and electronic industries.[9] The separation is particularly challenging in view of the similarity in the molecular dimensions.[9,10] Both molecules possess zero dipole moments and approximately the same quadrupole moment. The polarizability of C_2H_2 is slightly higher than that CO_2. On the basis of available data on unary isotherms, we conclude that four MOFs have the potential of being applied in this separation task: HOF-3 (a rod-packing 3D microporous hydrogen-bonded organic framework),[11] CuBTC (=$Cu_3(BTC)_2$ with BTC = 1,3,5-benzenetricarboxylate, also

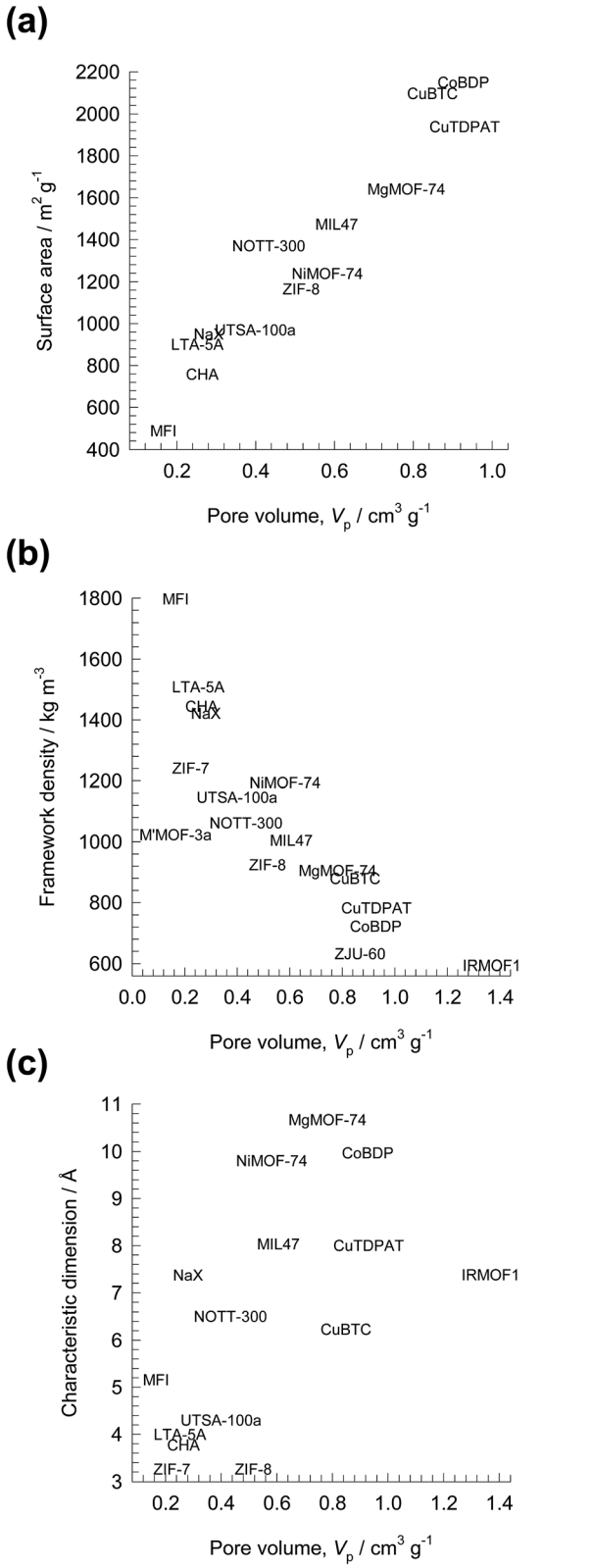

Fig. 1 Comparison of surface area, pore volumes, framework densities, and characteristic dimensions of some representative zeolites, MOFs and ZIFs.

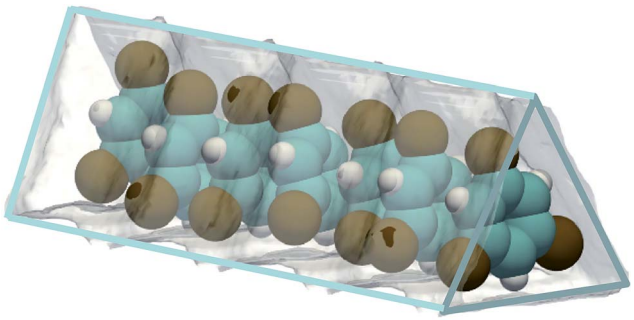

Fig. 2 Snapshot showing face-to-face stacking of 1,3,5-trichlorobenzene (TCB) within the triangular channels of $Fe_2(BDP)_3$.[8]

known as HKUST-1),[11] ZJU-60a (=Cu_2(MFDI)),[12] and PCP-33.[13] All four MOFs can selectively adsorb ethyne. With HOF-3, the preferential adsorption of ethyne over CO_2 is attributed to the unique pockets and pore surfaces.[11] The coordinatively unsaturated Cu(II) sites of CuBTC exert stronger interactions with C_2H_2 than with the O atoms of CO_2.[10]

As is commonly done in evaluating the separation performance of MOFs, let us determine the adsorption selectivity, S_{ads}, defined for separation of a binary mixture of species 1 and 2 by

$$S_{ads} = \frac{q_1/q_2}{p_1/p_2} \quad (1)$$

where the q_i represent the molar loadings of component i within the porous material that is in equilibrium with a bulk gas phase with partial pressures p_i. The S_{ads} values can be estimated using pure components isotherm fits, along with the Ideal Adsorbed Solution Theory (IAST) of Myers and Prausnitz[14] for binary adsorption equilibrium. It should be noted that the applicability of the IAST is restricted to cases in which there is a homogenous distribution of adsorbate species throughout the microporous framework. The IAST predictions will fail when segregation or clustering effects are present. Examples of segregated adsorption include preferential siting of CO_2 at the window regions,[15–17] or preferential location at the intersections of network of channels.[18] Hydrogen bonding between polar molecules may lead to cluster formation and the failure of the IAST.[19]

Fig. 3a presents IAST estimates of S_{ads} for separation of 50/50 C_2H_2/CO_2 mixtures. The hierarchy of S_{ads} values is HOF-3 > CuBTC ≈ ZJU-60a ≈ PCP-33, suggesting HOF-3 as the best choice. The performance of PSA units is also dictated by the uptake capacity. The component loading of C_2H_2, q_1, can be determined from IAST; see Fig. 3b. The hierarchy of uptake capacities, expressed as the number of moles of C_2H_2 adsorbed per L of adsorbent, is CuBTC > PCP-33 > ZJU-60a > HOF-3.

The costs of regenerating the adsorbed C_2H_2 may be related to the heat of adsorption; Fig. 3c is a plot of the isosteric heats of adsorption, Q_{st}, as a function of loading. We note that the hierarchy in the Q_{st} values is CuBTC > PCP-33 > ZJU-60a ≈ HOF-3. Since the selectivity, capacity, and Q_{st} metrics do not go hand-in-hand, the question arises: how do we weigh the three metrics in an appropriate manner? The primary objective of this review

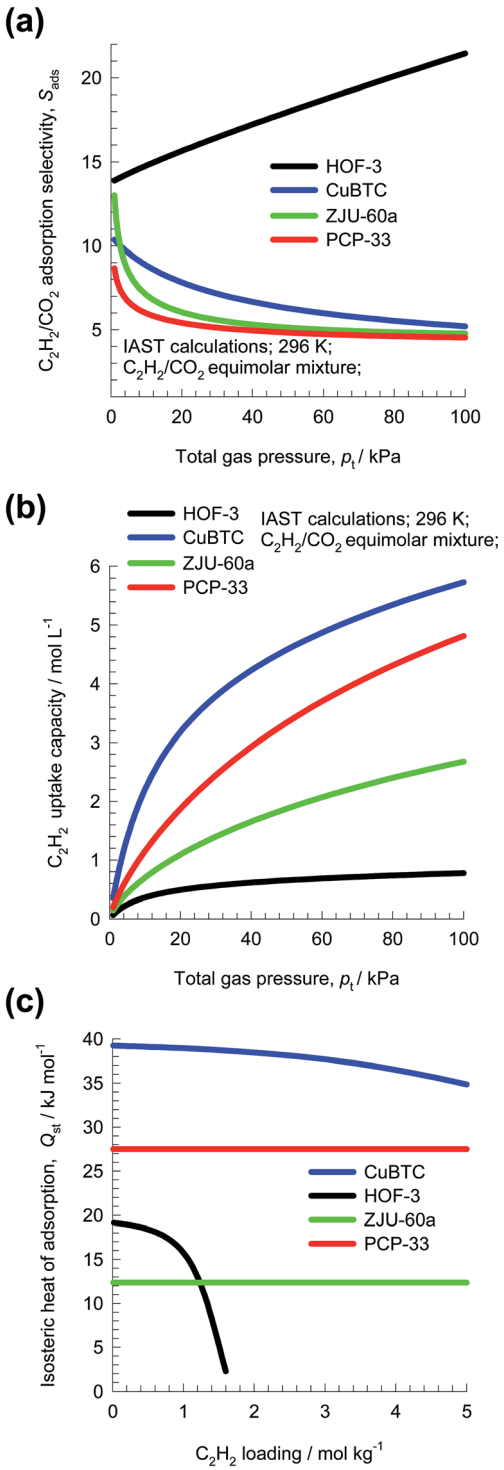

Fig. 3 (a and b) IAST calculations of (a) adsorption selectivity, S_{ads}, and (b) uptake capacity of C_2H_2, for separation of 50/50 C_2H_2/CO_2 mixture at 296 K using HOF-3, CuBTC, ZJU-60a, and PCP-33. (c) Comparison of the isosteric heat of adsorption of C_2H_2 in four MOFs.

is to discuss methodologies for arriving at a rational choice of the best adsorbent for a specified separation task.

When the number of components in the mixture exceeds two, it is often not obvious, *a priori*, how the S_{ads} and capacity metrics need to be defined for a meaningful comparison of

MOFs. For example, the production of pure H_2 from steam-methane reformer off-gas requires separation of $H_2/CO_2/CO/CH_4/N_2$ mixtures. The purity requirement of H_2 is stringent, and less than 500 ppm of impurities can be tolerated. The impurity level will be dictated primarily by the sequence of breakthroughs of the exit gas from the fixed bed adsorber; this sequence is not known *a priori*. The separation of hexane isomers (*n*-hexane (*n*C6), 2-methylpentane (2MP), 3-methylpentane (3MP), 2,2-dimethylbutane (22DMB), and 2,3-dimethylbutane (23DMB)) for the purpose of octane enhancement is another example for which the definition of selectivity is not meaningful because the objective is to produce high octane product from the adsorber; sharp separations are not demanded. The secondary objective of this review is to examine and analyze a number of multicomponent mixture separations in order to suggest procedures that need to be adopted in such cases.

The ESI† accompanying this article provides salient structural details of all the adsorbent materials that are evaluated for any specific separation application, along with references to data sources for unary isotherms. For any given separation application, the adsorbent materials have been carefully chosen to highlight a number of issues that are important in selection of the right adsorbent.

2 C_2H_2/CO_2 separations

Fig. 4 shows a schematic of fixed bed adsorber for C_2H_2/CO_2 mixture separations. Transient breakthrough simulations were performed to analyze the separations, using the methodology described in earlier works;[20,21] the simulation details are summarized in the ESI.† The validity of the breakthrough simulation methodology has been established by detailed comparisons with experimental data for a wide variety of guest/host combinations.[21–26] For all the simulations reported in this article we choose: adsorber length, $L = 0.3$ m; cross-sectional area, $A = 1$ m^2; superficial gas velocity in the bed, $u = 0.04$ m s^{-1}; voidage of the packed bed, $\varepsilon = 0.4$. The volume of MOF used in the simulations is $(1-\varepsilon)AL$. If ρ is the framework density, the mass of the adsorbent in the bed is $\rho(1-\varepsilon)AL$ kg. For presenting the breakthrough simulation results, we use the dimensionless time, $\tau = \frac{tu}{L\varepsilon}$, obtained by dividing the actual time, t, by the characteristic time, $\frac{L\varepsilon}{u}$.

For a 50/50 mixture feed to a bed packed with PCP-33 operating at a total pressure of 100 kPa and 298 K, the transient development of concentrations of CO_2, and C_2H_2 along the length of the adsorber are shown in Fig. 4b and c. The gas phase concentration of the more poorly adsorbed CO_2 traverses the bed faster than the more strongly adsorbed C_2H_2. Particularly noteworthy are the concentration overshoots for CO_2 during the early stages of the transience. To get a better appreciation of the transient behaviors, video animations are provided as ESI;† these video animations are constructed from the data such as those plotted in Fig. 4b and c. Analogous video animations for the other separations, to be discussed later, are also available as ESI.†

In transient breakthrough experiments, the gas phase concentrations can only be monitored at the exit of the adsorber. It is customary, therefore, to present the transient breakthroughs in the form shown in Fig. 5a. Here, the normalized gas phase concentrations, c_i/c_{i0}, monitored at the exit of the adsorber (at position $z = L$) is plotted as a function of the dimensionless time, τ.

During the initial transience, the effluent gas contains pure CO_2 and this continues until C_2H_2 starts breaking through because its uptake capacity within the MOF has been reached. Fig. 5b presents a comparison of the % C_2H_2 in the exit gas for beds packed with HOF-3, CuBTC, ZJU-60a, and PCP-33. In these breakthrough simulations, as with all other simulations in this article, we use the same volume of adsorbent in the breakthrough apparatus, *i.e.* $(1-\varepsilon)AL$. Since the framework densities of the three MOFs are different (HOF-3: $\rho = 453$; CuBTC: $\rho = 879$; ZJU-60a: $\rho = 631$; PCP-33: $\rho = 1261$ kg m^{-3}), the masses of adsorbents are also different. We note that the CuBTC and PCP-33 breakthroughs occur significantly later than the breakthroughs for HOF-3 and ZJU-60a. Delayed breakthroughs are desirable because increased amounts of C_2H_2 can be captured in each cycle. CuBTC has the longest breakthrough time primarily because of its significantly higher C_2H_2 uptake capacity (*cf.* Fig. 3b). The earlier breakthrough with HOF-3 is attributable to its low uptake capacity.

Let us define the breakthrough time, τ_{break}, as the time at which the exit gas contains <0.05% = 500 ppm C_2H_2. The value of τ_{break} is lowest for HOF-3, despite the fact that it has the highest selectivity. The amount of C_2H_2 captured during the time interval $0 - \tau_{break}$ can be determined from a material balance. These amounts, expressed as mol C_2H_2 captured per L of framework material are plotted against τ_{break} in Fig. 5c. We note that the amount of C_2H_2 captured is linearly dependent on τ_{break}. On the basis of this comparison, we conclude that CuBTC has the best separation capability.

Let us turn to regeneration energy requirements. The isosteric heat of adsorption, Q_{st}, can be considered to be representative of regeneration energy required per mole of captured C_2H_2. Fig. 5d plots the amount of C_2H_2 captured against Q_{st}. The high capture capacity of CuBTC needs to be weighed against the higher regeneration costs. Detailed costing is required to arrive at the final choice of MOF; such an exercise is beyond the scope of this article. Since CuBTC is a commercially available MOF, it may still end up as the most cost-effective option.

The important message that emerges from this case study C_2H_2/CO_2 mixture separations is that high uptake capacities can overcome the disadvantage of low selectivities, resulting in good separations in fixed beds. Also, low values of the isosteric heats of adsorption, Q_{st}, will not necessarily reduce regeneration energy requirements if the attendant capture capacities are low.

A further point to note is that the water and chemical stability aspects have only been investigated for PCP-33,[13] and CuBTC.[27,28]

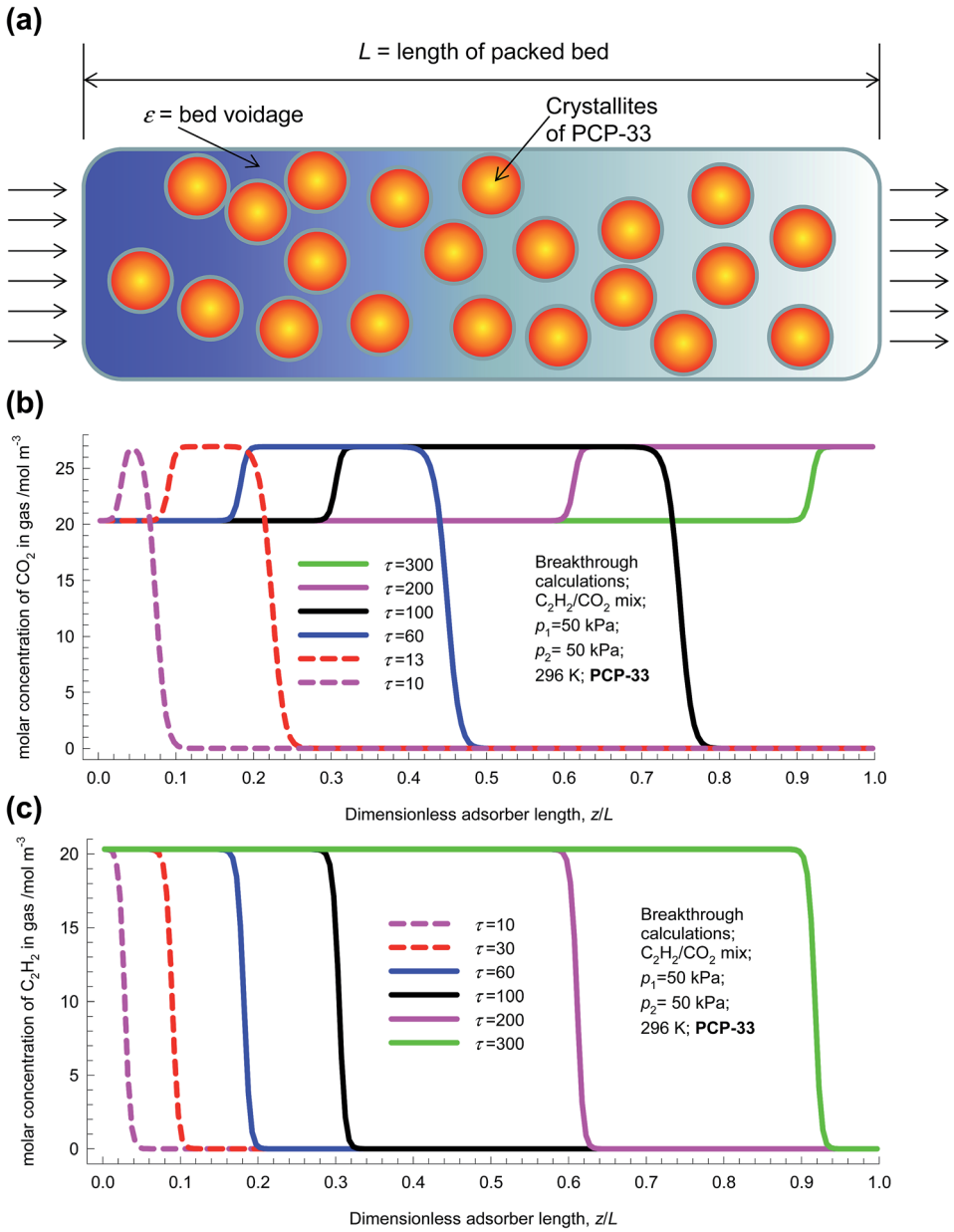

Fig. 4 (a) Schematic of fixed bed adsorber for C_2H_2/CO_2 mixture separations. (b and c) Transient development of concentrations of (b) CO_2, and (c) C_2H_2 along the length of the fixed bed adsorber.

3 Xe/Kr separations

The recovery of noble gases such as Xe and Kr from used nuclear fuels is an important industrial problem.[29] Fig. 6a presents data on the kinetic diameters and polarizabilities, α, of noble gases (He, Ne, Ar, Kr, Xe). The value of α generally increases with increasing molar mass, because more electrons are available for polarization; see Fig. 6a. As illustration of the efficacy of MOFs for separation of noble gases, Fig. 6b presents pulse chromatographic simulations for separation of a 5-component He/Ne/Ar/Kr/Xe mixture in a fixed bed of CuBTC. The times at which each of the component pulses peak correlates with the corresponding polarizability of the noble gas; see Fig. 6b. Pulse chromatographic simulations and experiments are representative of separations in the Henry regime at low pore occupancies.[30,31]

Let us now examine the separation of Xe/Kr mixtures in more detail. In the published literature, a number of MOFs have been developed with the potential for application in the Xe/Kr separation process. Wang *et al.*[32] demonstrate the highly selective adsorption of Xe in CoFormate ($=Co_3(HCOO)_6$), that is attributed to its commensurate positioning of Xe within the cages. This commensurate positioning also implies that the intracrystalline diffusivity of Xe will be significantly lower than that of Kr.[29,33,34] The experimental breakthroughs reported by Wang *et al.*[32] for 10/90 Xe/Kr mixtures in a bed packed with CoFormate are shown in Fig. 7a. The experimental breakthrough of Xe has a distended character; this indicates strong diffusion limitations.

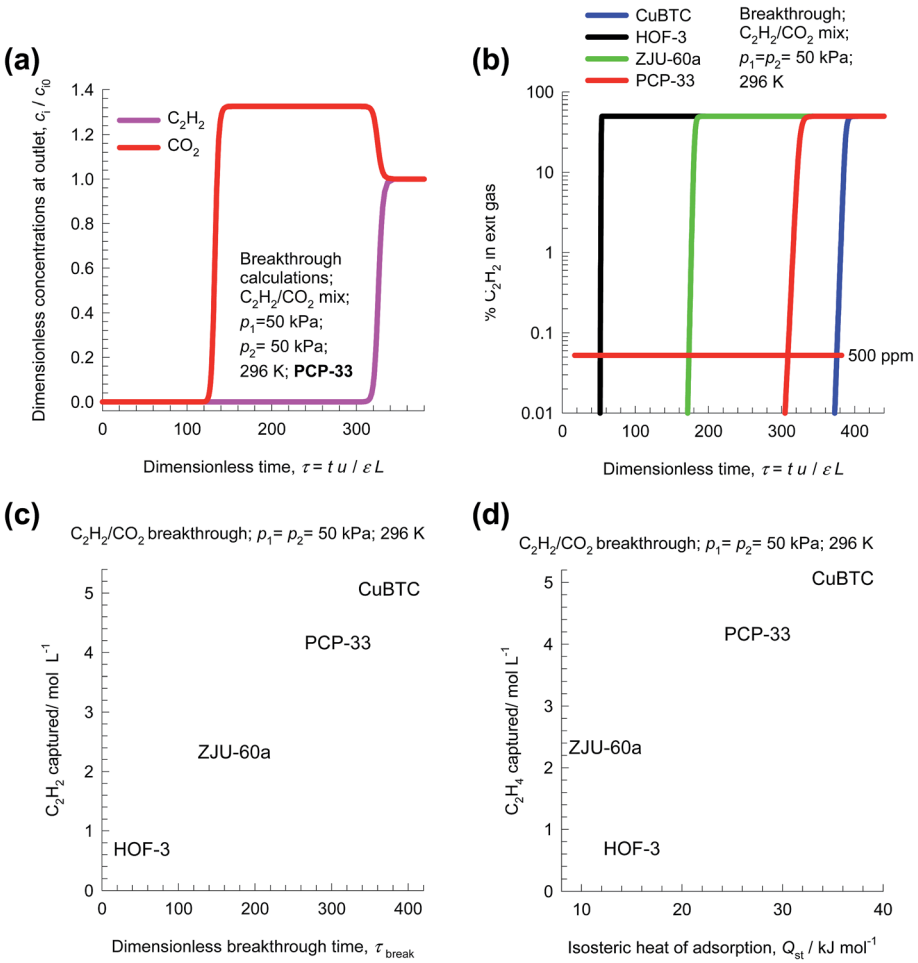

Fig. 5 (a) Transient breakthrough of C_2H_2/CO_2 mixture separations in a bed packed with PCP-33. (b) Comparison of % C_2H_2 in the exit gas for beds packed with HOF-3, CuBTC, ZJU-60a, and PCP-33 plotted as a function of the dimensionless time. (c) Comparison of the moles of C_2H_2 captured per L of material during the interval for which the product gas is 99.95% CO_2, plotted as a function of the dimensionless breakthrough time, τ_{break}. (d) Plot of the amount of C_2H_2 captured per L of material during the time interval 0 – τ_{break} *versus* the isosteric heat of adsorption.

Fig. 7b presents the transient breakthrough simulations using the data inputs corresponding to the experiments of Wang *et al.*[32] The experimental breakthroughs are reproduced, nearly quantitatively, by transient breakthrough simulations that include the influence of intra-crystalline effects with the chosen values $\mathcal{D}_{Xe}/r_c^2 = 2 \times 10^{-3}$ s^{-1}; $\mathcal{D}_{Kr}/r_c^2 = 1 \times 10^{-2}$ s^{-1}; here $\mathcal{D}_i$ is the intra-crystalline diffusivity, and r_c is the radius of the crystallites. We note that the diffusivity of Xe within the pores is a factor five lower than that of Kr because of the much more strongly confined Xe that adsorbs commensurately within the cages. If intra-crystalline diffusional influences are ignored and adsorption equilibrium is assumed to prevail at every position z, and any time t, we obtain the sharp breakthroughs represented by the dashed lines in Fig. 7b. The distended breakthrough of Xe has an impact on the separations, as we explain below.

Following the earlier works of Banerjee *et al.*,[29] and Chen *et al.*,[35] let us compare the separation performance of CoFormate with four other MOFs: NiMOF-74 (ref. 36 and 37) Ag@NiMOF-74,[37] CuBTC,[36,38] and SBMOF-2.[35] Fig. 8a presents a comparison the S_{ads} values for 20/80 Xe/Kr mixtures as a function of the total gas pressure $p_t = p_1 + p_2$. We note that the hierarchy of S_{ads} is CoFormate > Ag@NiMOF-74 > NiMOF-74 > SBMOF-2 > CuBTC. The introduction of well-dispersed Ag nanoparticles into NiMOF-74, results in stronger interactions of the polarizable Xe with the adsorbent Ag@NiMOF-74. The geometry of the channels of SBMOF-2 provides a better match for the larger Xe atoms rather than smaller Kr, and helps explain the selectivity for Xe over Kr.

Let us compare the separation of 20/80 Xe/Kr mixtures in fixed beds packed with the four MOFs. The transient breakthrough simulations for NiMOF-74, Ag@NiMOF-74, SBMOF-2, and CuBTC assume thermodynamic equilibrium because the influence of diffusional limitations are established to be of negligible importance.[29] For CoFormate the breakthrough simulations include intra-crystalline diffusion effects with the diffusivity values that are chosen to match the published breakthrough experimental data in Fig. 7.[29] On the basis of the outlet gas compositions, we can determine the ppm Xe in the exiting gas as a function of the dimensionless time, τ; see Fig. 8b. Let us assume that the desired product Kr should have a purity corresponding to 1000 ppm Xe. Corresponding to this

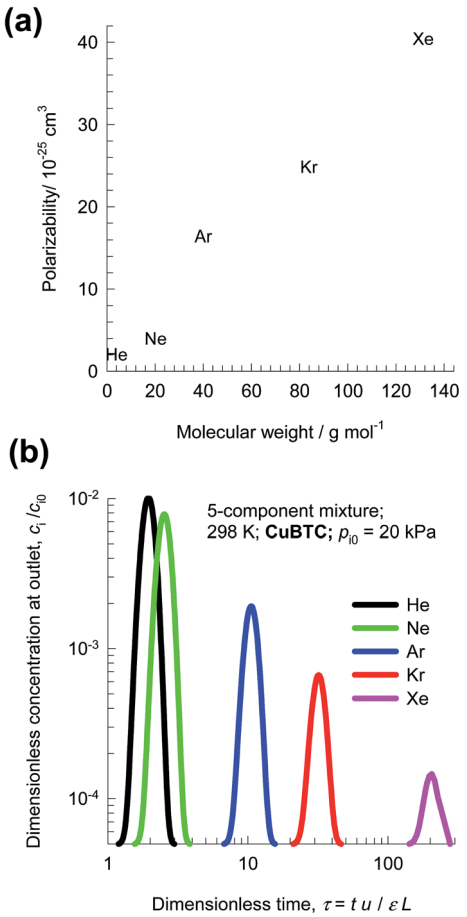

Fig. 6 (a) Comparison of molar masses, kinetic diameters, boiling points and polarizabilities of noble gases (He, Ne, Ar, Kr, Xe). (b) Pulse chromatographic simulations for separation of a 5-component mixture of noble gases He/Ne/Ar/Kr/Xe in a fixed bed of CuBTC operating at 298 K and a total pressure of 100 kPa.

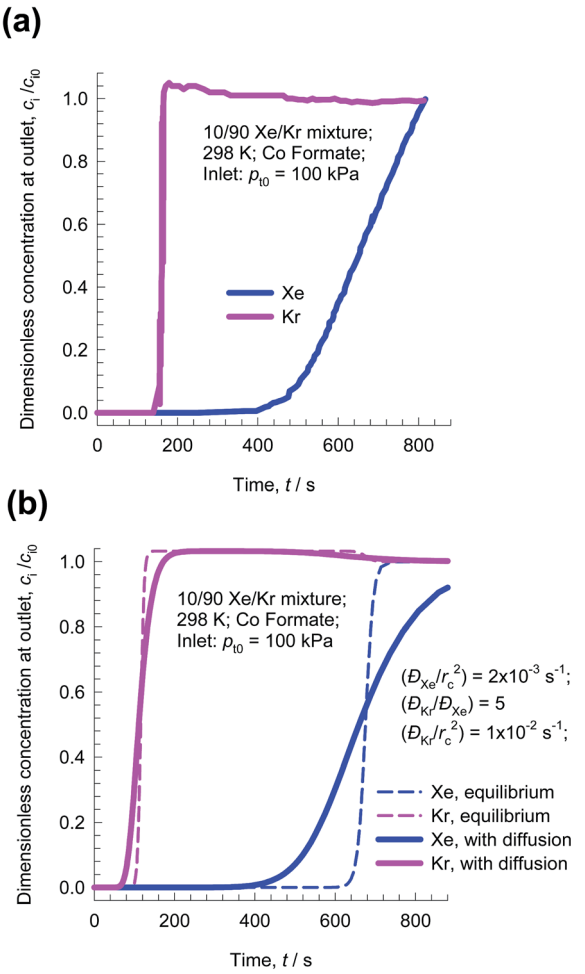

Fig. 7 (a) Experimental breakthroughs for 10/90 Xe/Kr mixtures at 298 K and 100 kPa in a bed packed with CoFormate; the data are scanned from Fig. S9 of the ESI† accompanying the paper by Wang *et al.*[32] (b) Simulations without intra-crystalline diffusion limitations (*i.e.* equilibrium between bulk gas and crystal at any location and indicated by dashed lines) are compared with breakthrough simulations that include intra-crystalline diffusion effects. The chosen diffusivity values are $Đ_{Xe}/r_c^2 = 2 \times 10^{-3}\ s^{-1}$; $Đ_{Kr}/r_c^2 = 1 \times 10^{-2}\ s^{-1}$.

purity requirement we can determine the dimensionless breakthrough time, τ_{break}, at which the operation of the fixed bed needs to be stopped and regeneration started to recover pure Xe. From a material balance, we can determine the productivity of Kr during the time interval $0 - \tau_{break}$. The productivities, expressed as mol of pure Kr produced per L of MOF are plotted in Fig. 8c as a function of the dimensionless breakthrough time, τ_{break}. The MOF with the highest productivity is Ag@NiMOF-74. Despite having the highest adsorption selectivity, CoFormate has a productivity that is significantly lower than that of Ag@NiMOF-74. The reasons for the lower productivity of CoFormate are two-fold: (a) lower uptake capacity, and (b) strong diffusional limitations.

This case study on Xe/Kr separations highlights the negative influence of intra-crystalline diffusion effects in CoFormate, leading to diminished capture capacities in fixed bed adsorbers.

4 CO_2/N_2 separations

For CO_2 capture from flue gas, typically containing 15% CO_2, and 85% N_2,[39] we can rely on selective CO_2 binding with extra-framework cations (*e.g.* Na^+, K^+, Ca^{++}, Ba^{++}) of zeolites NaX, LTA-4A, and LTA-5A. With MOFs, selective CO_2 binding could, for example, achieved with M^{2+} of M_2(dobdc) [Mg, Mn, Co, Ni, Zn, Fe, Cu, Mg] or M^{2+} of $M_3(BTC)_2$ [M = Cu, Cr, Mo]. Wu *et al.*[40] have established that the O atoms of CO_2 bind with the Mg atoms of MgMOF-74 (see Fig. 9a), with an associated binding energy of about 42 kJ mol^{-1}. Fig. 9b compares the isosteric heat of adsorption of CO_2 in six different adsorbents. The stronger the CO_2 binding, the higher is the selectivity in favor of CO_2 in separations.

Fig. 9c presents the IAST calculations of S_{ads} for separation of 15/85 CO_2/N_2 mixtures at 298 K using five different adsorbents: MgMOF-74,[39] NiMOF-74,[41] NaX zeolite,[42] Kureha carbon,[26] and Cu-SSZ13.[43] Kureha carbon exhibits the lowest CO_2/N_2 selectivity. The high selectivities of MgMOF-74, and NiMOF-74 are attributable to the strong binding of CO_2 with open metal sites. The electrostatic interactions of CO_2 with the extra framework cations

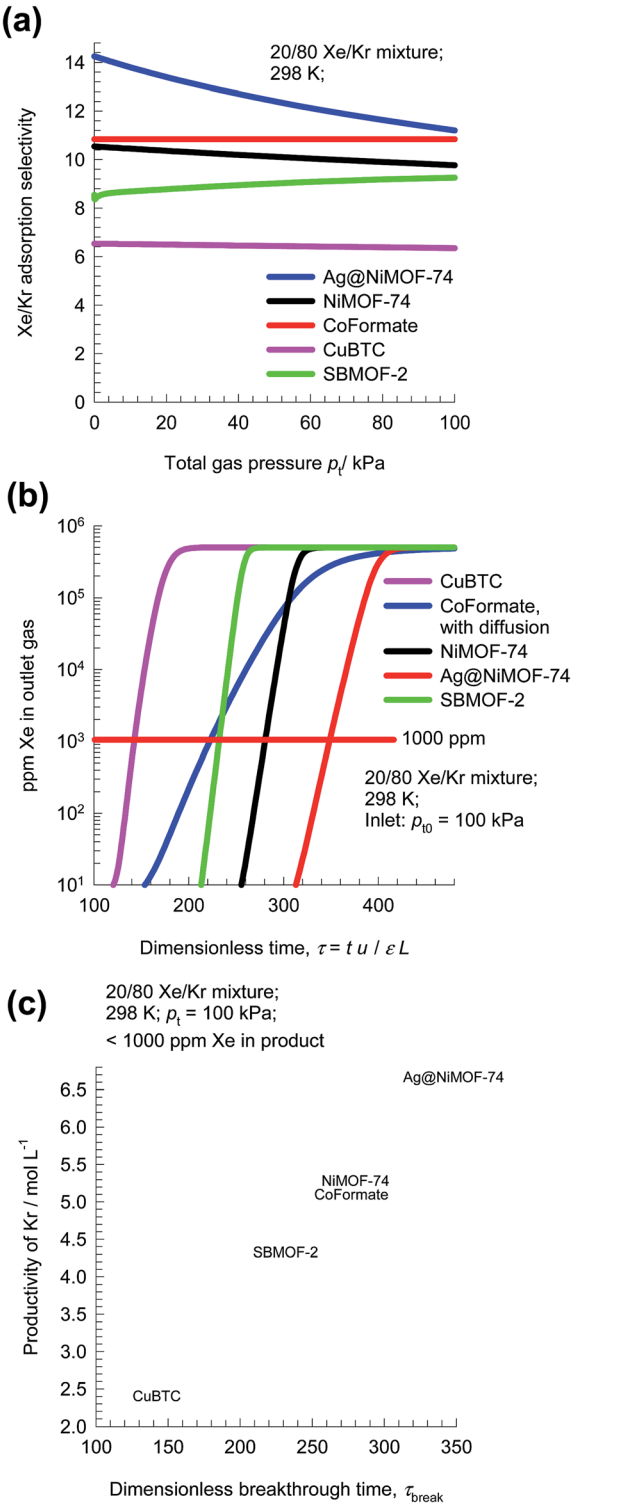

Fig. 8 (a) Comparison of adsorption selectivity, S_{ads}, for 20/80 Xe/Kr mixtures using NiMOF-74, Ag@NiMOF-74, CuBTC, SBMOF-2, and CoFormate as a function of the total gas pressure. (b) Ppm Xe in the outlet gas mixture of 20/80 Xe/Kr mixtures in fixed beds packed with five different MOFs, plotted as a function of the dimensionless time. (c) Dependence of the productivity of pure Kr (with <1000 ppm Xe), expressed in mol of product per L of MOF, as a function of the dimensionless breakthrough time, τ_{break}.

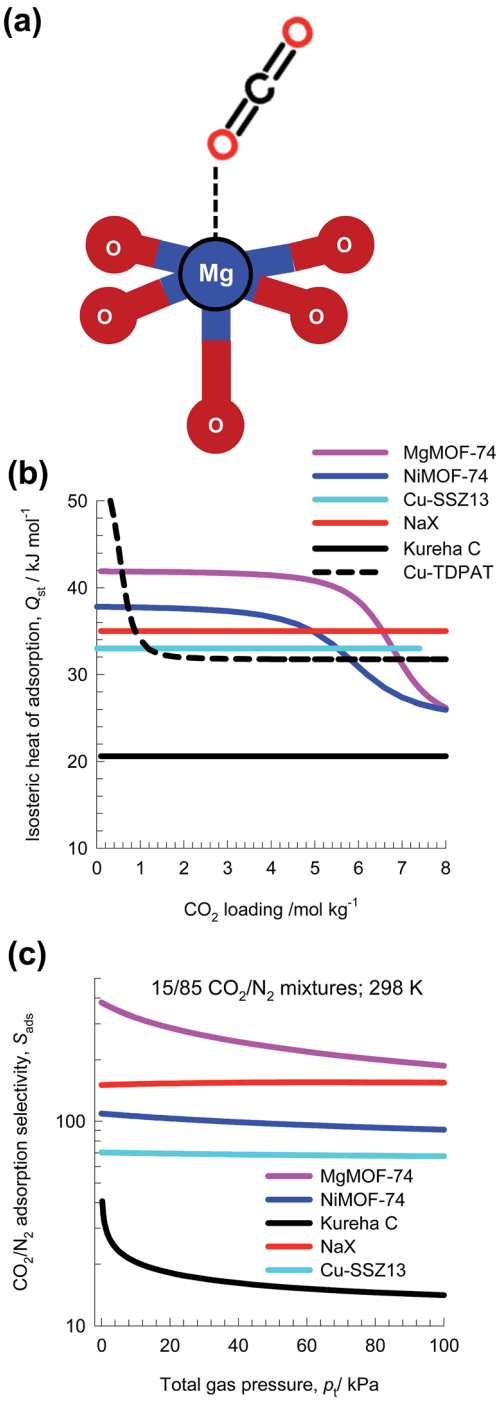

Fig. 9 (a) O atom of CO_2 binds with metal atoms of MgMOF-74. (b) Isosteric heat of adsorption of CO_2 in six different adsorbents: MgMOF-74, NiMOF-74, NaX zeolite, Kureha carbon, Cu-SSZ13, and Cu-TDPAT. (c) IAST calculations of adsorption selectivity, S_{ads} for separation of 15/85 CO_2/N_2 mixtures at 298 K.

Na^+ and Cu^{2+} account for the high selectivities exhibited by NaX and Cu-SSZ13 zeolites. The hierarchy of S_{ads} is the same as the hierarchy of values of Q_{st} shown in Fig. 9b; this is to be expected.

Transient breakthrough simulations are carried out to determine the relative separations in fixed bed adsorbers. Intra-crystalline diffusion resistances are of negligible importance for

MgMOF-74, NiMOF-74, and NaX zeolites, that have characteristics pore dimensions larger than 7.4 Å. Detailed analyses of the breakthrough experimental data of Chen *et al.*[24] and Yu *et al.*[26] confirm that intra-particle diffusion limitations are of negligible for NiMOF-74 and Kureha carbon. The situation with Cu-SSZ13 zeolite is different; this cage-type zeolite has the CHA topology and consists of consists of 316 $Å^3$ sized cages separated by 3.8 Å × 4.2 Å sized windows. Inter-cage hopping of CO_2 and N_2 occurs one-at-a-time and is strongly limited by diffusion.[2,44] In order to underscore the influence of intra-crystalline diffusion on the separations in fixed beds, Fig. 10a presents two types of simulation results for Cu-SSZ13, both neglecting diffusion limitations (dashed lines) and taking intra-crystalline diffusional influences into account (continuous solid lines). Inclusion of diffusion influences results in distended breakthrough characteristics, causing significantly earlier breakthrough of the more strongly adsorbed CO_2. Consequently, the productivity of purified N_2 is significantly diminished.

Fig. 10b presents a comparison of % CO_2 in the exit gas for beds packed with the five different adsorbents. Let us arbitrarily define the breakthrough time, τ_{break}, as the time at which the exit gas contains <0.05% = 500 ppm CO_2. The amount of CO_2 captured during the time interval $0 - \tau_{break}$ can be determined from a material balance. These amounts, expressed as mol CO_2 captured per L of framework material, are plotted against τ_{break} in Fig. 10c. The CO_2 capture capacity of Cu-SSZ13 is only marginally higher than the value for Kureha carbon. The message emerging from the analysis of CO_2/N_2 mixtures is that for achieving high CO_2 capture capacities, it is of vital importance to avoid use of adsorbents with characteristic pore dimensions significantly smaller than say 7 Å. This implies that materials such as LTA-4A, LTA-5A, SAPO-34, DDR, and KFI zeolites are unlikely to be effective for use in fixed bed separations; such materials are more suitable in membrane constructs.[44,45]

In addition to capture of CO_2 from flue gases, other impurities such as SO_2 present in the flue gas mixture need to be removed along with CO_2. The hydroxyl groups within the 6.5 Å × 6.5 Å channels of NOTT-300 bind both CO_2 and SO_2 selectively.[46] Fig. 11 presents simulation of transient breakthroughs of 15/75/10 $CO_2/N_2/SO_2$ mixtures in fixed bed adsorber packed with NOTT-300. The breakthrough of SO_2 occurs much later than CO_2, indicating the much stronger binding of SO_2 as compared to CO_2; the SO_2/N_2 selectivity is not of major importance. The selection of adsorbents should be based primarily on CO_2/N_2 separation performance.

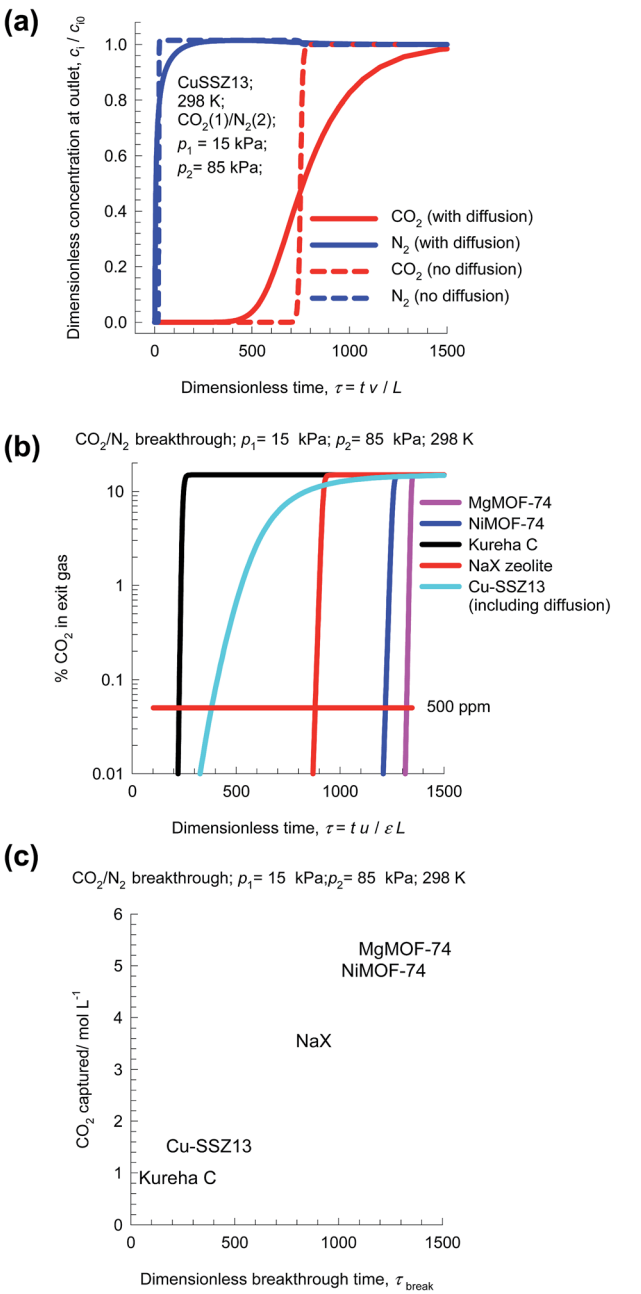

Fig. 10 (a) Transient breakthrough simulations for 15/85 CO_2/N_2 mixtures in CuSSZ-13, including intra-crystalline diffusional limitations (continuous solid lines), and ignoring diffusion (dashed lines). (b) Comparison of % CO_2 in the exit gas for beds packed with five different adsorbents, as a function of the dimensionless time. (c) Comparison of the moles of CO_2 captured per L of material during the interval for which the product gas is 99.95% N_2, plotted as a function of the dimensionless breakthrough time, τ_{break}.

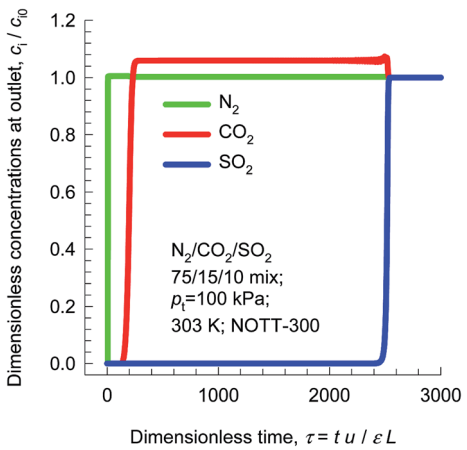

Fig. 11 Simulation of transient breakthroughs in fixed bed adsorber with input of 15/75/10 $CO_2/N_2/SO_2$ mixture using NOTT-300.

5 CO_2/CH_4 separations

Separation of CO_2 from CH_4 is relevant to the purification of natural gas, which can have up to 92% CO_2 impurity at its source.[47] Removal of CO_2, which is most commonly accomplished using amines, is conducted between 2 MPa and 7 MPa.[48] The separation requirements for production of liquefied natural gas (LNG) are rather stringent, often requiring the achievement of impurity levels of less than 500 ppm CO_2.

For separation of CO_2 from CH_4 at high pressures, uptake capacities are of paramount importance. To illustrate this, let us compare separations of 50/50 CO_2/CH_4 mixtures at 298 K using MgMOF-74, NiMOF-74, NaX zeolite, Kureha carbon, and Cu-TDPAT. The experimental isotherm data for Kureha carbon is available only for pressures up to 0.3 MPa;[26] consequently the selectivity and uptake capacities are calculated only up to a total pressure of 0.6 MPa. Fig. 12a presents IAST calculations of S_{ads}; the hierarchy of S_{ads} values is MgMOF-74 > NiMOF-74 $\approx$ NaX $\gg$ Cu-TDPAT > Kureha carbon. The CO_2 uptake capacity in 50/50 CO_2/CH_4 mixtures is plotted in Fig. 12b as a function of the total pressure p_t. For operations at pressure p_t < 100 kPa, the hierarchy of CO_2 uptake capacity is MgMOF-74 > NiMOF-74 > NaX > Cu-TDPAT > Kureha carbon. However, for p_t > 1 MPa, the hierarchy of CO_2 uptake capacity is MgMOF-74 > Cu-TDPAT > NiMOF-74 > NaX. The uptake capacity of NaX is severely limited due to its significantly lower pore volume than available with MOFs (*cf.* Fig. 1). Transient breakthrough simulations were carried out for fixed bed adsorbers operating at total pressures p_t = 100 kPa, and p_t = 2 MPa. The amount of CO_2 captured during the during the time interval $0 - \tau_{break}$, as a function of τ_{break} are presented in Fig. 12c and d. We define the breakthrough time, τ_{break}, as the time at which the outlet gas contains the arbitrarily chosen purity level of 500 ppm CO_2. We note that for operations at p_t = 100 kPa, the hierarchy of CO_2 captured is MgMOF-74 > NiMOF-74 $\approx$ NaX $\gg$ Cu-TDPAT > Kureha carbon, that is dictated by the uptake capacities plotted in Fig. 12b. However, for operations at p_t = 2 MPa, the hierarchy of CO_2 captured is MgMOF-74 > Cu-TDPAT > NiMOF-74 > NaX. The worst separation performance is with NaX; the diminished effectiveness of NaX at high pressures is due to capacity limitations. The higher uptake capacity of Cu-TDPAT, accounts for improved performance with increasing pressures. Generally

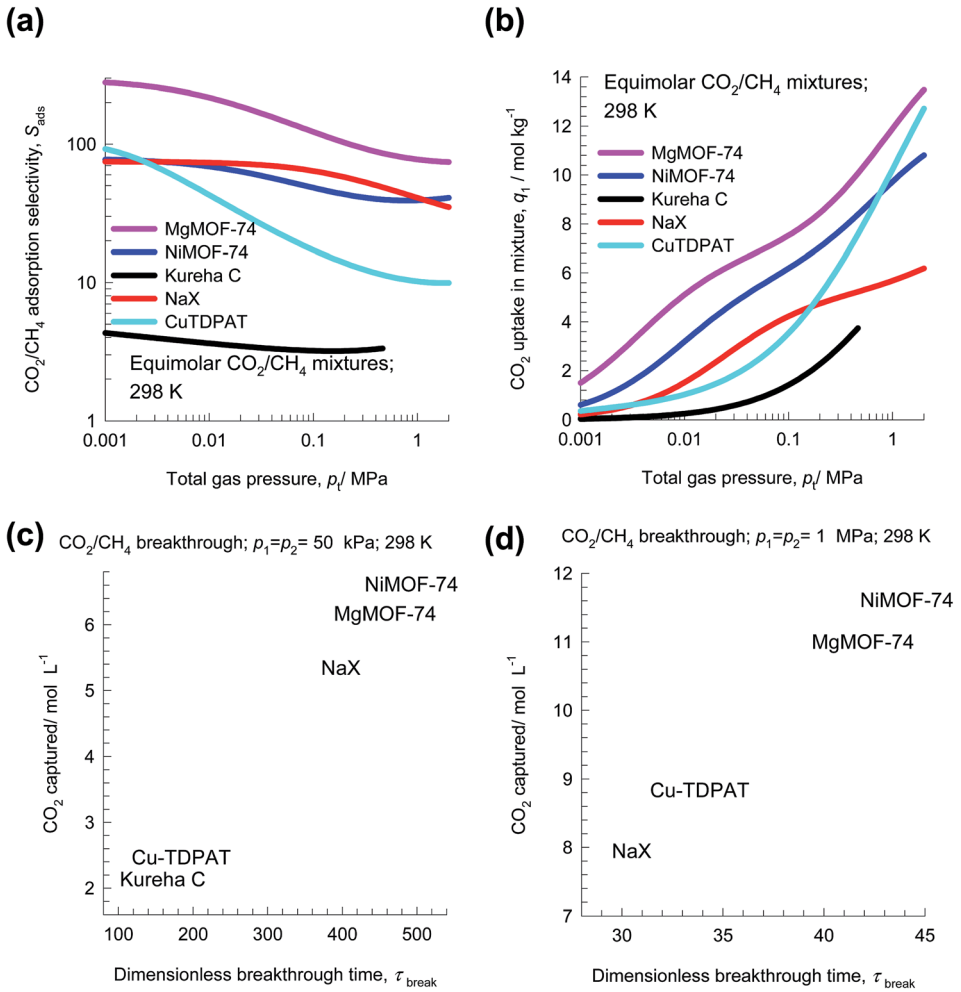

Fig. 12 (a and b) IAST calculations of (a) adsorption selectivity, S_{ads}, and (b) CO_2 uptake capacity of 50/50 CO_2/CH_4 mixture at 298 K using MgMOF-74, NiMOF-74, NaX zeolite, Kureha carbon and Cu-TDPAT. (c and d) Plots of the amount of CO_2 captured per L of material during the time interval $0 - \tau_{break}$ as function of the dimensionless breakthrough time, τ_{break}, for operations at (c) 100 kPa, and (b) 2 MPa.

speaking, MOFs with pore volumes in excess of say 0.9 $cm^3\ g^{-1}$ are desirable for CO_2/CH_4 separations at high pressures.

Plots such as those shown Fig. 5c, 8b, 10c, 12c and d are useful in selecting MOFs for a specified separation task. In these plots, the transient breakthrough simulations are performed under precisely the same set of conditions with respect to fixed bed dimension, flow rates, temperature, and inlet partial pressures of guest species. Under these conditions, the breakthrough times are representative of the capture capacities for the more strongly adsorbed component.

Such plots can also be constructed using experimental breakthroughs. However, it is unusual to find a set of experimental breakthroughs with different materials for the same set of operating conditions. We examine two available sets of data below; the ESI† contains details of the analysis of experimental breakthroughs.

Fig. 13a presents the experimental data of Li *et al.*[49] for % CO_2 in exit gas for breakthroughs of 40/60 CO_2/CH_4 mixtures in a fixed bed packed with five different adsorbents. The observed hierarchy of breakthroughs is Activated Carbon (AC) MIL-100(Cr), NiMOF-74, CoMOF-74, and MgMOF-74. The respective breakthrough times are representative of the CO_2 capture capacities; this data can be used to rank MOFs.

Another set of experimental breakthroughs are for 50/50 CO_2/CH_4 mixtures in bed packed with NiMOF-74 and Kureha carbon measured in the same set-up and reported by Chen *et al.*[24] and Yu *et al.*;[26] see Fig. 13b. The breakthrough with NiMOF-74 occurs at a significantly later time than Kureha carbon. From a material balance, we can determine the corresponding volumetric CO_2 capture capacities; see Fig. 13c. We note that the volumetric CO_2 capture capacity of NiMOF-74 is 3.5 times that of Kureha carbon. From the corresponding data determined from transient breakthrough simulations (presented in Fig. 12c), the ratio of the capture capacities of NiMOF-74 and Kureha carbon is 3.1. The closeness in the two sets of CO_2 capture capacity values is testimony to the accuracy of the transient breakthrough simulations in quantifying the separation capability of a MOF in fixed bed adsorbers. Indeed, the papers of Chen *et al.*[24] and Yu *et al.*[26] demonstrate good agreement of experimental breakthroughs with simulated breakthroughs for a wide range of temperatures and pressures.

Besides CO_2, other components such as H_2S are also present in small concentrations in natural gas; these also need to be adsorbed. The binding of H_2S with metal atoms of MOFs is much stronger than that with CO_2. Using NiMOF-74 as adsorbent, for example, the binding is between the S atoms with Ni atoms of NiMOF-74; see Fig. 14a. The stronger binding of H_2S with Ni atoms is reflected in a higher heat of adsorption that has a value of 60 kJ mol^{-1}, compared to the value of 38 kJ mol^{-1} for CO_2.[50]

The stronger binding of H_2S as compared to CO_2 has the consequence that the breakthrough of H_2S in a fixed bed adsorber packed with NiMOF-74 occurs significantly later than for CO_2. This is illustrated in Fig. 14b for transient breakthrough of 45/50/5 $CO_2/CH_4/H_2S$ mixtures in an adsorber packed with NiMOF-74, operating at 2 MPa and 298 K. Fig. 14c presents the corresponding results of the breakthroughs of $CO_2/CH_4/H_2S$ mixtures using amino-MIL-125(Ti) whose potential for this separation task has been established by Vaesen *et al.*[51] Since the objective is to obtain purified CH_4, the purity level will be dictated primarily by the breakthrough of CO_2, the first impurity to exit the adsorber. This implies that the separation of $CO_2/CH_4/H_2S$ mixtures can be treated as that for CO_2/CH_4 separations; there is no point in seeking materials with high

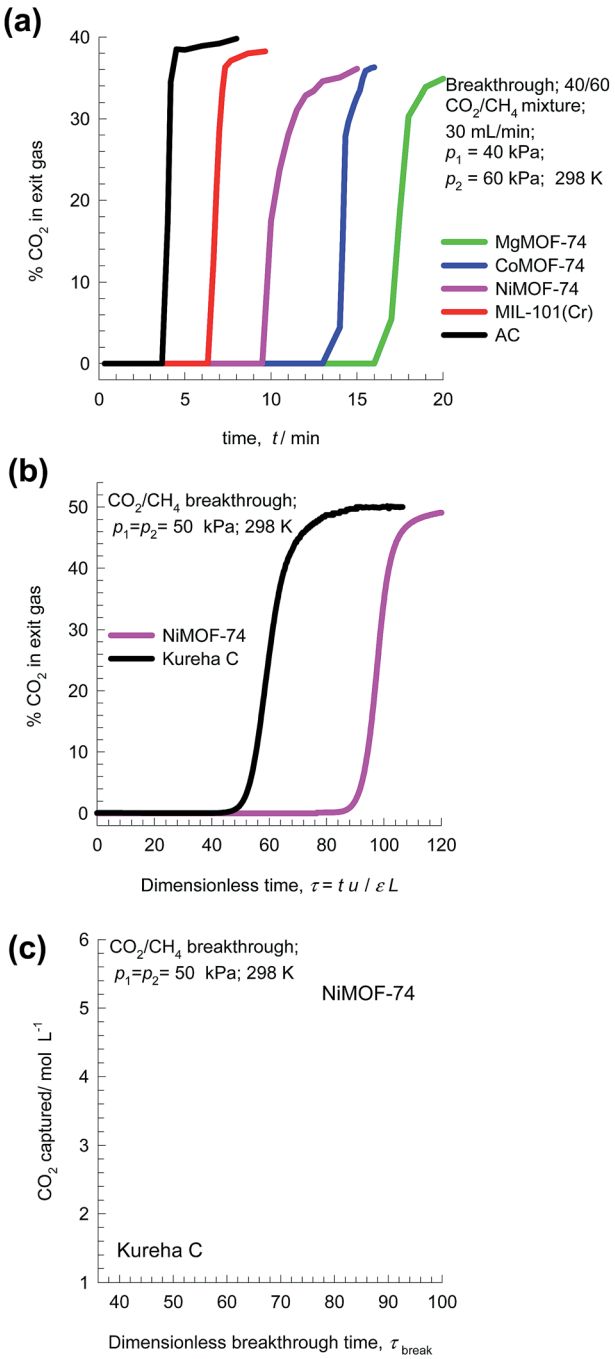

Fig. 13 (a) Experimental data of Li *et al.*[49] on the % CO_2 in exit gas for transient breakthroughs of 40/60 CO_2/CH_4 mixtures in a fixed bed packed with five different adsorbents MgMOF-74, CoMOF-74, NiMOF-74, MIL-100(Cr), and Activated Carbon (AC). (b and c) Experimental data of Chen *et al.*[24] and Yu *et al.*[26] for transient breakthroughs of CO_2/CH_4 mixtures in bed packed with NiMOF-74 and Kureha carbon. The inlet partial pressures are $p_1 = p_2 = 50$ kPa, and $T = 298$ K.

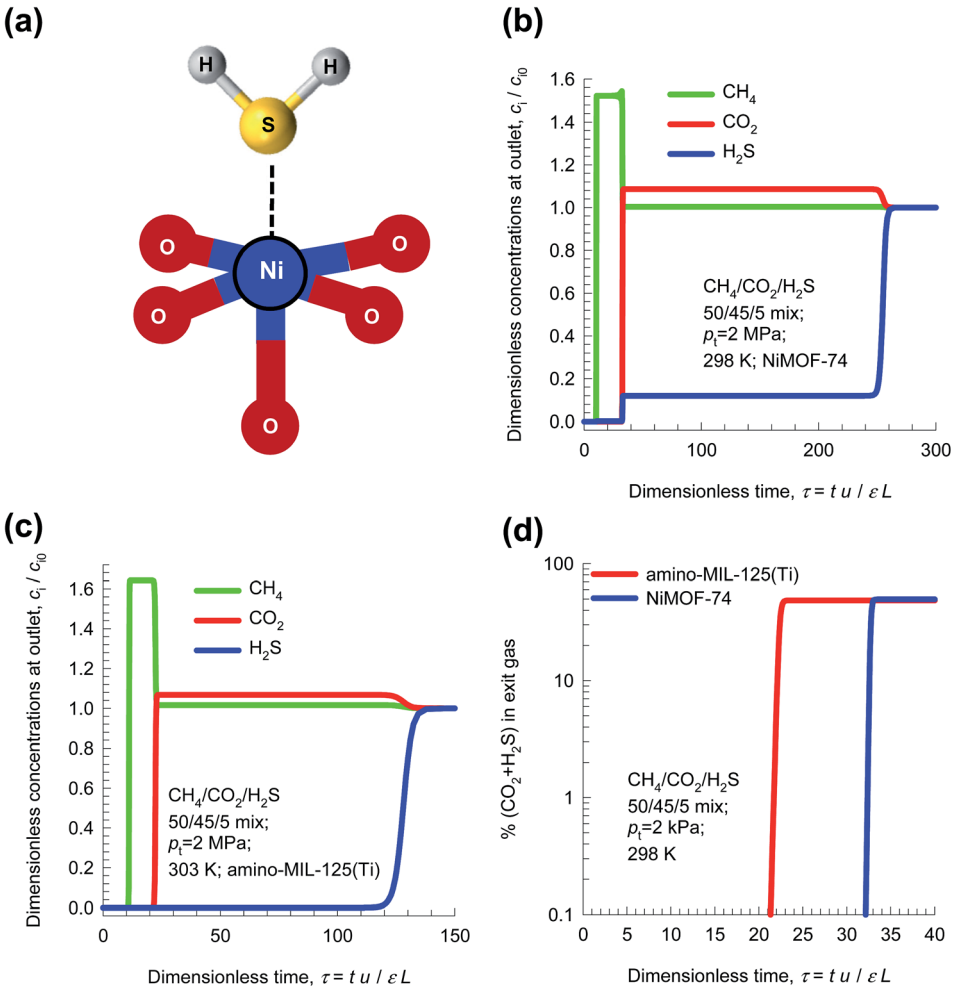

Fig. 14 (a) S atoms of H_2S bind with metal atoms of NiMOF-74.[50] (b and c) Simulation of transient breakthroughs in fixed bed adsorber with input of 45/50/5 $CO_2/CH_4/H_2S$ mixture using (b) NiMOF-74, and (c) amino-MIL-125(Ti). (d) Comparison of the % (CO_2 + H_2S) in outlet gas stream leaving fixed bed adsorber packed with NiMOF-74 and amino-MIL-125(Ti) as a function of the breakthrough time.

adsorption selectivity towards H_2S. Put another way, the H_2S/CH_4 selectivity is not of major importance. Fig. 14d presents a comparison of the % (CO_2 + H_2S) in outlet gas stream leaving fixed bed adsorber packed with either NiMOF-74 or amino-MIL-125(Ti). For both adsorbents, the purity level of CH_4 in the outlet gas is dictated by the breakthrough of CO_2. On the basis of this comparison we conclude that NiMOF-74 is the more effective adsorbent for separation of $CO_2/CH_4/H_2S$ mixtures.

The message emerging from the data presented in Fig. 11 and 14 is that for evaluation of MOFs, we need to identify the "key components" that determine multicomponent separations. In these two examples, the key components are, respectively, CO_2/CH_4 and CO_2/N_2 mixtures.

6 Separation of H_2 from $H_2/CO_2/CO/CH_4/N_2$ mixtures

Pressure swing adsorption is the most commonly used technology for recovery of pure hydrogen from a gaseous streams containing 60–90 mol% H_2.[52] Steam-methane reformer off-gas (SMROG), after it has been further treated in a water–gas shift reactor, is a commonly used feed gas stream, with typical compositions 70–80% H_2, 15–25% CO_2, 3–6% CH_4, 1–3% CO, and also containing some N_2.[52–54] The production of pure H_2 from steam-methane reformer off-gas requires operation of PSA units at pressures reaching about 5 MPa. Typically, H_2 is required with 99.95%+ purity. In fuel cell applications, the purity demands are as high as 99.999%.[55] In recent years there has been a considerable amount of research on the development of MOFs for use as adsorbents in PSA processes.[22,47,54,56]

Fig. 15a presents the breakthrough characteristics a 5-component 73/16/3/4/4 $H_2/CO_2/CO/CH_4/N_2$ mixture in an adsorber packed with Cu-TDPAT, and maintained at isothermal conditions at 298 K and total pressure of 0.7 MPa. The sequence of breakthroughs is: H_2, N_2, CH_4, CO, and CO_2. The sequence of breakthroughs in a fixed bed packed with UTSA-16a extrudates[57,58] is somewhat different: H_2, N_2, CO, CH_4, and CO_2; see Fig. 15b. The purity of H_2 in the product gas exiting the adsorber is primarily dictated by the presence of the less-strongly adsorbed N_2, CO, CH_4, rather than CO_2, that is the main

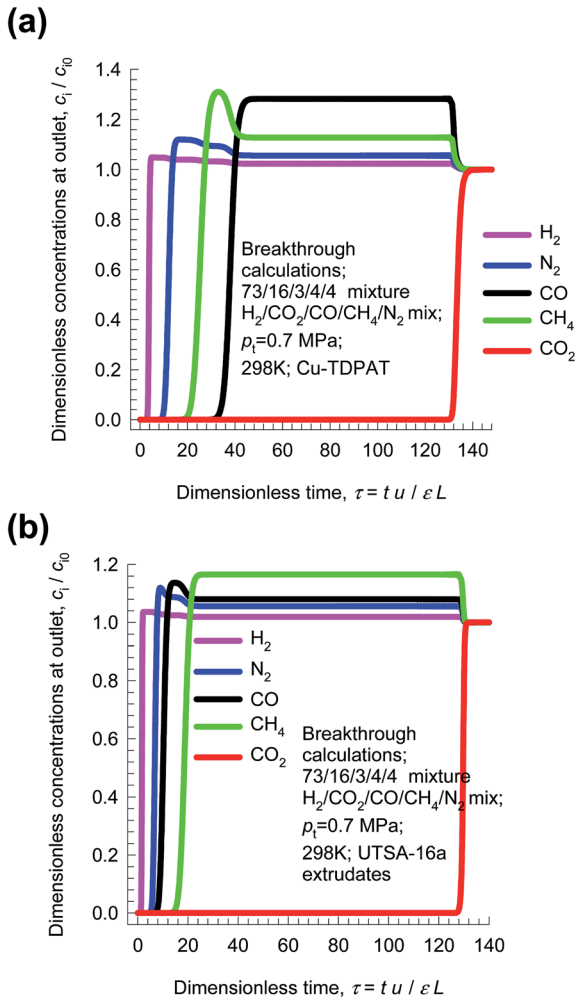

Fig. 15 Breakthrough characteristics of 5-component 73/16/3/4/4 $H_2/CO_2/CO/CH_4/N_2$ mixture in adsorber packed with (a) Cu-TDPAT, and (b) UTSA-16a and maintained at isothermal conditions at 298 K and total pressure of 0.7 MPa.

impurity in the feed gas mixture. The N_2/H_2, CO/H_2, CH_4/H_2 adsorption selectivities are far more relevant than the CO_2/H_2 selectivity. The proper methodology for comparing different adsorbents is to perform breakthrough calculations; simple IAST calculations of mixture adsorption equilibrium do not present the complete picture on separation capabilities.

From breakthrough calculations of the type shown in Fig. 15, we can compare different adsorbents by plotting the ppm (CO_2 + CO + CH_4 + N_2) in outlet gas as a function of the dimensionless time, τ, for various adsorbent materials. Fig. 16a compares the performance of four different adsorbents. We choose the impurity level to be 500 ppm (CO_2 + CO + CH_4 + N_2) in outlet gas; this is a typical requirement in industry. When this impurity level is reached, the corresponding dimensionless breakthrough time, τ_{break}, can be determined. The values of τ_{break} are largely dictated by the breakthrough time of the N_2, the "first" impurity that appears at the exit of the adsorber. NaX zeolite has the highest value of τ_{break}, implying that the bed can be run for a longer time before shutting down for regeneration. The productivity of purified H_2, with the desired purity level, correlates with τ_{break}; see Fig. 16b. Remarkably, the worst separation performance is with UTSA-16a, that emerged in the study of Xiang *et al.*[58] as a promising candidate for CO_2 capture.

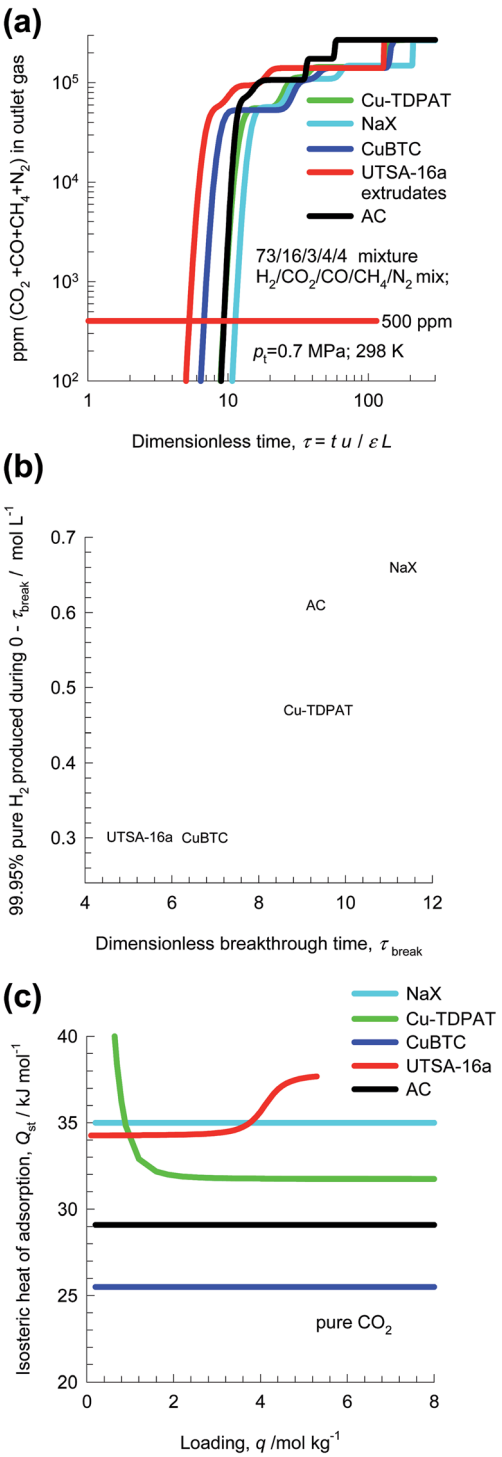

Fig. 16 (a) ppm (CO_2 + CO + CH_4 + N_2) in outlet gas as a function of the dimensionless time for separation of 5-component 73/16/3/4/4 $H_2/CO_2/CO/CH_4/N_2$ mixture using various adsorbent materials. (a) Plots of the amount of H_2 produced (<500 ppm impurities) per L of material during the time interval 0 – τ_{break} as function of the dimensionless breakthrough time, τ_{break}. (c) Isosteric heats of adsorption of CO_2 in different adsorbents.

This re-emphasizes the fact that best adsorbents for H_2 production do not need to be the best materials for CO_2 capture.

Fig. 16c compares the isosteric heats of adsorption of the four different adsorbents. It is likely that Activated Carbon (AC), could be also be a cost-effective option for H_2 production because this material is relatively cheap and has a low Q_{st} value, and separation performance only slightly lower than that of NaX zeolite. Indeed, Majlan *et al.*[55] have experimentally demonstrated that H_2 of purities demanded in fuel cell applications can be achieved in PSA units with activated carbon.

7 C_2H_2/C_2H_4 separations

In steam cracking of ethane to produce ethene, one of the by-products is ethyne, more commonly referred to as acetylene. Typically, the C_2H_2 content of C_2H_2/C_2H_4 feed mixtures is 1%. Ethyne has a deleterious effect on end-products of ethene, such as polyethene. Recovery, or removal of ethyne from ethene streams is essential because the presence of ethyne at levels higher than 40 ppm will poison the catalyst used for polymerization of ethene. The selective removal of ethyne is conventionally carried out by absorption in dimethyl formamide (DMF). A typical processing scheme involves three steps: (1) acetylene absorption in a tray column, (2) stripping of ethene from the solvent DMF, and (3) DMF regeneration with recovery of ethyne. Selective C_2H_2 adsorption using microporous materials affords an energy-efficient alternative. For example, ethyne binds more strongly than C_2H_4, with side-on attachment and π-coordination, with Fe^{2+} of FeMOF-74;[59,60] see Fig. 17a.

Fig. 17b compares the C_2H_2/C_2H_4 selectivities of seven different adsorbents. The adsorbents M′MOF-3a, and M′MOF-4a,[61] with a combination of metallo-ligands and organic ligands, have the highest selectivities. However, the C_2H_2 uptake capacity of M′MOF-3a, and M′MOF-4a is significantly

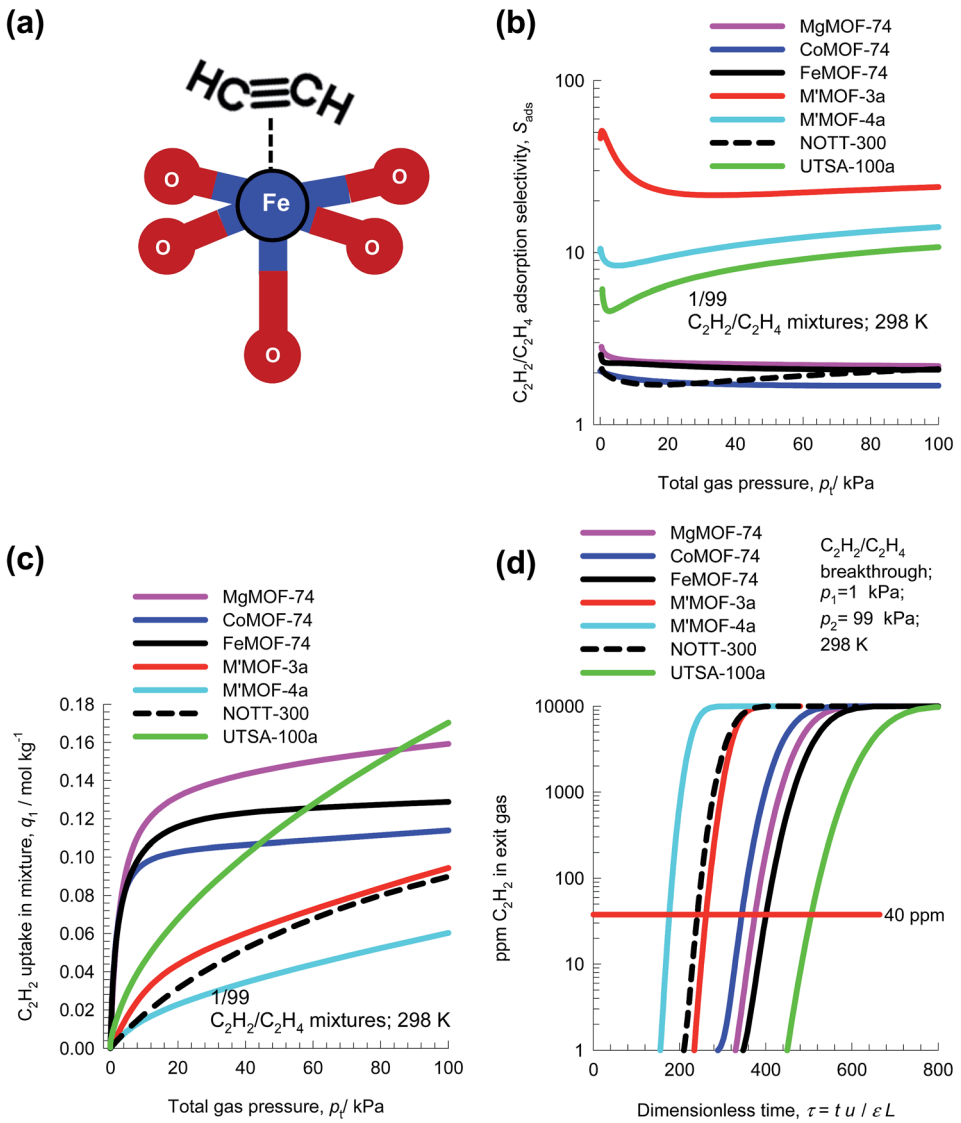

Fig. 17 (a) Side-on attachment of C_2H_2 with Fe^{2+} atoms of FeMOF-74. (b) IAST calculations of the adsorption selectivity, S_{ads}, of 1/99 C_2H_2/C_2H_4 mixtures using seven different MOFs. (c) C_2H_2 uptake capacity of 1/99 C_2H_2/C_2H_4 mixtures. (d) Comparison of % C_2H_2 in the exit gas from adsorber beds.

lower than that of M-MOF-74 and UTSA-100a;[62] see Fig. 17c. Due to capacity limitations, the breakthroughs with M′MOF-3a, and M′MOF-4a occurs earlier than with other adsorbents; see Fig. 17d. Delayed breakthroughs are desirable because increased amounts of C_2H_2 can be captured, and UTSA-100a[62] has the longest breakthrough time primarily because of its significantly higher C_2H_2 uptake capacity and selectivity.

Let us arbitrarily define the breakthrough time, τ_{break}, as the time at which the exit gas contains <40 ppm C_2H_2. The amount of C_2H_2 captured during the time interval $0 - \tau_{break}$ can be determined from a material balance. These amounts, expressed as mol C_2H_2 captured per L of framework material are plotted against τ_{break} in Fig. 18a. We note that the amount captured, is linearly dependent on τ_{break}. The C_2H_2 capture capacity is lowest for M′MOF-3a, despite the fact that it has the highest selectivity; the reason for its poor separation in the adsorber is its low uptake capacity.

Let us turn to regeneration energy requirements. The isosteric heat of adsorption, Q_{st}, can be considered to be indicative of regeneration energy required per mol of captured C_2H_2. Fig. 18a plots the C_2H_2 captured against Q_{st}. Remarkably, UTSA-100a has the highest capture capacity combined with the lowest value of Q_{st}. This is a desirable combination that makes UTSA-100a a good choice of adsorbent material.[62]

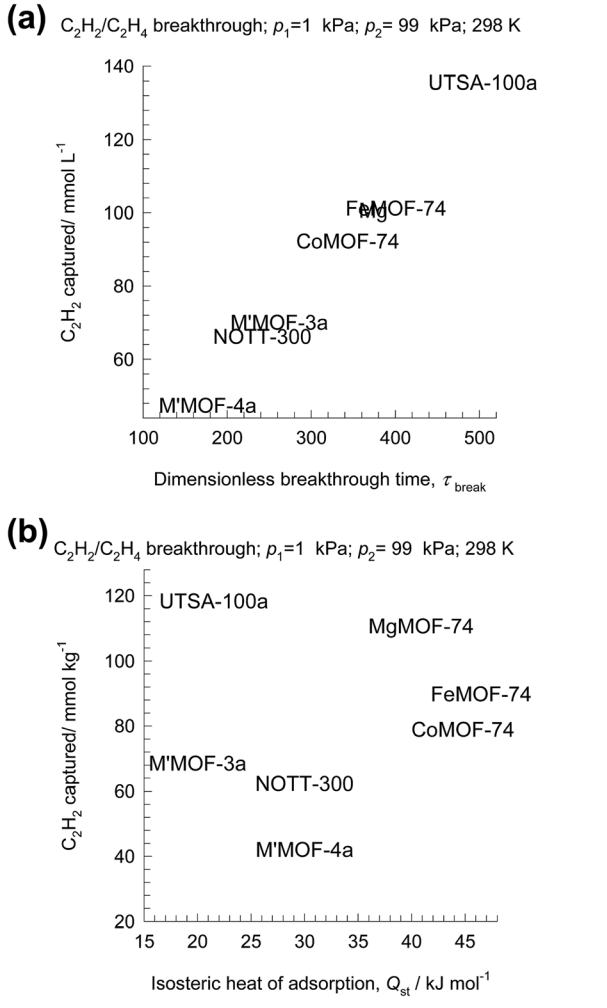

Fig. 18 (a) Plot of the amount of C_2H_2 captured per L of material during the time interval $0 - \tau_{break}$ as function of the dimensionless breakthrough time, τ_{break}. (b) Plot of the amount of C_2H_2 captured per L of material during the time interval $0 - \tau_{break}$ *versus* the isosteric heat of adsorption.

8 Alkene/alkane separations

Ethene is an important chemical used as feedstock in manufacture of polymers such as polyethene, polyvinyl chloride, polyester, polystyrene as well as other organic chemicals. Propene is an important chemical used as feedstock in manufacture of polymers such as polypropene. Key processing steps in preparing feedstocks for polymer production are the separations of ethene/ethane, and propene/propane mixtures. The boiling points are below ambient temperatures: ethane (184.5 K), ethene (169.4 K), propane (225.4 K), propene (225.4 K). Due to the small differences in the boiling points, the separations of ethene/ethane, and propene/propane mixtures have low relative volatilities, in the range of 1.1–1.2. These separations are traditionally carried out by distillation columns that operate at high pressures and low temperatures. The purity requirement of the alkenes as feedstocks to polymerization reactors is 99.95%, and consequently the distillation columns are some of the largest and tallest distillation columns used in the petrochemical industries. Several MOFs offer potential for separation of ethene/ethane and propene/propane mixtures, as alternatives to distillation.[59,63–68]

Let us now compare the performance of seven different MOFs for separation of 50/50 C_2H_4/C_2H_6 mixtures. The highest S_{ads} values are realized with the three recently reported MOFs: PAF-1-SO3Ag,[67] MIL-101-Cr-SO3Ag,[66] and NOTT-300;[68] see Fig. 19a. The π-complexation of the alkenes with Ag(I) ions of PAF-1-SO3Ag, and MIL-101-Cr-SO3Ag account for their high alkane/alkane selectivities. For FeMOF-74, Bloch *et al.*[59] have established that each alkene molecule attaches *side-on* to an Fe(II) atom in the FeMOF-74 framework. The volumetric uptake capacities for C_2H_4 of PAF-1-SO3Ag, MIL-101-Cr-SO3Ag, and NOTT-300 are, however, the lowest among the seven MOFs investigated; see Fig. 19b. The highest volumetric uptakes are obtained with FeMOF-74, and CoMOF-74. The separation performance in fixed bed adsorbers are best compared by plotting the % C_2H_4 in the exit gas from adsorber beds (Fig. 19c). Let us arbitrarily define the breakthrough time, τ_{break}, as the dimensionless time at which the % C_2H_4 in the exit gas is 1%. The breakthrough times, τ_{break}, are shortest with PAF-1-SO3Ag, MIL-101-Cr-SO3Ag, and NOTT-300; the longest breakthrough times are with FeMOF-74, and CoMOF-74 primarily because of their higher volumetric uptake capacities. Indeed, the hierarchy of breakthrough times is coincidental with the hierarchy of volumetric uptake capacities.

The amount of C_2H_4 captured during the time interval $0 - \tau_{break}$ can be determined from a material balance. These amounts, expressed as mol C_2H_4 captured per L of framework material are plotted against τ_{break} in Fig. 19d. The highest capture capacities are with FeMOF-74, and CoMOF-74; this is followed closely by MgMOF-74. The lowest C_2H_4 capture capacities are with PAF-1-SO3Ag, MIL-101-Cr-SO3Ag, and NOTT-300; the high

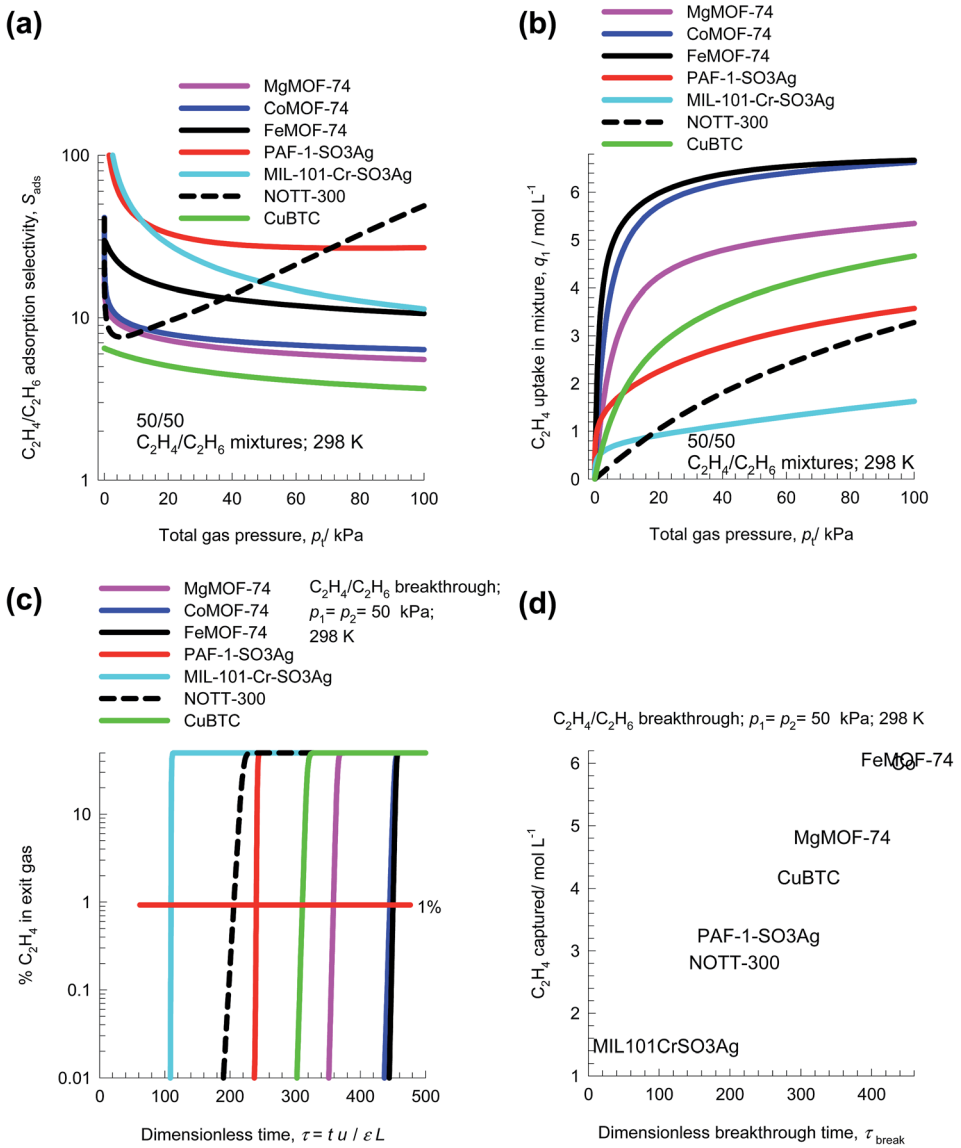

Fig. 19 (a and b) IAST calculations of (a) adsorption selectivity, S_{ads}, and (b) C_2H_4 uptake capacity in 50/50 C_2H_4/C_2H_6 mixtures at 298 K using seven different MOFs. (c) Comparison of % C_2H_4 in the exit gas from adsorber beds. (d) Plot of the amount of C_2H_4 captured per L of material during the time interval 0 – τ_{break} as function of the dimensionless breakthrough time, τ_{break}.

C_2H_4/C_2H_6 selectivities realized with these three MOFs are not able to compensate for their low uptake capacities.

The comparative evaluation of MOFs for C_3H_6/C_3H_8 separations[59,63–65] proceeds along similar lines; details are available in the ESI.† An important disadvantage of the alkane/alkene separations with the seven MOFs considered above is that the desired alkene product, required for production of polymer grade polyethene and polypropene, can only be recovered in the desorption phase. It becomes necessary to operate with multiple beds involving five different steps; the alkene product of the desired purity is recovered in the final step by counter-current vacuum blowdown.[69,70]

It is preferable to have use adsorbents that are selective to the saturated alkanes, so that the desired alkenes are recoverable in the adsorption cycle.[71] The preferential adsorption of alkanes is only possible if separations are based on van der Waals interactions alone. However, the adsorption selectivities cannot be expected to be high. Indeed, computational screening of 300 000 all-silica zeolite structures by Kim *et al.*[72] results in the discovery of SOF zeolite, that has a C_2H_6/C_2H_4 selectivity of only 2.9. This selectivity value of 2.9 can be matched by ZIF-7,[25,71] and ZIF-8.[73]

The separation of C4 hydrocarbon streams to recover the valuable 1,3-butadiene, 1-butene, and iso-butene by distillation is difficult and energy intensive.[30] There are potential savings to be realized by using adsorption technology with MOFs. Remarkably, however, this topic has not yet attracted the attention of MOF experimentalists.

9 N_2/O_2 separations

The separation of air to produce N_2 and O_2 of high purities is one of the most important industrial processes that uses

pressure swing adsorption technology.[1,74] The process technologies are geared to either production of purified O_2 or purified N_2. Cryogenic distillation has been the common technologies for this separation, but adsorptive separations offer energy-efficient alternatives. Purified O_2 is required for a wide variety of applications that include portable adsorption units for medical applications and in space vehicles. Nitrogen is required in applications where it is desired or necessary to exclude oxygen. Typical industrial applications include laser cutting, food packaging, and nitrogen blanketing. N_2 is required for use in laboratory analytical equipment, and in glove boxes.

Let us consider N_2/O_2 separations using LTA zeolite for which the all-silica form has a window size of approximately 4 Å. Fig. 20a and b present snapshots showing the location of cations in the industrially important LTA-5A (96Si, 96Al, $32Na^+$, $32Ca^{++}$, Si/Al = 1), and LTA-4A (96Si, 96Al, $96Na^+$, Si/Al = 1) zeolites. In LTA-4A, some of the Na^+ cations partially block the window regions,[2,33] thereby effectively reducing the aperture size that is available for inter-cage hopping of molecules. The Na^+ and Ca^{++} cations in LTA-5A, on the other hand, do not locate near the window regions and there is no blocking of the windows. This implies that diffusional influences are much stronger in LTA-4A than in LTA-5A zeolite.

Both O_2, and N_2 have similar polarizabilities and magnetic susceptibilities. However, the quadrupole moment of N_2 is about four times that of O_2. For both LTA-4A, and LTA-5A the

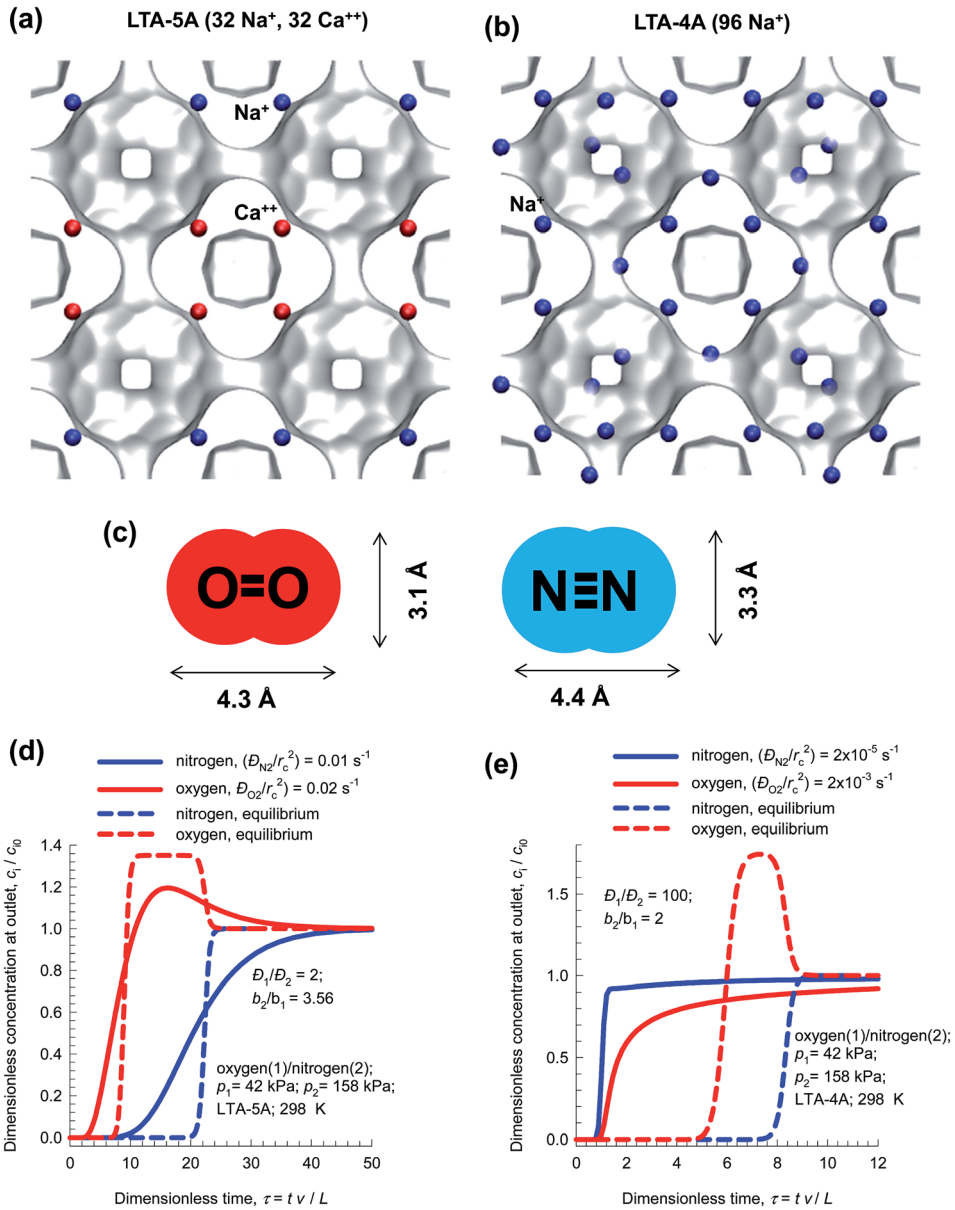

Fig. 20 (a and b) Snapshots showing the location of cations in (a) LTA-5A, and (b) LTA-4A. (c) Molecular dimensions of N_2 and O_2. (d) Influence of diffusional limitations on the breakthrough characteristics of O_2/N_2 mixture in a fixed bed adsorber packed with LTA-5A. (e) Influence of diffusional limitations on the breakthrough characteristics of O_2/N_2 mixture in a fixed bed adsorber packed with LTA-4A.

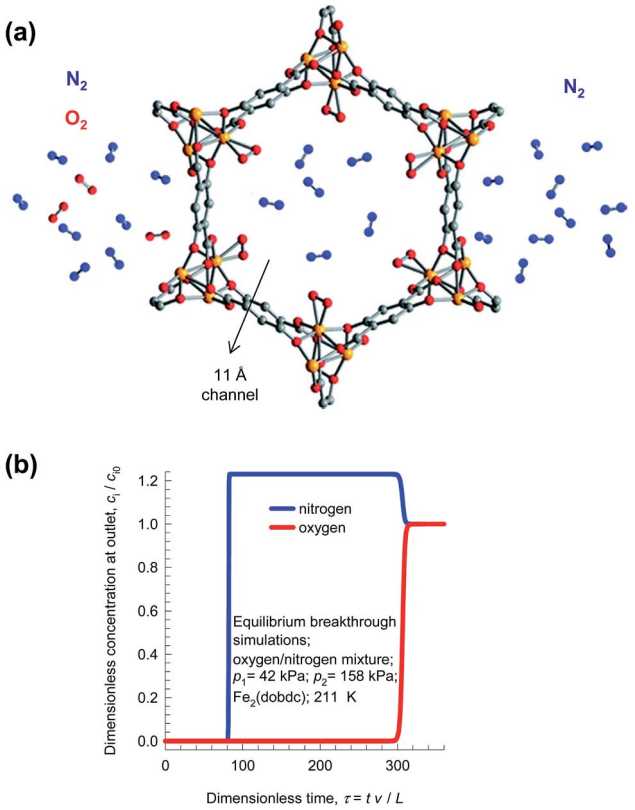

Fig. 21 (a) Selective binding of oxygen with Fe atoms of FeMOF-74; schematic adapted from Bloch *et al.*[75] (b) Simulations of the breakthrough characteristics of O_2(1)/N_2(2) mixture in a fixed bed adsorber packed with FeMOF-74 and operating at a total pressure of 200 kPa and 211 K. The partial pressures of the components in the bulk gas phase at the inlet are $p_1 = 42$ kPa, $p_2 = 158$ kPa.

adsorption selectivity is in favor of N_2. The diffusivity of N_2 is significantly lower than that of O_2 because of its larger cross-sectional dimension of 3.3 Å, compared to 3.1 Å for O_2; see Fig. 20c.

In LTA-5A zeolite, the ratio of the diffusivity of O_2 to that of N_2 is 2.[21] In a fixed bed adsorber with LTA-5A, O_2 breaks through earlier than N_2 because the separation is governed by thermodynamic equilibrium that overrides the diffusional effects; see Fig. 20d. Purified O_2 is the product emerging from the adsorption cycle of a fixed bed packed with LTA-5A.

Due to the reduced window aperture of LTA-4A, the ratio of the diffusivity of O_2 to that of N_2 is about 100. A fixed bed adsorber packed with LTA-4A produces pure N_2 in the adsorption phase of PSA operations; *i.e.* the separation is diffusion-selective; see Fig. 20e.

A better strategy for production of purified N_2, is to use an adsorption selective process in which the selective binding of O_2 to the Fe^{2+} of FeMOF-74 because of the greater electron affinity of O_2 than N_2 (see Fig. 21a).[75] Transient breakthroughs for 21/79 O_2/N_2 mixtures (*cf.* Fig. 21b) demonstrate that this MOF would be better suited of pure N_2 than LTA-4A;[21,75] absence of diffusion limitations in FeMOF-74 results in increased productivities of purified N_2.

10 N_2/CH_4 separations

The separation of N_2/CH_4 mixtures is important in the context of natural gas upgrading. For transportation purposes, the pipeline specifications usually demand that the amount of N_2 in natural gas is less than about 3%, because the presence of N_2 reduces the heating value. For purification of natural gas

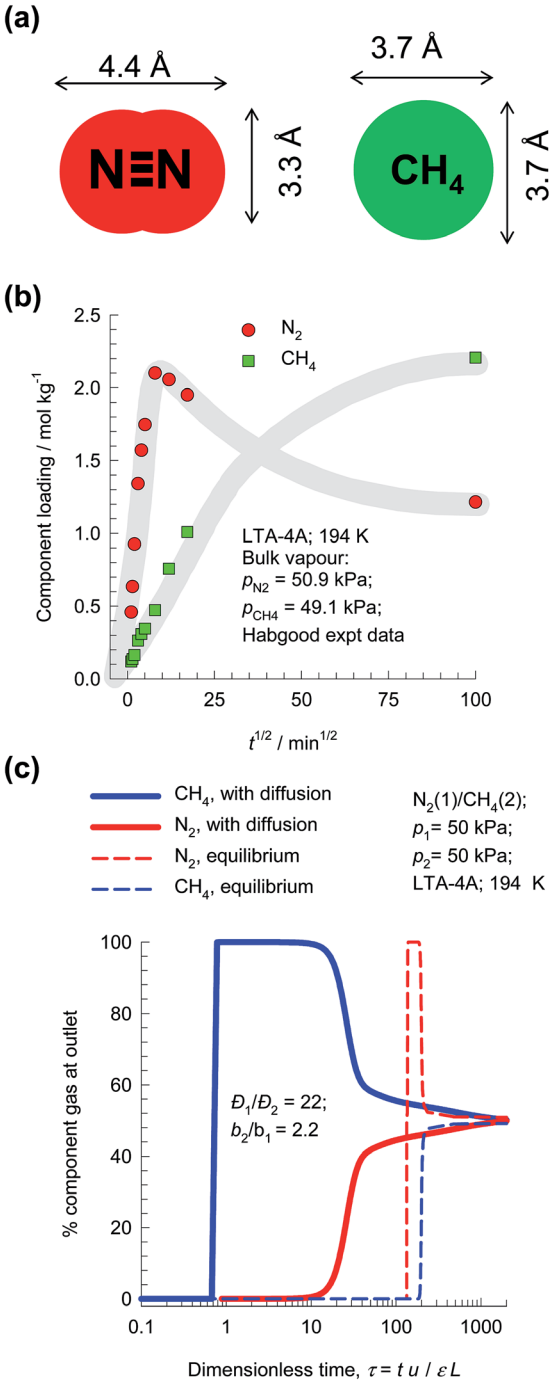

Fig. 22 (a) Molecular dimensions of N_2 and CH_4. (b) Transient uptake of N_2/CH_4 mixture in LTA-4A.[76] (c) PSA process for separation of 50/50 N_2/CH_4 mixture in a fixed bed adsorber packed with LTA-4A operating at a total pressure of 100 kPa and 194 K.

streams, it is desirable to use adsorbents in PSA units that are selective to N_2. For most known adsorbents, the adsorption selectivity favors CH_4; see Li *et al.*[49] One practical solution to this separation problem is to rely on diffusion selectivities by use of microporous LTA-4A zeolite (see Fig. 20b), that consists of cages of about 11 Å size, that are connected by 4 Å window apertures. Nitrogen is a "pencil-like" molecule (4.4 Å × 3.3 Å; see Fig. 22a) that can hop length-wise across the narrow windows; the "spherical" CH_4 (3.7 Å) is much more severely constrained and has a diffusivity that is 22 times lower than that of N_2.

The earliest study demonstrating the possibility of exploiting diffusion selectivities for separating N_2/CH_4 mixtures is due to Habgood,[76] who presents experimental data on transient mixture uptake within LTA-4A (*cf.* Fig. 22b). During the initial stages of the transient uptake, the pores of LTA-4A are predominantly richer in the more mobile N_2, but this is displaced by the more strongly-adsorbed-but-tardier CH_4 molecules at longer times. This results in an overshoot in the N_2 loading within the crystals during the early stages of transience. Note that the maximum loading of N_2 is about a factor 2.5 times that of the final equilibrated uptake. Put another way, supra-equilibrium loadings are attained for N_2 during a short time interval; we infer the occurrence of uphill diffusion.[77] Based on his experimental results, Habgood filed a patent claiming that natural gas could be upgraded by selectively adsorbing the faster diffusing nitrogen in a diffusion-selective PSA process employing LTA-4A zeolite.

In order to demonstrate the possibility of purifying natural gas by exploiting diffusion selectivity principles, Fig. 22c presents the transient breakthroughs of a 50/50 N_2/CH_4 mixture in a fixed bed adsorber packed with LTA-4A operating at a total pressure of 100 kPa and 194 K. We note that the more strongly adsorbed CH_4 is rejected in nearly pure form during the earlier stages of the transient breakthrough. If we were to ignore intra-crystalline diffusion limitations (these simulations are indicated by dashed lines), CH_4 is selectively adsorbed and it is not possible to meet the objectives of purifying natural gas.

Nitrogen-selective separation of N_2/CH_4 mixtures is also be achieved by choosing the pore size to be small enough to exclude CH_4; this is the operative separation principle with BaETS-4.[78]

11 Separation of hexane isomers

The separation of hexane isomers, *n*-hexane (*n*C6), 2-methylpentane (2MP), 3-methylpentane (3MP), 2,2-dimethylbutane (22DMB), and 2,3-dimethylbutane (23DMB) is required for production of high-octane gasoline. The values of the Research Octane Number (RON) increases with the degree of branching; the RON values are: *n*C6 = 30, 2MP = 74.5, 3MP = 75.5, 22DMB = 94, 23DMB = 105. Therefore, di-branched isomers are preferred products for incorporation into the high-octane gasoline pool.[21,79,80] Currently, the separation of hexane isomers is performed using LTA-5A zeolite that operates on the principle of molecular sieving; see Fig. 23a. Linear *n*C6 can hop from one cage to the adjacent cage through the 4 Å windows of LTA-5A, but branched alkanes are largely excluded. An

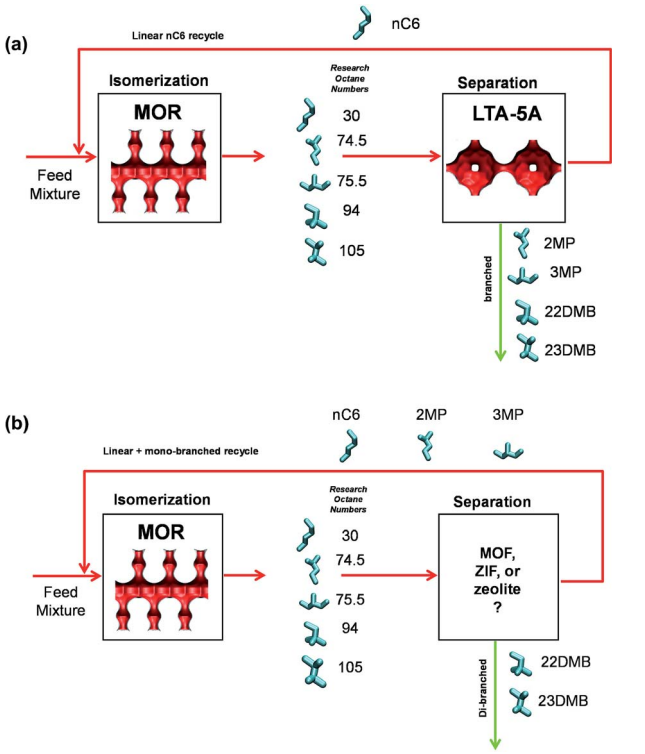

Fig. 23 (a) Currently employed processing scheme for *n*C6 isomerization and subsequent separation step using LTA-4A. (b) Improved processing scheme for the *n*C6 isomerization process.

improved separation scheme, pictured in Fig. 23b, would require an adsorbent that would separate the di-branched isomers 22DMB and 23DMB from the *n*C6, 2MP, and 3MP; this would allow the low-RON components to be recycled back to the isomerization reactor. The separation of 22DMB and 23DMB from the remaining isomers is a difficult task because it requires distinguishing molecules on the *degree* of branching; such a separation is not feasible with the currently used LTA-5A. Typically, in such a processing scheme the aim would be to produce a product stream from the separation step with RON value of 92. This requirement of 92+ RON implies that the product stream will contain predominantly the di-branched isomers 22DMB and 23DMB, while allowing a small proportion of 2MP and 3MP to be incorporated into the product stream. Sharp separations between mono- and di-branched isomers is not a strict requirement.

Herm *et al.*[7] report the synthesis of $Fe_2(BDP)_3$ [BDP^{2-} = benzenedipyrazolate] that has 1D channels which are triangular in shape and a pore size of 4.9 Å (see Fig. 24a). Molecular simulations provide insights into the workings of $Fe_2(BDP)_3$. The linear *n*C6 can align optimally along the V-shaped gutters, and exert the best van der Waals interaction with the framework. The interactions of the mono- and di-branched isomers are less effective, resulting in considerably lower adsorption strengths.

The hierarchy of breakthroughs reported in the transient experiments of Herm[7] is 22DMB, 23DMB, 3MP, 2MP, and *n*C6 (*cf.* Fig. 25a); this hierarchy is dictated by a combination of adsorption strengths (*n*C6 ≫ 2MP ≈ 3MP ≫ 22DMB ≈

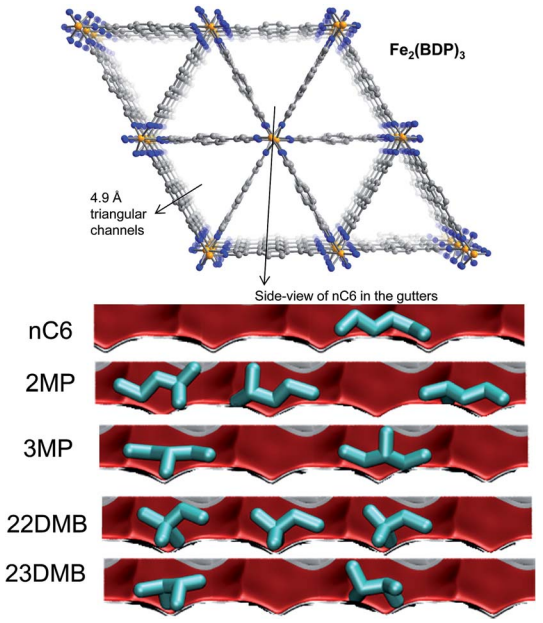

Fig. 24 The triangular channel topology of $Fe_2(BDP)_3$.[7] Also shown are computational snapshots (side-on view) of the conformations of *n*C6, 2MP, 3MP, 22DMB, and 23DMB within the triangular channels.

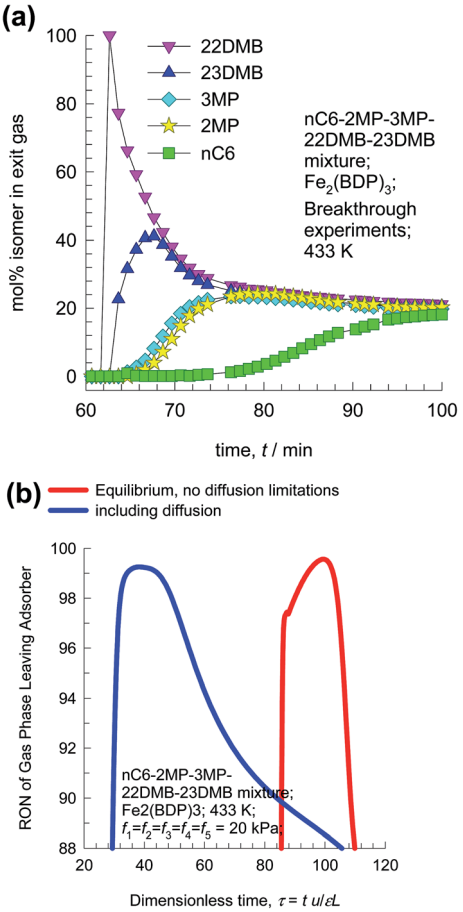

Fig. 25 (a) Experimental data on transient breakthrough of hexane isomers in a fixed bed packed with $Fe_2(BDP)_3$.[7] (b) Influence of diffusional limitations on the RON of product gas exiting fixed bed adsorber packed with $Fe_2(BDP)_3$.

23DMB) and diffusivities (*n*C6 > 2MP ≈ 3MP > 22DMB ≈ 23DMB). The di-branched isomers 22DMB and 23DMB can be recovered in the early stages of the transient breakthrough in fixed bed adsorbers. The experimentally determined breakthroughs in fixed bed adsorbers displays distended characteristics that is indicative of strong intra-crystalline diffusional limitations within the 4.9 Å channels. Taking proper account of intra-crystalline diffusion limitations, the experimental breakthroughs can be properly reproduced by transient breakthrough simulations.[7,21]

From the compositions exiting the adsorber we can determine the RON value of mixture as a function of time. Fig. 25b presents the RON values for $Fe_2(BDP)_3$, calculated using two different scenarios: (1) ignoring intra-crystalline diffusion and assuming thermodynamic equilibrium between a crystal and its surrounding gas at any time t, and position z in the adsorber, and (2) including intra-crystalline diffusion influences. Intra-crystalline diffusion influences leads to earlier breakthroughs and distended RON *vs.* τ characteristics. From a material balance we can determine the mol of product having the desired target value of 92+ RON value. In the scenario of equilibrium adsorption, the 92+ RON productivity is 0.77 mol L^{-1}. Inclusion of diffusion limitations results in a lowering of the productivity to 0.54 mol L^{-1}.

Using MFI zeolite, the separation of hexane isomers is achieved by exploiting subtle configurational differences.[21,79,81] The linear *n*C6 can locate comfortably along the channels (see Fig. 26a). The mono-branched and di-branched isomers locate preferentially at the channel intersections that offer more "legroom" for these bulkier, more-compact, branched isomers. But the number of intersections are limited to 4 per unit cell; this limits the saturation capacities of branched isomers. Under pore saturation conditions typical of industrial operations, molecular packing effects within the MFI channels ensure the sorption hierarchy *n*C6 ≫ 2MP ≈ 3MP ≫ 22DMB ≈ 23DMB, with virtual exclusion of the branched isomers at equilibrium. The presence of branched isomers at the channel intersections is tantatmount to "intersection blocking"; this influences molecular traffic and diffusion.

Intra-crystalline diffusional influences in MFI zeolite have a unique character, as underscored in the recent experimental work of Titze *et al.*[82] With increasing pore occupancy, θ_t, the branched isomers are increasingly excluded. As a consequence, the degree of intersection blocking is reduced and the diffusivity of the linear *n*C6 increases with increasing value of θ_t. The unique synergy between adsorption and diffusion has a beneficial influence on separations. With proper quantification of the synergistic effect of adsorption and diffusion, the 92+ RON productivity achieved with MFI zeolite is 0.64 mol L^{-1}, about a factor 3 higher than that achieved with the scenario in which diffusional effects are considered to be negligible. Diffusional influences enhance the hexanes separation performance of MFI zeolite.

Fig. 26b presents a comparison of 92+ RON productivities of $Fe_2(BDP)_3$, MFI, and ZIF-77 for separation of hexane isomers.

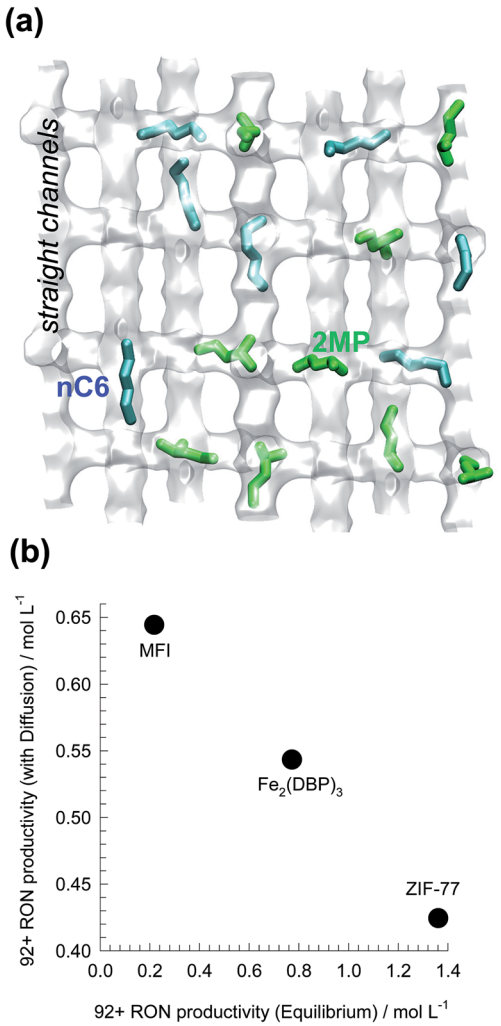

Fig. 26 (a) Snapshots showing the location of *n*C6, and 2MP within the channel network of MFI zeolite. (b) Comparison of 92+ RON productivities of ZIF-77, $Fe_2(BDP)_3$, and MFI for separation of hexane isomers. The productivity values plotted on the *x*-axis are obtained from breakthrough simulations with assumption of thermodynamic equilibrium. The productivity values on the *y*-axis are obtained from breakthrough simulations taking intra-crystalline diffusion into account. Further details are provided in ESI.†

The productivity values on the *y*-axis are obtained from breakthrough simulations taking intra-crystalline diffusion into account. The productivity values plotted on the *x*-axis are obtained from breakthrough simulations with assumption of thermodynamic equilibrium. We note that thermodynamic equilibrium prevails, then the best choice of adsorbent is ZIF-77; indeed, this MOF emerged as the best adsorbent for hexanes isomer separation in the computational screening exercise undertaken by Dubbeldam *et al.*,[80] that did not take diffusional effects into consideration. ZIF-77 has a characteristic pore dimension of 4.5 Å, and intra-crystalline diffusion limitations have a drastic negative influence on the 92+ RON productivity, which is below that of $Fe_2(BDP)_3$. Taking proper account of the synergy between adsorption and diffusion, MFI zeolite emerges as the best adsorbent for separation of hexane isomers.

Pulse chromatographic experiments have been used to demonstrate the potential of ZIF-8 for separations at of alkane isomers;[83] the separation is primarily based on differences in intra-crystalline diffusivities.[21]

12 Separation of xylene isomers

Para-xylene is a valuable petrochemical feedstock; the largest use of *p*-xylene is in its oxidation to make terephthalic acid, that is used in turn to make polymers such as polyethylene terephthalate (PET) and polybutylene terephthalate (PBT). PET is one of the largest volume polymers in the world, and is used to produce fibers, resins, films, and blown beverage bottles.

In a commonly used separation scheme (*cf.* Fig. 27a), the xylenes rich stream from the bottom of the reformer splitter is routed to a xylenes splitter. Here, the heavier aromatics (C9+) are removed from the bottom of the column. The overhead stream from the xylenes splitter, typically containing 19% ethylbenzene, 44% *m*-xylene, 20% *o*-xylene, and 17% *p*-xylene, needs to be separated for recovery of *p*-xylene. In current technology this mixture is separated in a Simulated Moving Bed (SMB) adsorption separation unit. The adsorbent

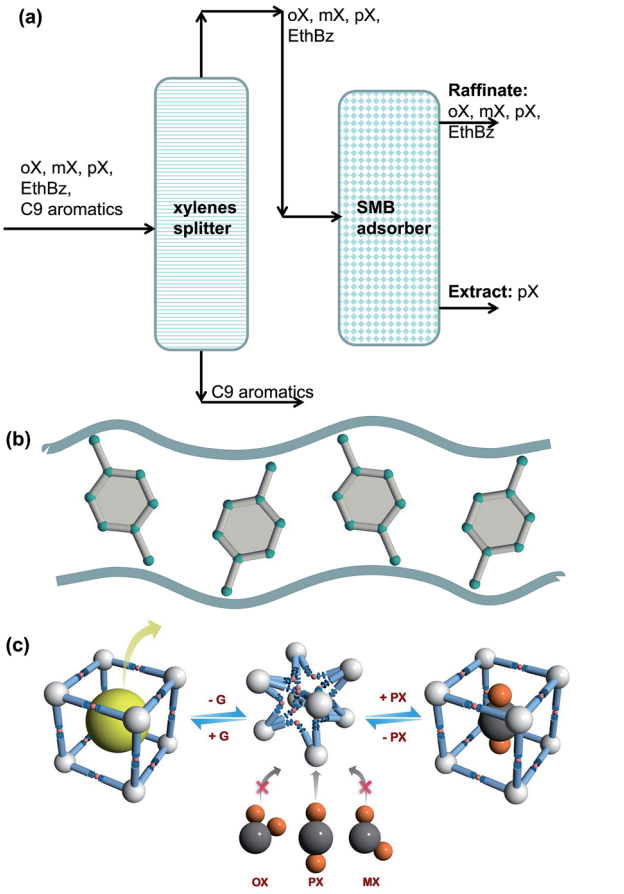

Fig. 27 (a) Schematic showing the separations of the oX/mX/pX/EthBz mixtures in a Simulated Moving Bed (SMB) unit. (b) Stacking of *p*-xylene within 10 Å channels of MAF-X8.[84] (c) Schematic representation of the framework flexibility of DynaMOF-100 with selective accommodation of *p*-xylene from xylenes mixture.[4]

used is BaX zeolite, that selectively adsorbs *p*-xylene. Since the adsorbent particles are in contact with a mixture in the *liquid* phase, the pores of the adsorbent material are practically saturated with guest molecules.[30] For mixture adsorption, let us define the fractional occupancy within the pores, θ_t

$$\theta_t = \sum_{i=1}^{n} \frac{q_i}{q_{i,sat}} \quad (2)$$

where q_i is the molar loading of species i in the mixture, and $q_{i,sat}$ is its saturation capacity. In the SMB unit with BaX zeolite, pore saturation prevails, *i.e.* $\theta_t \rightarrow 1$; the hierarchy of adsorption strengths is dictated by molecular packing, or entropy, effects.[30] Binding energies of guest molecules with the framework walls or non-framework cations do not solely determine the separation performance.

Let us compare the separation performance of BaX with MOFs that have been shown recently to be applicable to this task. Torres-Knoop *et al.*[84] have adopted a conceptual approach, using CBMC simulations for selecting MOFs that selectively adsorb *p*-xylene. Within the one-dimensional 10 Å channels of MAF-X8, we have commensurate stacking of *p*-xylene; see Fig. 27b.[84] Commensurate stacking within 1D channels of MAF-X8, results in strong selectivity in the favor of the *p*-xylene as $\theta_t \rightarrow 1$. More recently, Mukherjee *et al.*[4] report the synthesis of a Zn(II)-based dynamic coordination framework, $[Zn_4O(L)_3]$, also dubbed DynaMOF-100.[5] The framework gets transformed in such a manner as to allow optimal packing of *p*-xylene within the cavities; see Fig. 27c.

For separation of 4-component equimolar *o*-xylene(1)/*m*-xylene(2)/*p*-xylene(3)/ethylbenzene(4) mixtures we adopt the following definition of selectivity that was used in the recent paper of Torres-Knoop *et al.*[84]

$$S_{ads} = \frac{(q_3)/(q_1+q_2+q_4)}{(p_3)/(p_1+p_2+p_4)} = 3\frac{(q_3)}{(q_1+q_2+q_4)} \quad (3)$$

For a fair comparison of adsorbents, we compare the values of the selectivity as function of the fractional occupancy within the pores, θ_t. Fig. 28a shows that the S_{ads} value for DynaMOF-100 (at 298 K) is about one to two orders of magnitude higher than that of MAF-X8 (at 433 K),[84] Mg-CUK-1 (at 323 K),[85] and BaX zeolite (at 393 K, and 453 K).[86,87]

Besides S_{ads}, the separation performance is also dictated by the uptake capacity for *p*-xylene. Fig. 28b compares the *p*-xylene uptake capacity of MAF-X8, Mg-CUK-1, and BaX with that of DynaMOF-100. Fig. 28c presents a plot of selectivity *vs.* uptake capacity at $\theta_t \approx 1$. The combination of high selectivities and high uptake capacities indicates that DynaMOF-100 is the best choice of adsorbent; further experimentation is required to establish this expectation.

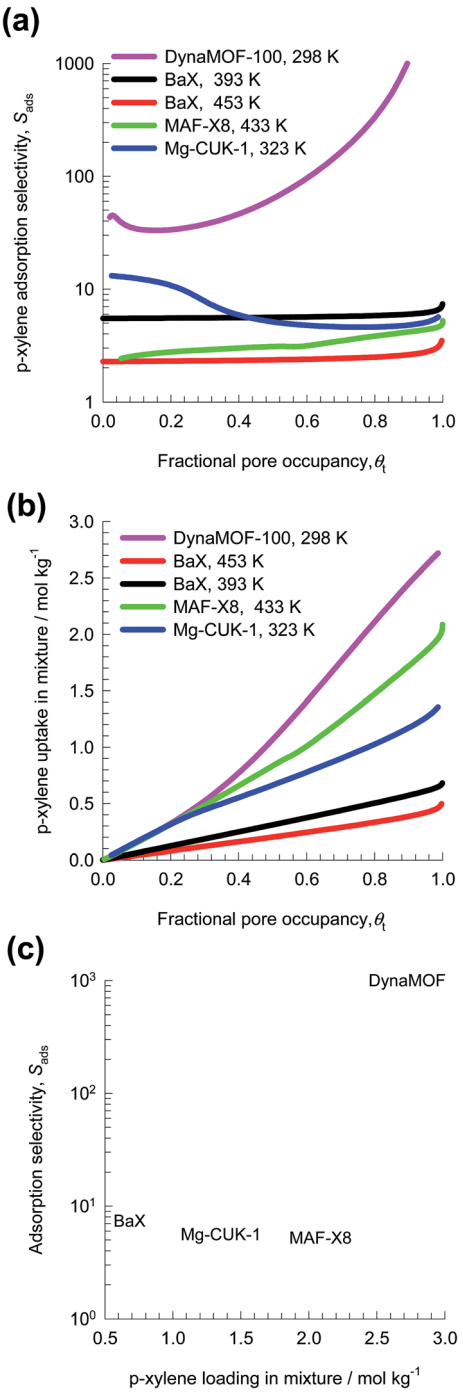

Fig. 28 (a) IAST calculations for *p*-xylene adsorption selectivity for 4-component *o*-xylene/*m*-xylene/*p*-xylene/ethylbenzene mixture in MAF-X8 (at 433 K), BaX zeolite (at 393 K, and 453 K), Mg-CUK-1 (at 323 K), and DynaMOF-100 (at 298 K). The *x*-axis is fractional occupancy, θ_t, within the pores of the MOFs. (b) IAST calculations for *p*-xylene uptake capacity in mixture. (c) Plot of selectivity *vs.* uptake capacity at $\theta_t \approx 1$.

13 Styrene/ethylbenzene separations

Alkylation of benzene with ethene produces ethyl benzene (*cf.* Fig. 29a), which is dehydrogenated to styrene, a monomer used in the manufacture of many commercial polymers and co-polymers. The conversion of ethylbenzene to styrene is only partial, and the reactor product contains a large fraction, in the range of 20–40%, of unreacted ethylbenzene. Due to the small, 9 K, difference in their boiling points, the distillation separation of styrene and ethylbenzene has to be carried out in tall vacuum towers that have high energy demands; adsorptive separations

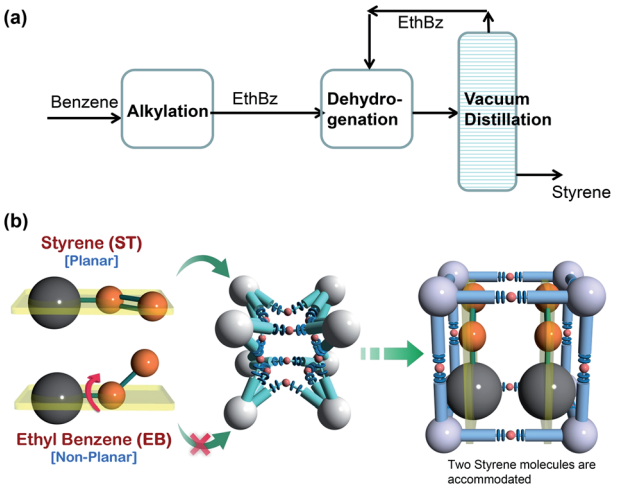

Fig. 29 (a) Current processing scheme for styrene production by vacuum fractionation of styrene/ethylbenzene mixtures. (b) Schematic representation of the framework flexibility of DynaMOF-100 with selective accommodation of styrene from mixtures with ethylbenzene.[5]

using microporous metal–organic frameworks offer energy-efficient alternatives.

In the recent screening study of Torres-Knoop *et al.*,[88] MIL-47(V)[89] and MIL-53(Al)[89] emerged as the best adsorbents for separation of styrene/ethylbenzene mixtures. Let us now compare the performance of MIL-47(V) and MIL-53(Al) with DynaMOF-100 that undergoes guest-induced structural changes to selectively encapsulate styrene (*cf.* Fig. 29b).

Fig. 30a presents the IAST calculations in which the *x*-axis is fractional occupancy, θ_t, within the pores of the MOFs. We note that the value of S_{ads} for DynaMOF-100 is about one to two orders of magnitude higher than that of MIL-47(V) and MIL-53(Al). Fig. 30b compares IAST calculations for styrene uptake capacity in the three MOFs; the uptake capacity of DynaMOF-100 is higher than that of the other two MOFs. Fig. 30c presents a plot of selectivity *vs.* uptake capacity at pore saturation, $\theta_t \approx 1$. Due to the significantly higher adsorption selectivity, and higher styrene uptake capacity, we should expect separations with DynaMOF-100 to be significantly superior to those realized with either MIL-47(V) or MIL-53(Al); this anticipated superiority of DynaMOF-100 needs to be established in experiments.

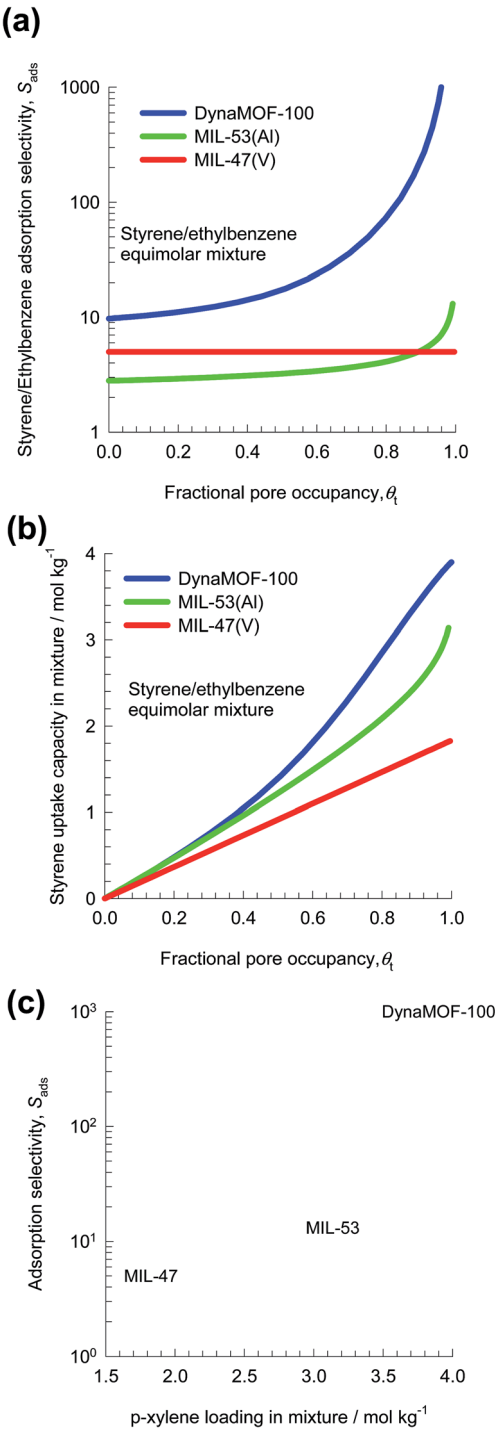

Fig. 30 (c and d) IAST calculations for (a) adsorption selectivity, and (b) uptake capacity of equimolar styrene/ethylbenzene mixtures in MIL-47(V), MIL-53(Al), and DynaMOF-100. The *x*-axis is fractional occupancy, θ_t, within the pores of the MOFs. (c) Plot of selectivity *vs.* uptake capacity at $\theta_t \approx 1$.

14 Stability and other issues that influence the selection of MOFs

The selection methodologies considered in the foregoing sections were based on a number of important simplifying assumptions: (a) trace impurities, such as water vapor, that may be present in the mixtures have been ignored, (b) no account has been taken of the influence of the presence of impurities on the separation performance, and (c) the analysis of every separation is based on isotherm data that have been determined on defect-free as-synthesized crystals. In practice, one or more of the afore-mentioned assumptions may not hold.

Often, the presence of water vapor in industrial flue gas or natural gas streams cannot be ignored when examining

adsorbents for CO_2 capture. In their comprehensive review article, Burtch *et al.*[27] demonstrate that stability of an adsorbent in humid environments is a critical property that needs to be included as part of the MOF selection methodology. Of the 20 000 MOF structures reported to data, very few of them retain their structural integrity after exposure to moisture of chemical treatment.[28,90–92] Kizzie *et al.*[90] have shown that MgMOF-74 is particularly sensitive to the presence of water impurities in the feed mixture, whereas CoMOF-74 and NiMOF-74 are less sensitive in this regard. Liu *et al.*[92] found that NiMOF-74 maintains its CO_2 uptake capacity after steam conditioning and long-term storage, whereas MgMOF-74 does not.

MIL-53(Cr) has a unit cell volume of 1486 Å^3 in the as-synthesized "large pore" form (-lp). At a water loading of 2 molecules per unit cell, the unit cell volume shrinks to 1013 Å^3, the "narrow pore" (-np) form.[93,94] The -np structure is virtually inaccessible to guest molecules. On heating and removal of adsorbed water, the -lp form is regained.

For use in fixed bed adsorbers, the MOFs are most commonly used in the form of pellets or extrudates. As illustration, in the investigation of H_2 separation from steam-methane reformer off-gas as reported by Agueda *et al.*,[57] UTSA-16 crystals were first synthesized according to the method reported in the literature.[58] The crystals were then agglomerated in the form of extrudates using polyvinylalcohol as binder. The CO_2 uptakes measured for the extrudates are found to be about 15% lower than the corresponding data for pristine UTSA-16 crystals. This lowering can be attributed to the binder content in the extrudate, and blocking of the entry into the embedded MOF crystals introduced by the binder.[95]

In the study of Chen *et al.*,[24] CO_2/CH_4 and C_3H_6/C_3H_8 separations with NiMOF-74 in pelletized form are reported. The pellets are formed by compaction of crushed MOF crystals. A careful comparison of the reported unary isotherm data for NiMOF-74 pellets with those obtained for pristine NiMOF-74 crystals,[41,65] show lower uptake values for pellets. This lowering is most likely caused by reduction in the available pore volume, and surface area as a result of the structural transformations accompanying the compaction process.

The implication is that for process development studies with the selected MOFs, the isotherm data need to be re-measured using pellets or extrudates as appropriate.

Fixed bed adsorbers are normally operated in a cyclical manner, with adsorption and desorption cycles. The ability of the selected MOF to retain its separation capability during a large number of adsorption/desorption cycles needs to be ascertained. For C_3H_6/C_3H_8 separations, with FeMOF-74, Bloch *et al.*[59] find that the separation performance is retained after about 40 adsorption/desorption cycles. However, for process development, about a million cycles carried out over a period of a few weeks, need to be tested before possible usage in industrial units.

15 Conclusions

The following major conclusions can be drawn on the basis of the several case studies considered in the foregoing sections.

(1) Separations in PSA units are governed by a combination of adsorption selectivity, uptake capacity, and intra-crystalline diffusion limitations. Selecting MOFs on the basis of adsorption selectivity alone may lead to sub-optimal choice of adsorbent materials. Often, high uptake capacities can over-ride the influence of low selectivities. Conversely, low uptake capacities diminish the separation performance of MOFs with high selectivities.

(2) Transient breakthrough experiments, backed by transient breakthrough simulations, afford a proper evaluation of the separation performance of fixed bed adsorbers.

(3) Strong intra-crystalline diffusional influences lead to distended breakthroughs, resulting in reduced capture capacities and productivities.

(4) Hydrogen production from steam reforming of natural gas involves separations of $H_2/CO_2/CO/CH_4/N_2$ mixtures. The N_2/H_2, CO/H_2, CH_4/H_2 adsorption selectivities are far more relevant than the CO_2/H_2 selectivity. Transient breakthroughs are the only consistent procedure of judging separation performances.

(5) For $CO_2/N_2/SO_2$ separations, SO_2 is often more strongly adsorbed than CO_2 in most MOFs. The purity of N_2 will be dictated by CO_2/N_2 separations; there is no point is searching for MOFs with increased SO_2/N_2 selectivities. For $CO_2/CH_4/H_2S$ separations, H_2S is often more strongly adsorbed than CO_2 on the open metal sites of MOFs. The purity of CH_4 will be dictated by CO_2/CH_4 separations; the H_2S/CH_4 selectivities do not influence the purities of CH_4.

(6) For N_2/CH_4 mixture separations with LTA-4A zeolite, the higher diffusivity of N_2 can be used to reverse the selectivity in its favor; this strategy is useful for meeting the pipeline specifications of natural gas.

(7) A unique scenario holds for hexane isomer separations using MFI zeolite. In this case, adsorption and diffusion proceeds synergistically and enhances separations.

(8) Industrial separations of mixtures of aromatics, are invariably carried out under pore saturation conditions. In these cases, the separations need to be compared at fractional occupancies, $\theta_t \approx 1$.

Notation

c_i	Molar concentration of species i in gas mixture, mol m^{-3}
c_{i0}	Molar concentration of species i in gas mixture at inlet to adsorber, mol m^{-3}
$Đ_i$	Maxwell–Stefan diffusivity, m^2 s^{-1}
L	Length of packed bed adsorber, m
n	Number of components in the mixture, dimensionless
p_i	Partial pressure of species i in mixture, Pa
p_t	Total system pressure, Pa
q_i	Component molar loading of species i, mol kg^{-1}
q_t	Total molar loading for mixture adsorption, mol kg^{-1}
$q_{i,sat}$	Molar loading of species i at saturation, mol kg^{-1}
Q_{st}	Isosteric heat of adsorption, J mol^{-1}

r_c	Radius of crystallite, m
S_{ads}	Adsorption selectivity, dimensionless
t	Time, s
T	Absolute temperature, K
u	Superficial gas velocity in packed bed, m s^{-1}

Greek letters

α	Polarizability, cm^3
ε	Voidage of packed bed, dimensionless
θ_t	Fractional occupancy for mixture adsorption, dimensionless
τ	Time, dimensionless

Subscripts

i	referring to component i
t	referring to total mixture

References

1 D. M. Ruthven, S. Farooq and K. S. Knaebel, *Pressure swing adsorption*, VCH Publishers, New York, 1994.
2 R. Krishna and J. M. van Baten, *Microporous Mesoporous Mater.*, 2011, **137**, 83–91.
3 Y. Lee, J. A. Hriljac, T. Vogt, J. B. Parise, M. J. Edmondson, P. A. Anderson, D. R. Corbin and T. Nagai, *J. Am. Chem. Soc.*, 2001, **123**, 8418–8419.
4 S. Mukherjee, B. Joarder, B. Manna, A. V. Desai, A. K. Chaudhari and S. K. Ghosh, *Sci. Rep.*, 2014, **4**, 5761, DOI: 10.1038/srep05761.
5 S. Mukherjee, B. Joarder, A. V. Desai, B. Manna, R. Krishna and S. K. Ghosh, *Inorg. Chem.*, 2015, **54**, 4403–4408.
6 V. Guillerm, F. Ragon, M. Dan-Hardi, T. Devic, M. Vishnuvarthan, B. Campo, A. Vimont, G. Clet, Q. Yang, G. Maurin, G. Férey, A. Vittadini, S. Gross and C. Serre, *Angew. Chem., Int. Ed.*, 2012, **51**, 9267–9271.
7 Z. R. Herm, B. M. Wiers, J. M. Van Baten, M. R. Hudson, P. Zajdel, C. M. Brown, N. Maschiocchi, R. Krishna and J. R. Long, *Science*, 2013, **340**, 960–964.
8 A. Torres-Knoop, S. R. G. Balestra, R. Krishna, S. Calero and D. Dubbeldam, *ChemPhysChem*, 2015, **16**, 532–535.
9 R. Matsuda, R. Kitaura, S. Kitagawa, Y. Kubota, R. V. Belosludov, T. C. Kobayashi, H. Sakamoto, T. Chiba, M. Takata, Y. Kawazoe and Y. Mita, *Nature*, 2005, **436**, 238–241.
10 M. Fischer, F. Hoffmann and M. Fröba, *ChemPhysChem*, 2010, **11**, 2220–2229.
11 P. Li, Y. He, Y. Zhao, L. Weng, H. Wang, R. Krishna, H. Wu, W. Zhou, M. O'Keeffe, Y. Han and B. Chen, *Angew. Chem., Int. Ed.*, 2015, **54**, 574–577.
12 X. Duan, Q. Zhang, J. Cai, Y. Yang, Y. Cui, Y. He, C. Wu, R. Krishna, B. Chen and G. Qian, *J. Mater. Chem. A*, 2014, **2**, 2628–2633.
13 J. Duan, W. Jin and R. Krishna, *Inorg. Chem.*, 2015, **54**, 4279–4284.
14 A. L. Myers and J. M. Prausnitz, *AIChE J.*, 1965, **11**, 121–130.
15 R. Krishna and J. M. van Baten, *Chem. Phys. Lett.*, 2007, **446**, 344–349.
16 R. Krishna and J. M. van Baten, *Sep. Purif. Technol.*, 2008, **61**, 414–423.
17 R. Krishna and J. M. van Baten, *Chem. Eng. Sci.*, 2008, **63**, 3120–3140.
18 R. Krishna and J. M. van Baten, *Chem. Eng. J.*, 2008, **140**, 614–620.
19 J. J. Gutierrez-Sevillano, S. Calero and R. Krishna, *J. Phys. Chem. C*, 2015, **119**, 3658–3666.
20 R. Krishna and J. R. Long, *J. Phys. Chem. C*, 2011, **115**, 12941–12950.
21 R. Krishna, *Microporous Mesoporous Mater.*, 2014, **185**, 30–50.
22 H. Wu, K. Yao, Y. Zhu, B. Li, Z. Shi, R. Krishna and J. Li, *J. Phys. Chem. C*, 2012, **116**, 16609–16618.
23 D.-L. Chen, N. Wang, F.-F. Wang, J. Xie, Y. Zhong, W. Zhu, J. K. Johnson and R. Krishna, *J. Phys. Chem. C*, 2014, **118**, 17831–17838.
24 D.-L. Chen, H. Shang, W. Zhu and R. Krishna, *Chem. Eng. Sci.*, 2014, **117**, 407–415.
25 D.-L. Chen, N. Wang, C. Xu, G. Tu, W. Zhu and R. Krishna, *Microporous Mesoporous Mater.*, 2015, **208**, 55–65.
26 H. Yu, X. Wang, C. Xu, D.-L. Chen, W. Zhu and R. Krishna, *Chem. Eng. J.*, 2015, **269**, 135–147.
27 N. C. Burtch, H. Jasuja and K. S. Walton, *Chem. Rev.*, 2014, **114**, 10575–10612.
28 J. B. DeCoste, G. W. Peterson, B. J. Schindler, K. L. Killops, M. A. Browe and J. J. Mahle, *J. Mater. Chem. A*, 2013, **1**, 11922–11932.
29 D. Banerjee, A. J. Cairns, J. Liu, R. Krishna, P. K. Thallapally and D. M. Strachan, *Acc. Chem. Res.*, 2015, **48**, 211–219.
30 R. Krishna, *Phys. Chem. Chem. Phys.*, 2015, **17**, 39–59.
31 Z.-Y. Gu, C.-X. Yang, N. Chang and X.-P. Yan, *Acc. Chem. Res.*, 2012, **45**, 734–745.
32 H. Wang, K. Yao, Z. Zhang, J. Jagiello, Q. Gong, Y. Han and J. Li, *Chem. Sci.*, 2014, **5**, 620–624.
33 R. Krishna, *J. Phys. Chem. C*, 2009, **113**, 19756–19781.
34 R. Krishna and J. M. van Baten, *Mol. Simul.*, 2009, **35**, 1098–1104.
35 X. Chen, A. M. Plonka, D. Banerjee, R. Krishna, H. T. Schaef, D. Ghose, P. K. Thallapally and J. B. Parise, *J. Am. Chem. Soc.*, 2015, DOI: 10.1021/jacs.5b02556.
36 J. Liu, P. K. Thallapally and D. Strachan, *Langmuir*, 2012, **28**, 11584–11589.
37 J. Liu, D. M. Strachan and P. K. Thallapally, *Chem. Commun.*, 2014, **50**, 466–468.
38 Y. Gurdal and S. Keskin, *Ind. Eng. Chem. Res.*, 2012, **51**, 7373–8382.
39 J. A. Mason, K. Sumida, Z. R. Herm, R. Krishna and J. R. Long, *Energy Environ. Sci.*, 2011, **4**, 3030–3040.

40 H. Wu, J. M. Simmons, G. Srinivas, W. Zhou and T. Yildrim, *J. Phys. Chem. Lett.*, 2010, **1**, 1946–1951.
41 P. D. C. Dietzel, V. Besikiotis and R. Blom, *J. Mater. Chem.*, 2009, **19**, 7362–7370.
42 Y. Belmabkhout, G. Pirngruber, E. Jolimaitre and A. Methivier, *Adsorption*, 2007, **13**, 341–349.
43 M. R. Hudson, L. Murray, J. A. Mason, D. W. Fickel, R. F. Lobo, W. L. Queen and C. M. Brown, *J. Am. Chem. Soc.*, 2012, **134**, 1970–1973.
44 S. Li, J. L. Falconer, R. D. Noble and R. Krishna, *J. Phys. Chem. C*, 2007, **111**, 5075–5082.
45 R. Krishna and J. M. van Baten, *J. Membr. Sci.*, 2013, **430**, 113–128.
46 S. Yang, J. Sun, A. J. Ramirez-Cuesta, S. K. Callear, W. I. F. David, D. P. Anderson, R. Newby, A. J. Blake, J. E. Parker, C. C. Tang and M. Schröder, *Nat. Chem.*, 2012, **4**, 887–894.
47 Z. R. Herm, J. A. Swisher, B. Smit, R. Krishna and J. R. Long, *J. Am. Chem. Soc.*, 2011, **133**, 5664–5667.
48 G. T. Rochelle, *Science*, 2009, **325**, 1652–1654.
49 L. Li, J. Yang, J. Li, Y. Chen and J. Li, *Microporous Mesoporous Mater.*, 2014, **198**, 236–246.
50 S. Chavan, F. Bonino, L. Valenzano, B. Civalleri, C. Lamberti, N. Acerbi, J. H. Cavka, M. Leistner and S. Bordiga, *J. Phys. Chem. C*, 2013, **117**, 15615–15622.
51 S. Vaesen, V. Guillerm, Q. Yang, A. D. Wiersum, B. Marszalek, B. Gil, A. Vimont, M. Daturi, T. Devic, P. L. Llewellyn, C. Serre, G. Maurin and G. De Weireld, *Chem. Commun.*, 2013, **49**, 10082–10084.
52 S. Sircar and T. C. Golden, *Sep. Sci. Technol.*, 2000, **35**, 667–687.
53 A. M. Ribeiro, C. A. Grande, F. V. S. Lopes, J. M. Loureiro and A. E. Rodrigues, *Chem. Eng. Sci.*, 2008, **63**, 5258–5273.
54 A. M. Banu, D. Friedrich, S. Brandani and T. Düren, *Ind. Eng. Chem. Res.*, 2013, **52**, 9946–9957.
55 E. H. Majlan, W. R. W. Daud, S. E. Iyuke, A. B. Mohamad, A. H. Kadhum, A. W. Mohammad, M. S. Takriff and N. Bahaman, *Int. J. Hydrogen Energy*, 2009, **34**, 2771–2777.
56 Z. R. Herm, R. Krishna and J. R. Long, *Microporous Mesoporous Mater.*, 2012, **151**, 481–487.
57 V. I. Agueda, J. A. Delgado, M. A. Uguina, P. Brea, A. I. Spjelkavik, R. Blom and C. Grande, *Chem. Eng. Sci.*, 2015, **124**, 159–169.
58 S. C. Xiang, Y. He, Z. Zhang, H. Wu, W. Zhou, R. Krishna and B. Chen, *Nat. Commun.*, 2012, **3**, 954, DOI: 10.1038/ncomms1956.
59 E. D. Bloch, W. L. Queen, R. Krishna, J. M. Zadrozny, C. M. Brown and J. R. Long, *Science*, 2012, **335**, 1606–1610.
60 S. M. Chavan, G. C. Shearer, E. D. Bloch and S. Bordiga, *ChemPhysChem*, 2012, **13**, 445–448.
61 M. C. Das, Q. Guo, Y. He, J. Kim, C. G. Zhao, K. Hong, S. Xiang, Z. Zhang, K. M. Thomas, R. Krishna and B. Chen, *J. Am. Chem. Soc.*, 2012, **134**, 8703–8710.
62 T.-L. Hu, H. Wang, B. Li, R. Krishna, H. Wu, W. Zhou, Y. Zhao, Y. Han, X. Wang, W. Zhu, Z. Yao, S. C. Xiang and B. Chen, *Nat. Commun.*, 2015, **6**, 7328, DOI: 10.1038/ncomms8328.
63 Y.-S. Bae, C. Y. Lee, K. C. Kim, O. K. Farha, P. Nickias, J. T. Hupp, S. T. Nguyen and R. Q. Snurr, *Angew. Chem., Int. Ed.*, 2012, **51**, 1857–1860.
64 Z. Bao, S. Alnemrat, I. Vasiliev, Q. Ren, L. Yu, X. Lu and S. Deng, *Langmuir*, 2011, **27**, 13554–13562.
65 S. J. Geier, J. A. Mason, E. D. Bloch, W. L. Queen, M. R. Hudson, C. M. Brown and J. R. Long, *Chem. Sci.*, 2013, **4**, 2054–2061.
66 Y. Zhang, B. Li, R. Krishna, Z. Wu, D. Ma, Z. Shi, T. Pham, K. Forrest, B. Space and S. Ma, *Chem. Commun.*, 2015, **51**, 2714–2717.
67 B. Li, Y. Zhang, R. Krishna, K. Yao, Y. Han, Z. Wu, D. Ma, Z. Shi, T. Pham, B. Space, J. Liu, P. K. Thallapally, J. Liu, M. Chrzanowski and S. Ma, *J. Am. Chem. Soc.*, 2014, **136**, 8654–8660.
68 S. Yang, A. J. Ramirez-Cuesta, R. Newby, V. Garcia-Sakai, P. Manuel, S. K. Callear, S. I. Campbell, C. C. Tang and M. Schröder, *Nat. Chem.*, 2014, **7**, 121–129.
69 F. A. Da Silva and A. E. Rodrigues, *AIChE J.*, 2001, **47**, 341–357.
70 C. A. Grande, F. Poplow and A. E. Rodrigues, *Sep. Sci. Technol.*, 2010, **45**, 1252–1259.
71 C. Gücüyener, J. van den Bergh, J. Gascon and F. Kapteijn, *J. Am. Chem. Soc.*, 2010, **132**, 17704–17706.
72 J. Kim, L.-C. Lin, R. L. Martin, J. A. Swisher, M. Haranczyk and B. Smit, *Langmuir*, 2012, **28**, 11914–11919.
73 U. Böhme, B. Barth, C. Paula, A. Kuhnt, W. Schwieger, A. Alexander Mundstock, J. Caro and M. Hartmann, *Langmuir*, 2013, **29**, 8592–8600.
74 S. Farooq, D. M. Ruthven and H. A. Boniface, *Chem. Eng. Sci.*, 1989, **44**, 2809–2816.
75 E. D. Bloch, L. Murray, W. L. Queen, S. M. Chavan, S. N. Maximoff, J. P. Bigi, R. Krishna, V. K. Peterson, F. Grandjean, G. J. Long, B. Smit, S. Bordiga, C. M. Brown and J. R. Long, *J. Am. Chem. Soc.*, 2011, **133**, 14814–14822.
76 H. W. Habgood, *Can. J. Chem.*, 1958, **36**, 1384–1397.
77 R. Krishna, *Chem. Soc. Rev.*, 2015, **44**, 2812–2836.
78 B. Majumdar, S. J. Bhadra, R. P. Marathe and S. Farooq, *Ind. Eng. Chem. Res.*, 2011, **50**, 3021–3034.
79 R. Krishna and J. M. van Baten, *Sep. Purif. Technol.*, 2007, **55**, 246–255.
80 D. Dubbeldam, R. Krishna, S. Calero and A. Ö. Yazaydın, *Angew. Chem., Int. Ed.*, 2012, **51**, 11867–11871.
81 R. Krishna, *Chem. Eng. Res. Des.*, 2001, **79**, 182–194.
82 T. Titze, C. Chmelik, J. Kärger, J. M. van Baten and R. Krishna, *J. Phys. Chem. C*, 2014, **118**, 2660–2665.
83 N. Chang, Z.-Y. Gu and X.-P. Yan, *J. Am. Chem. Soc.*, 2010, **132**, 13645–13647.
84 A. Torres-Knoop, R. Krishna and D. Dubbeldam, *Angew. Chem., Int. Ed.*, 2014, **53**, 7774–7778.
85 B. Saccoccia, A. M. Bohnsack, N. W. Waggoner, K. H. Cho, J. S. Lee, D.-Y. Hong, V. M. Lynch, J.-S. Chang and S. M. Humphrey, *Angew. Chem., Int. Ed.*, 2015, **54**, 5394–5398.
86 M. Minceva and A. E. Rodrigues, *AIChE J.*, 2007, **53**, 138–149.
87 M. Minceva and A. E. Rodrigues, *Chem. Eng. Res. Des.*, 2004, **82**, 667–681.

88 A. Torres-Knoop, J. Heinen, R. Krishna and D. Dubbeldam, *Langmuir*, 2015, **31**, 3771–3778.
89 M. Maes, F. Vermoortele, L. Alaerts, S. Couck, C. E. A. Kirschhock, J. F. M. Denayer and D. E. De Vos, *J. Am. Chem. Soc.*, 2010, **132**, 15277–15285.
90 A. C. Kizzie, A. G. Wong-Foy and A. J. Matzger, *Langmuir*, 2011, **27**, 6368–6373.
91 J. Liu, J. Tian, P. K. Thallapally and B. P. McGrail, *J. Phys. Chem. C*, 2012, **116**, 9575–9581.
92 J. Liu, A. I. Benin, A. M. B. Furtado, P. Jakubczak, R. R. Willis and M. D. LeVan, *Langmuir*, 2011, **27**, 11451–11456.
93 C. Serre, F. Millange, C. Thouvenot, M. Nouguès, G. Marsolier, D. Louër and G. Férey, *J. Am. Chem. Soc.*, 2002, **124**, 13519–13526.
94 D. Dubbeldam, R. Krishna and R. Q. Snurr, *J. Phys. Chem. C*, 2009, **113**, 19317–19327.
95 V. Finsy, L. Ma, L. Alaerts, D. E. de Vos, G. V. Baron and J. F. M. Denayer, *Microporous Mesoporous Mater.*, 2009, **120**, 221–227.

Electronic Supplementary Information (ESI) to accompany:

Methodologies for Evaluation of Metal-Organic Frameworks in Separation Applications

Rajamani Krishna

Van 't Hoff Institute for Molecular Sciences, University of Amsterdam, Science Park 904,

1098 XH Amsterdam, The Netherlands

CORRESPONDING AUTHOR *Tel +31 20 6270990; Fax: + 31 20 5255604;

email: r.krishna@contact.uva.nl

Table of Contents

1. Simulation methodology for transient breakthrough in fixed bed adsorbers

Fixed bed, packed with crystals of microporous materials, are commonly used for separation of mixtures (see schematic in Figure **2**); such adsorbers are commonly operated in a transient mode, and the compositions of the gas phase, and component loadings within the crystals, vary with position and time. During the initial stages of the transience, the pores are loaded up gradually, and only towards the end of the adsorption cycle are conditions corresponding to pore saturation attained. Put another way, separations in fixed bed adsorbers are influenced by both the Henry regime of adsorption as well as the conditions corresponding to pore saturation. Experimental data on the transient breakthrough of mixtures across fixed beds are commonly used to evaluate and compare the separation performance of zeolites and MOFs.[1-5] For a given separation task, transient breakthroughs provide more a realistic evaluation of the efficacy of a material, as they reflect the combined influence of adsorption selectivity, adsorption capacity, and intra-crystalline diffusion limitations.[5, 6]

We describe below the simulation methodology used to perform transient breakthrough calculations that are presented in this work. This simulation methodology is the same as that used in our previous published work.[5]

Assuming plug flow of an *n*-component gas mixture through a fixed bed maintained under isothermal conditions, the partial pressures in the gas phase at any position and instant of time are obtained by solving the following set of partial differential equations for each of the species *i* in the gas mixture.[7]

$$\frac{1}{RT}\frac{\partial p_i(t,z)}{\partial t} = -\frac{1}{RT}\frac{\partial\left(v(t,z)p_i(t,z)\right)}{\partial z} - \frac{\left(1-\varepsilon\right)}{\varepsilon}\rho\frac{\partial \bar{q}_i(t,z)}{\partial t}; \quad i = 1,2,...n \tag{1}$$

In equation (1), t is the time, z is the distance along the adsorber, ρ is the framework density, ε is the bed voidage, v is the interstitial gas velocity, and $\bar{q}_i(t,z)$ is the *spatially averaged* molar loading within the crystallites of radius r_c, monitored at position z, and at time t.

At any time t, during the transient approach to thermodynamic equilibrium, the spatially averaged molar loading within the crystallite r_c is obtained by integration of the radial loading profile

$$\bar{q}_i(t) = \frac{3}{r_c^3}\int_0^{r_c} q_i(r,t) r^2 dr \tag{2}$$

For transient unary uptake within a crystal at any position and time with the fixed bed, the radial distribution of molar loadings, q_i, within a spherical crystallite, of radius r_c, is obtained from a solution of a set of differential equations describing the uptake

$$\frac{\partial q_i(r,t)}{\partial t} = -\frac{1}{\rho}\frac{1}{r^2}\frac{\partial}{\partial r}\left(r^2 N_i\right) \tag{3}$$

The molar flux N_i of component i is described by the simplified version of the Maxwell-Stefan equations in which both correlation effects and thermodynamic coupling effects are considered to be of negligible importance[5]

$$N_i = -\rho Đ_i \frac{\partial q_i}{\partial r} \tag{4}$$

Summing equation (**2**) over all n species in the mixture allows calculation of the *total average* molar loading of the mixture within the crystallite

$$\bar{q}_t(t,z) = \sum_{i=1}^{n} \bar{q}_i(t,z) \tag{5}$$

The *interstitial* gas velocity is related to the *superficial* gas velocity by

$$v = \frac{u}{\varepsilon} \tag{6}$$

In industrial practice, the most common operation is with to use a step-wise input of mixtures to be separation into an adsorber bed that is initially free of adsorbates, i.e. we have the initial condition

$$t = 0; \quad q_i(0,z) = 0 \tag{7}$$

At time, $t = 0$, the inlet to the adsorber, $z = 0$, is subjected to a step input of the n-component gas mixture and this step input is maintained till the end of the adsorption cycle when steady-state conditions are reached.

$$t \geq 0; \quad p_i(0,t) = p_{i0}; \quad u(0,t) = u \tag{8}$$

where u is the superficial gas velocity at the inlet to the adsorber.

Besides, the breakthrough simulations with a step-input (8), we also carried out simulations for a packed bed adsorber with injection of a short duration pulse of the mixture to be separated. This type of simulation is particularly useful to demonstrate the fractionating capability of adsorbents. For simulation of pulse chromatographic separations, we use the corresponding set of inlet conditions

$$0 \leq t \leq t_0; \quad p_i(0,t) = p_{i0}; \quad u(0,t) = u \tag{9}$$

where the time for duration of the pulse is t_0. The pulse duration is generally very short, and therefore pore saturation conditions are never approached at any position at any time t. Therefore, pulse chromatographic simulations, and the corresponding experiments, do not reflect molecular packing effects. Pulse chromatographic simulations and experiments are representative of separations in the Henry regime at low pore occupancies.[8, 9] Pulse chromatographic experiments have been used to demonstrate the potential of MOFs for separations at of alkane isomers,[10] and xylene isomers[11, 12] at low pore occupancies. In this review article, pulse chromatographic simulations are only used to demonstrate the separation of noble gases using CuBTC.

If the value of $\frac{Đ_i}{r_c^2}$ is large enough to ensure that intra-crystalline gradients are absent and the entire crystallite particle can be considered to be in thermodynamic equilibrium with the surrounding bulk gas phase at that time t, and position z of the adsorber

$$\bar{q}_i(t,z) = q_i(t,z) \tag{10}$$

The molar loadings at the *outer surface* of the crystallites, i.e. at $r = r_c$, are calculated on the basis of adsorption equilibrium with the bulk gas phase partial pressures p_i at that position z and time t. The

adsorption equilibrium can be calculated on the basis of the Ideal Adsorbed Solution Theory (IAST) of Myers and Prausnitz.[13] In all the simulation results we present in this article, the IAST calculations use pure component isotherms fitted with the Langmuir, Langmuir-Freundlich, or dual-Langmuir-Freundlich model.

For presenting the breakthrough simulation results, we use the dimensionless time, $\tau = \frac{tu}{L\varepsilon}$, obtained by dividing the actual time, t, by the characteristic time, $\frac{L\varepsilon}{u}$, where L is the length of adsorber, u is the superficial fluid velocity, ε is the bed voidage.[6]

For all the simulations reported in this article we choose the following: adsorber length, L = 0.3 m; cross-sectional area, A = 1 m^2; superficial gas velocity in the bed, u = 0.04 m s^{-1}; voidage of the packed bed, ε = 0.4. Please note that since the superficial gas velocity is specified, the specification of the cross-sectional area of the tube, A, is not relevant in the simulation results presented. The volume of MOF used in the simulations is (1 - ε) A L = 0.18 m^3. If ρ is the framework density, the mass of the adsorbent in the bed is ρ (1 - ε) A L kg. In these breakthrough simulations we use the same volume of adsorbent in the breakthrough apparatus, i.e. (1 - ε) A L = 0.18 m^3.

2. Transient breakthrough experiments for CO_2/CH_4 separations

We analyze a set of experimental breakthroughs for 50/50 CO_2/CH_4 mixtures in bed packed with NiMOF-74 and Kureha carbon measured in the same set-up and reported by Chen et al.[14] and Yu et al.[15] The tube length, L =100 mm and the internal diameter, d = 4.65 mm; see schematic in Figure **2**.

The cross-sectional area of the tube, is

$$A = \frac{\pi}{4} d^2 \tag{11}$$

The volume of the empty tube, V, is

$$V = AL \tag{12}$$

Let m_{ads} represent the mass of adsorbent packed into the tube. The volume occupied by the adsorbent crystalline material, V_{ads}, is

$$V_{ads} = \frac{m_{ads}}{\rho} \tag{13}$$

A precisely determined mass of each adsorbent (Ni-MOF-74 pellet sample = 576.1 mg, and Kureha carbon = 760 mg) was filled into the column and then heated in flowing He with a rate of 20 ml (STP) min^{-1} at 423 K for 8 h prior to the breakthrough measurements. The breakthrough curves were then measured by switching the He flow to a flow containing CO_2 and CH_4 in He (used as a balance) with a CO_2:CH_4:He mole composition of 1:1:2 at a total flow rate of 8 mL (STP) min^{-1}.

As illustration, Figures 3a,b compares the experimental breakthroughs for CO_2(1)/CH_4(2)/He(3) in packed bed with NiMOF-74, and Kureha carbon at 298 K. The partial pressures at the inlet are $p_1 = p_2 =$ 50 kPa; $p_3 = 100$ kPa. For both materials, with the notable exception of NH_2-MIL-101, there is a finite time interval within which 99%+ pure CH_4 can be produced. As illustration in Figure 3b, for NiMOF-74 it is possible to produce CH_4 with 99%+ purity during the time interval between t_1, and t_2.

The gravimetric CO_2 uptake can be calculated from

$$\text{CO}_2 \text{ uptake} = \frac{c_t Q_{He}}{m_{ads}} \int_0^{t_{ss}} \left(\frac{y_{CO2,inlet}}{y_{He,inlet}} - \frac{y_{CO2,exit}}{y_{He,exit}} \right) dt - \frac{\left(c_t y_{CO2,exit}\right)}{m_{ads}} \left(AL - V_{ads}\right) \tag{14}$$

The volumetric CO_2 uptake is obtained by multiplying by the framework density (= grain density) of the adsorbent. Figure 3c shows the dependence of the volumetric uptake on the dimensionless breakthrough time.

A material balance for the time interval $t = t_1 - t_2$ allows us to determine the productivity of CH_4 with the specified 99%+ purity

$$\text{CH}_4 \text{ productivity} = \frac{c_t Q_{He}}{m_{ads}} \int_{t_1}^{t_2} \left(\frac{y_{CH4,exit}}{y_{He,exit}} \right) dt \tag{15}$$

3. C_2H_2/CO_2 separations

MOF	Surface area $m^2\ g^{-1}$	Pore volume $cm^3\ g^{-1}$	Framework density $kg\ m^{-3}$	Data sources for unary isotherm fits	Comment
HOF-3	165	0.0971	453	[16]	
ZJU-60a	1627	0.868	631	[17]	
CuBTC	2097	0.848	879	[18, 19]	
PCP-33	1248	0.502	1261	[20]	
Cu_2TPTC	2405		760	[21]	

HOF-3 is a rod-packing 3D microporous hydrogen-bonded organic framework exhibiting the **srs** topology.[16]

ZJU-60a = Cu_2(MFDI) is a three-dimensional microporous metal–organic framework with a rare **sty-a** type topology.[17]

CuBTC (=$Cu_3(BTC)_2$ with BTC = 1,3,5-benzenetricarboxylate, also known as HKUST-1) structure consists of two types of "cages" and two types of "windows" separating these cages. Large cages are inter-connected by 9 Å windows of square cross-section. The large cages are also connected to tetrahedral-shaped pockets of ca. 6 Å size through triangular-shaped windows of ca. 4.6 Å size.

PCP-33 = $[(Cu_4Cl)(BTBA)_8\cdot(CH_3)_2NH_2)]$ based on a symmetric ligand (3,5-bis(2H-tetrazol-5-yl)-benzoic acid, H_3BTBA).[20]

Cu_2TPTC-Me (TPTC-Me =2′,5′-dimethyl-[1,1′:4′,1″-terphenyl]-3,3″,5,5″-tetracarboxylate) is a NbO type isostructural MOF synthesized by Xia et al. [21]. The separation performance of this MOF is almost identical to that of PCP-33. The comparison of the C_2H_2/CO_2 mixture separations using Cu_2TPTC-Me with the four other MOFs are provided in Figure 4.

Figures 4a, 4b show IAST calculations of (a) adsorption selectivity, S_{ads}, and (b) uptake capacity of C_2H_2, for separation of 50/50 C_2H_2/CO_2 mixture.

Figure 4c compares the % C_2H_2 in the exit gas plotted as a function of the dimensionless breakthrough time. We see that the breakthrough time for Cu_2TPTC-Me is identical to that of PCP-33.

4. Xe/Kr separations

MOF	Surface area $m^2\ g^{-1}$	Pore volume $cm^3\ g^{-1}$	Framework density $kg\ m^{-3}$	Data sources for unary isotherm fits	Comment
Ag@NiMOF-74	750		1240	[22]	Intra-crystalline diffusion effects are not significant
NiMOF-74	1532	0.582	1220	[22, 23]	
CuBTC	2097	0.848	879	[23, 24]	
SBMOF-2			1192	[25]	
CoFormate	300		1819	[26]	Intra-crystalline diffusion effects are not significant

NiMOF-74 = (Ni_2 (dobdc) = Ni\(dobdc) with dobdc = (dobdc4– = 1,4-dioxido-2,5-benzenedicarboxylate)). This MOF consists of one-dimensional hexagonal-shaped channels with free internal diameter of ca. 11 Å.

Ag@NiMOF-74 = silver loaded NiMOF-74.[22]

CuBTC (=$Cu_3(BTC)_2$ with BTC = 1,3,5-benzenetricarboxylate, also known as HKUST-1) structure consists of two types of "cages" and two types of "windows" separating these cages. Large cages are inter-connected by 9 Å windows of square cross-section. The large cages are also connected to tetrahedral-shaped pockets of ca. 6 Å size through triangular-shaped windows of ca. 4.6 Å size.

SBMOF-2 (Stony Brook MOF-2) is a robust 3-D porous crystalline structure containing calcium and 1,2,4,5-tetrakis(4-carboxyphenyl)benzene. [26]

CoFormate = $Co_3(HCOO)_6$. The framework contains one-dimensional channels made of repeating zig and zag segment running along the crystallographic *b*-axis, of which the pore diameter is about 5 Å.

5. CO_2/N_2 separations

MOF	Surface area $m^2\ g^{-1}$	Pore volume $cm^3\ g^{-1}$	Framework density $kg\ m^{-3}$	Data sources for unary isotherm fits	Comment
MgMOF-74	1669	0.607	909	[19, 27]	Intra-crystalline diffusion effects are not significant
NiMOF-74	1532	0.582	1194	[28, 29]	
NaX	950	0.280	1421	[19, 30]	
Kureha carbon	1300	0.56	1860	[15]	
Cu-SSZ13		0.253	1852	[31, 32]	Intra-crystalline diffusion effects are significant

MgMOF-74 (= Mg_2 (dobdc) = Mg\(dobdc) with dobdc = (dobdc4– = 1,4-dioxido-2,5-benzenedicarboxylate)), This MOF consists of one-dimensional hexagonal-shaped channels with free internal diameter of ca. 11 Å

NiMOF-74 = (Ni_2 (dobdc) = Ni\(dobdc) with dobdc = (dobdc4– = 1,4-dioxido-2,5-benzenedicarboxylate)). This MOF consists of one-dimensional hexagonal-shaped channels with free internal diameter of ca. 11 Å

NaX zeolite, also referred to as 13 X zeolite, has the FAU topology. The FAU topology consists of 785.7 $Å^3$ size cages separated by 7.4 Å size windows. Cage size is calculated on the basis of the equivalent sphere volume.

Kureha carbon is a commercially available, purely microporous material with pore-size distribution centered at 0.6 and 1.1 nm.[15]

Cu-SSZ13 has the CHA zeolite topology. CHA topology consists of 316.4 $Å^3$ size cages separated by 3.77 Å × 4.23 Å size windows.

6. $CO_2/N_2/SO_2$ separations

MOF	Surface area $m^2\ g^{-1}$	Pore volume $cm^3\ g^{-1}$	Framework density $kg\ m^{-3}$	Data sources for unary isotherm fits	Comment
NOTT-300	1370	0.433	1062	[33]	

NOTT-300 = $[Al_2(OH)_2(C_{16}O_8H_6)]$.[33] The pore dimensions are 6.5 Å × 6.5 Å.

7. CO_2/CH_4 separations

MOF	Surface area $m^2\ g^{-1}$	Pore volume $cm^3\ g^{-1}$	Framework density $kg\ m^{-3}$	Data sources for unary isotherm fits	Comment
MgMOF-74	1669	0.607	909	[19, 27]	Intra-crystalline diffusion effects are not significant
NiMOF-74	1532	0.582	1194	[28, 29]	
NaX	950	0.280	1421	[19, 30]	
CuBTC	2097	0.848	879	[19, 34]	
Cu-TDPAT	1938	0.93	782	[19, 35]	
Kureha carbon	1300	0.56	1860	[15]	

MgMOF-74 (= Mg_2 (dobdc) = Mg\(dobdc) with dobdc = (dobdc4– = 1,4-dioxido-2,5-benzenedicarboxylate)). This MOF consists of one-dimensional hexagonal-shaped channels with free internal diameter of ca. 11 Å

NiMOF-74 = (Ni_2 (dobdc) = Ni\(dobdc) with dobdc = (dobdc4– = 1,4-dioxido-2,5-benzenedicarboxylate)). This MOF consists of one-dimensional hexagonal-shaped channels with free internal diameter of ca. 11 Å

NaX zeolite, also referred to as 13 X zeolite, has the FAU topology. The FAU topology consists of 785.7 $Å^3$ size cages separated by 7.4 Å size windows. Cage size is calculated on the basis of the equivalent sphere volume.

CuBTC (=$Cu_3(BTC)_2$ with BTC = 1,3,5-benzenetricarboxylate, also known as HKUST-1) structure consists of two types of "cages" and two types of "windows" separating these cages. Large cages are inter-connected by 9 Å windows of square cross-section. The large cages are also connected to tetrahedral-shaped pockets of ca. 6 Å size through triangular-shaped windows of ca. 4.6 Å size

Cu-TDPAT =an rht-type metal−organic framework; H_6TDPAT = 2,4,6-tris(3,5-dicarboxylphenylamino)-1,3,5-triazine.

Kureha carbon is a commercially available, purely microporous material ,with pore-size distribution centered at 0.6 and 1.1 nm.[15]

The main manuscript compares separations at total pressures of 100 kPa and 2 MPa. Here, we also include comparisons with transient breakthroughs 600 kPa. Figure 5 presents a comparison of % CO_2 in the exit gas for fixed bed adsorber beds packed with different adsorbents, fed with 50/50 CO_2/CH_4 mixture, operating at 298 K and (a) p_t = 100 kPa, (b) p_t = 600 kPa, (c) p_t = 2 MPa. Figure 6 presents plots of the amount of CO_2 captured during the time interval 0 - τ_{break} as function of the dimensionless breakthrough time, τ_{break}, for fixed bed adsorber beds packed with different adsorbents, fed with 50/50 CO_2/CH_4 mixture, operating at 298 K and (a) p_t = 100 kPa, (b) p_t = 600 kPa, (c) p_t = 2 MPa. (c) 100 kPa, and (b) 2 MPa.

8. $CO_2/CH_4/H_2S$ separations

MOF	Surface area $m^2\ g^{-1}$	Pore volume $cm^3\ g^{-1}$	Framework density $kg\ m^{-3}$	Data sources for unary isotherm fits	Comment
NiMOF-74	1532	0.582	1194	[28, 29, 36]	Intra-crystalline diffusion effects are not significant
Amino-MIL-125 (Ti)	950	0.280	1421	[37]	

NiMOF-74 = (Ni_2 (dobdc) = Ni\(dobdc) with dobdc = (dobdc4– = 1,4-dioxido-2,5-benzenedicarboxylate)). This MOF consists of one-dimensional hexagonal-shaped channels with free internal diameter of ca. 11 Å.

Amino-MIL-125 (Ti) = MIL-125(Ti)-NH_2 = amino functionalized titanium terephthalate. MIL-125(Ti)-NH_2 exhibits a quasi-cubic tetragonal structure. The octahedral and tetrahedral cages with calculated free diameters of 10.7 Å and 4.7 Å are accessible through triangular windows of 5–7 Å.[37]

9. Separation of H_2 from $H_2/CO_2/CO/CH_4/N_2$ mixtures

MOF	Surface area $m^2\ g^{-1}$	Pore volume $cm^3\ g^{-1}$	Framework density $kg\ m^{-3}$	Data sources for unary isotherm fits	Comment
UTSA-16a extrudates	805	0.49	1171	The isotherm data used are from Agueda et al.[38]	Intra-crystalline diffusion effects are not significant
Cu-TDPAT	1938	0.93	782	[19, 35]	
NaX zeolite	950	0.280	1421	[19, 30]	
CuBTC	2097	0.848	879	[19, 39]	
Activated Carbon (AC)			1000	[40]	

The simulation details are provided in our earlier work. [5]

Cu-TDPAT =an rht-type metal−organic framework; H_6TDPAT = 2,4,6-tris(3,5-dicarboxylphenylamino)-1,3,5-triazine.

NaX zeolite, also referred to as 13 X zeolite, has the FAU topology. The FAU topology consists of 785.7 $Å^3$ size cages separated by 7.4 Å size windows. Cage size is calculated on the basis of the equivalent sphere volume.

CuBTC (=$Cu_3(BTC)_2$ with BTC = 1,3,5-benzenetricarboxylate, also known as HKUST-1) structure consists of two types of "cages" and two types of "windows" separating these cages. Large cages are inter-connected by 9 Å windows of square cross-section. The large cages are also connected to tetrahedral-shaped pockets of ca. 6 Å size through triangular-shaped windows of ca. 4.6 Å size.

The isotherm data for Activated Carbon are taken from Banu et al. [40]

Experimental confirmation that intra-crystalline diffusion effects are not of significant importance for H_2 purification processes is obtained by an analysis of the experimental data of Silva et al.[41] on the breakthrough characteristics of 3-component 35.5/47/17.5 $H_2/CO_2/CH_4$ mixture in adsorber packed with CuBTC at 303 K operating at a total pressure of 0.2 MPa; see Figure 7. The experimental data (symbols) are compared with breakthrough simulations (continuous solid lines) assuming thermodynamic equilibrium, i.e. invoking Equation (10); the agreement is very good. Silva et al.[41] also present a detailed model for breakthrough that include: intra-crystalline diffusion, axial dispersion in the fixed bed, along with a rigorous energy balance. Their simulation results, presented in Figure 4a of their paper, are hardly distinguishable from our own simulations using invoking Equation (10) that assumes thermodynamic equilibrium.

10. Fuel-cell grade H_2 production from $H_2/CO_2/CO$ mixtures

MOF	Surface area $m^2\ g^{-1}$	Pore volume $cm^3\ g^{-1}$	Framework density $kg\ m^{-3}$	Data sources for unary isotherm fits	Comment
UTSA-16a extrudates	805	0.49	1171	The isotherm data used are from Agueda et al.[38]	Intra-crystalline diffusion effects are not significant
Cu-TDPAT	1938	0.93	782	[19, 35]	
NaX zeolite	950	0.280	1421	[19, 30]	
CuBTC	2097	0.848	879	[19, 39]	
Activated Carbon (AC)			1000	[40]	

The simulation details are provided in our earlier work. [5]

Cu-TDPAT =an rht-type metal−organic framework; H_6TDPAT = 2,4,6-tris(3,5-dicarboxylphenylamino)-1,3,5-triazine.

NaX zeolite, also referred to as 13 X zeolite, has the FAU topology. The FAU topology consists of 785.7 $Å^3$ size cages separated by 7.4 Å size windows. Cage size is calculated on the basis of the equivalent sphere volume.

CuBTC (=$Cu_3(BTC)_2$ with BTC = 1,3,5-benzenetricarboxylate, also known as HKUST-1) structure consists of two types of "cages" and two types of "windows" separating these cages. Large cages are inter-connected by 9 Å windows of square cross-section. The large cages are also connected to tetrahedral-shaped pockets of ca. 6 Å size through triangular-shaped windows of ca. 4.6 Å size.

The isotherm data for Activated Carbon are taken from Banu et al. [40]

Figure 8a plots the ppm impurities in outlet gas as a function of the dimensionless time for separation of 3-component 73/16/11 $H_2/CO_2/CO$ mixtures. We aim for impurity levels < 10 ppm. [42]

Figure 8b compares the plots of the amount of H_2 captured (< 10 ppm impurities) per L of material during the time interval 0 - τ_{break} as function of the dimensionless breakthrough time, τ_{break} for separation of 3-component 73/16/11 $H_2/CO_2/CO$ mixtures. We note that NaX is the best adsorbent for production of fuel-cell grade hydrogen.

11. CO_2/CO mixture separations

MOF	Surface area $m^2\ g^{-1}$	Pore volume $cm^3\ g^{-1}$	Framework density $kg\ m^{-3}$	Data sources for unary isotherm fits	Comment
UTSA-16a extrudates	805	0.49	1171	The isotherm data used are from Agueda et al.[38]	Intra-crystalline diffusion effects are not significant
Cu-TDPAT	1938	0.93	782	[19, 35]	
NaX zeolite	950	0.280	1421	[19, 30]	
CuBTC	2097	0.848	879	[19, 39]	
Activated Carbon (AC)			1000	[40]	

The simulation details are provided in our earlier work. [5]

Cu-TDPAT =an rht-type metal−organic framework; H_6TDPAT = 2,4,6-tris(3,5-dicarboxylphenylamino)-1,3,5-triazine.

NaX zeolite, also referred to as 13 X zeolite, has the FAU topology. The FAU topology consists of 785.7 $Å^3$ size cages separated by 7.4 Å size windows. Cage size is calculated on the basis of the equivalent sphere volume.

CuBTC (=$Cu_3(BTC)_2$ with BTC = 1,3,5-benzenetricarboxylate, also known as HKUST-1) structure consists of two types of "cages" and two types of "windows" separating these cages. Large cages are inter-connected by 9 Å windows of square cross-section. The large cages are also connected to tetrahedral-shaped pockets of ca. 6 Å size through triangular-shaped windows of ca. 4.6 Å size.

The isotherm data for Activated Carbon are taken from Banu et al. [40]

Figure 9a presents a plot of ppm CO_2 in outlet gas as a function of the dimensionless time for separation of binary 50/50 CO_2/CO mixtures using five different adsorbent materials. CuBTC, NaX, Cu-TDPAT have nearly the same breakthrough times, that are significantly higher than that with UTSA-16a, and AC.

Figure 9b presents a plot of the amount of CO_2 captured per L of material during the time interval 0 - τ_{break} as function of the dimensionless breakthrough time, τ_{break}. NaX, CuBTC, and Cu-TDPAT have nearly the same CO_2 capture capabilities. The poorest CO_2 capture capability is that of AC.

12. C_2H_2/C_2H_4 separations at 298 K

MOF	Surface area $m^2\ g^{-1}$	Pore volume $cm^3\ g^{-1}$	Framework density $kg\ m^{-3}$	Data sources for unary isotherm fits	Comment
MgMOF-74	1669	0.607	909	[18]	Intra-crystalline diffusion effects are not significant
CoMOF-74	1448.5	0.515	1169	[18]	
FeMOF-74	1536	0.626	1126	[18]	
NOTT-300	1370	0.433	1062	The isotherm fits are from Table S13 of Yang.[43] The data is for 293 K.	
M'MOF3a	110	0.165	1023	[18]	
M'MOF4a		0.289	1126	[18]	
UTSA-100a	970	0.399	1146	[44]	

MgMOF-74 (= Mg_2 (dobdc) = Mg\(dobdc) with dobdc = (dobdc4– = 1,4-dioxido-2,5-benzenedicarboxylate)). This MOF consists of one-dimensional hexagonal-shaped channels with free internal diameter of ca. 11 Å

CoMOF-74 = (Co_2 (dobdc) = Co\(dobdc)) with dobdc = (dobdc4– = 1,4-dioxido-2,5-benzenedicarboxylate)). This MOF consists of one-dimensional hexagonal-shaped channels with free internal diameter of ca. 11 Å

FeMOF-74 (= Fe_2(dobdc) = Fe\(dobdc) with dobdc = (dobdc4– = 1,4-dioxido-2,5-benzenedicarboxylate)). This MOF consists of one-dimensional hexagonal-shaped channels with free internal diameter of ca. 11 Å

M'MOF3a = mixed metal organic-framework.[45] The pore dimensions are 3.4 Å × 4.8 Å

M'MOF4a = mixed metal organic-framework.[45]

NOTT-300 = $[Al_2(OH)_2(C_{16}O_8H_6)]$.[33] It has 6.5 Å × 6.5 Å channels.

UTSA-100a = a microporous MOF = [Cu(ATBDC)]; H_2ATBDC = 5-(5-Amino-1H-tetrazol-1-yl)-1,3-benzenedicarboxylic acid. [44] UTSA-100a has a three-dimensional framework with rhombic open zigzag nano-channels with amino and tetrazole functionalized wall running in the *c*-direction. The 1D open zigzag channels have a diameter of about 4.3 Å. There are smaller cages with the diameter of about 4.0 Å between the 1D channels with window openings of 3.3 Å.

The main manuscript examines 1/99 C_2H_2/C_2H_4 mixture separations. Figure 10 presents IAST, and breakthrough calculations for 50/50 C_2H_2/C_2H_4 mixtures using four different MOFs. We note that the highest capture capture capacity is achieved with MgMOF-74. These calculations demonstrate that uptake capacities are more important for 50.50 C_2H_2/C_2H_4 mixtures than for 1/99 C_2H_2/C_2H_4 mixtures.

13. C_2H_4/C_2H_6 and C_3H_6/C_3H_8 separations at 318 K

MOF	Surface area $m^2\ g^{-1}$	Pore volume $cm^3\ g^{-1}$	Framework density $kg\ m^{-3}$	Data sources for unary isotherm fits	Comment
MgMOF-74	1835	0.638	909	[46]	Intra-crystalline diffusion effects are not significant for thes MOFs
CoMOF-74	1438	0.51	1169	[46]	
FeMOF-74	1536	0.529	1126	[1, 46]	
NiMOF-74	1532	0.541	1206	[46]	
MnMOF-74	1797	0.628	1084	[46]	
ZnMOF-74	1277	0.451	1231	[46]	

The values above are reproduced from Tables S1 and S15 of Geier et al.[46]

Our simulations are carried out with the dual-Langmuir-Freundlich fit parameters in Tables S2, S3, S4, S5, S6, S7, S8, S9, S10, S11, S12, and S13.

MgMOF-74 (= Mg_2 (dobdc) = Mg\(dobdc) with dobdc = (dobdc4– = 1,4-dioxido-2,5-benzenedicarboxylate)). This MOF consists of one-dimensional hexagonal-shaped channels with free internal diameter of ca. 11 Å

CoMOF-74 = (Co_2 (dobdc) = Co\(dobdc)) with dobdc = (dobdc4– = 1,4-dioxido-2,5-benzenedicarboxylate)). This MOF consists of one-dimensional hexagonal-shaped channels with free internal diameter of ca. 11 Å

FeMOF-74 (= Fe_2(dobdc) = Fe\(dobdc) with dobdc = (dobdc4– = 1,4-dioxido-2,5-benzenedicarboxylate)). This MOF consists of one-dimensional hexagonal-shaped channels with free internal diameter of ca. 11 Å

NiMOF-74 = (Ni_2 (dobdc) = Ni\(dobdc) with dobdc = (dobdc4– = 1,4-dioxido-2,5-benzenedicarboxylate)). This MOF consists of one-dimensional hexagonal-shaped channels with free internal diameter of ca. 11 Å

MnMOF-74 (= Mn_2 (dobdc) = Mn\(dobdc)) with dobdc = (dobdc4– = 1,4-dioxido-2,5-benzenedicarboxylate)). This MOF consists of one-dimensional hexagonal-shaped channels with free internal diameter of ca. 11 Å

ZnMOF-74 (= Zn_2 (dobdc) = Zn\(dobdc)) with dobdc = (dobdc4– = 1,4-dioxido-2,5-benzenedicarboxylate)). This MOF consists of one-dimensional hexagonal-shaped channels with free internal diameter of ca. 11 Å.

Experimental data on the pure component isotherms for adsorption of C_2H_4,C_2H_6, C_3H_6, and C_3H_8 in six different iso-structural MOFs M-MOF-74 with M = Fe, Co, Ni, Zn, and Mn are available in the works of Bloch et al.[1], and Geier et al.[46] We shall use the pure component isotherm fits at 318 K to compare their relative performance for separations of 50/50 C_2H_4/C_2H_6, and 50/50 C_3H_6/C_3H_8 mixtures. The C_2H_4/C_2H_6 selectivities and volumetric C_2H_4 uptake capacities are compared in Figure 11a, and 11b. The highest selectivities are realized with FeMOF-74, and MnMOF-74. The higher volumetric uptake capacities are obtained with FeMOF-74, MnMOF-74, CoMOF-74, and NiMOF-74. Figures 11c presents a comparison of the % C_2H_4 in the exit gas from adsorber beds for the six different MOFs. Let us arbitrarily define the breakthrough time, τ_{break}, as the dimensionless time at which the % C_2H_4 in the exit gas is 1%. The longest breakthrough times, τ_{break}, are with FeMOF-74, MnMOF-74, CoMOF-74, and NiMOF-74; this appears to be dictated primarily the the hierarchy of volumetric uptake capacities. The shortest breakthrough times, τ_{break}, are with MgMOF-74 that has the lowest volumetric uptake capacity. The amount of C_2H_4 captured during the time interval 0 - τ_{break} can be determined from a material balance. These amounts, expressed as mol C_2H_4 captured per L of framework material are plotted against τ_{break} in Figures 11d. The highest capture C_2H_4 capacities are realized with FeMOF-74, MnMOF-74, CoMOF-74, and NiMOF-74 primarily because of high uptake capacities. By the same token, the lowest C_2H_4 capture capacity is realized with MgMOF-74 primarily because of its low volumetric uptake capacity.The C_3H_6/C_3H_8 selectivities and volumetric C_3H_6 uptake capacities are compared in Figures 12a, and 12b. The highest selectivities are realized with MnMOF-74, and FeMOF-74. The higher volumetric uptake capacities are obtained with NiMOF-74, FeMOF-74, and MnMOF-74. Figures 12c presents a comparison of the % C_3H_6 in the exit gas from adsorber beds for the six different MOFs. Let us arbitrarily define the breakthrough time, τ_{break}, as the dimensionless time at which the % C_3H_6 in the exit gas is 1%. The longest breakthrough times, τ_{break}, are with NiMOF-74,

FeMOF-74, and MnMOF-74; this appears to be dictated primarily the the hierarchy of volumetric uptake capacities. MgMOF-74, CoMOF-74, and FeMOF-74 primarily because of the higher uptake capacities. The shortest breakthrough times, τ_{break}, are with MgMOF-74 that has the lowest volumetric uptake capacity. The amount of C_3H_6 captured during the time interval 0 - τ_{break} can be determined from a material balance. These amounts, expressed as mol C_3H_6 captured per L of framework material are plotted against τ_{break} in Figures 12d. The highest capture C_3H_6 capacities are realized with NiMOF-74, FeMOF-74, and MnMOF-74 primarily because of high uptake capacities. By the same token, the lowest C_3H_6 capture capacity is realized with MgMOF-74 primarily because of its low volumetric uptake capacity.From the foregoing analyses of separation of C_2H_4/C_2H_6, and C_3H_6/C_3H_8 mixtures we conclude that M-MOF-74 have good potential for selective adsorption of unsaturated alkenes from mixtures with the corresponding saturated alkanes of the same chain length.

The energy requirements are high because of the significantly higher binding energy of the alkenes; this is reflected in the isosteric heats of adsorption; see Figure 13.

14. C_2H_4/C_2H_6 separations at 298 K

MOF	Surface area $m^2\ g^{-1}$	Pore volume $cm^3\ g^{-1}$	Framework density $kg\ m^{-3}$	Data sources for unary isotherm fits	Comment
MgMOF-74	1669	0.607	909	[18]	
CoMOF-74	1448.5	0.5146	1169	[18]	
FeMOF-74	1536	0.626	1126	[18]	
CuBTC	2097	0.848	879	[18]	
NOTT-300	1370	0.433	1062	The isotherm fits are from Table S13 of Yang.[43] The data is for 293 K.	
PAF-1-SO3Ag	1938	0.93	1070	[47]	
MIL-101-Cr-SO3Ag	1374	0.56	700	[48]	

Since the Geier et al. [46] data for MgMOF-74, CoMOF-74, and FeMOF-74 are available only for the lowest temperature of 318 K, the isotherm fits used for the simulations at 298 K are from the parameters presented by He et al.[18]

MgMOF-74 (= Mg_2 (dobdc) = Mg\(dobdc) with dobdc = (dobdc4– = 1,4-dioxido-2,5-benzenedicarboxylate)). This MOF consists of one-dimensional hexagonal-shaped channels with free internal diameter of ca. 11 Å

CoMOF-74 = (Co_2 (dobdc) = Co\(dobdc)) with dobdc = (dobdc4– = 1,4-dioxido-2,5-benzenedicarboxylate)). This MOF consists of one-dimensional hexagonal-shaped channels with free internal diameter of ca. 11 Å

FeMOF-74 (= Fe_2(dobdc) = Fe\(dobdc) with dobdc = (dobdc4– = 1,4-dioxido-2,5-benzenedicarboxylate)). This MOF consists of one-dimensional hexagonal-shaped channels with free internal diameter of ca. 11 Å

CuBTC (=$Cu_3(BTC)_2$ with BTC = 1,3,5-benzenetricarboxylate, also known as HKUST-1) structure consists of two types of "cages" and two types of "windows" separating these cages. Large cages are inter-connected by 9 Å windows of square cross-section. The large cages are also connected to tetrahedral-shaped pockets of ca. 6 Å size through triangular-shaped windows of ca. 4.6 Å size.

PAF-1-SO3Ag introduces π-complexation into highly porous PAF-122 with Ag(I) ions.[47]

MIL-101–Cr–SO3Ag was afforded via Ag(I) ion exchange of the sulphonic acid functionalized MIL-101–Cr.[48]

NOTT-300 = $[Al_2(OH)_2(C_{16}O_8H_6)]$.[33, 43] It has 6.5 Å × 6.5 Å channels. The isotherm data are available at 293 K.[43]

15. O_2/N_2 separations

MOF	Surface area $m^2\ g^{-1}$	Pore volume $cm^3\ g^{-1}$	Framework density $kg\ m^{-3}$	Data sources for unary isotherm fits	Comment
LTA-4A = RS-10	900	0.25	1529	[49, 50]	Diffusional effects are significant. Inter-cage hopping occurs one-molecule-at-a-time
LTA-5A	900	0.25	1508	[51-53]	Diffusional effects are significant. Inter-cage hopping occurs one-molecule-at-a-time
FeMOF-74	1536	0.626	1126	[54]	Diffusional effects are not of significant importance

LTA consists of 743.05 $Å^3$ size cages separated by 4 Å windows.

The adsorption and diffusion data for LTA-4A are for commercially available RS-10 that is a modified version of LTA-4A that affords higher diffusion selectivity in favor of O2; the data are taken from Farooq et al. [49, 50]

FeMOF-74 (= Fe_2(dobdc) = Fe\(dobdc) with dobdc = (dobdc4– = 1,4-dioxido-2,5-benzenedicarboxylate)). This MOF consists of one-dimensional hexagonal-shaped channels with free internal diameter of ca. 11 Å

Further simulation details are provided in our earlier work.[5]

16. N_2/CH_4 separations

MOF	Surface area $m^2\ g^{-1}$	Pore volume $cm^3\ g^{-1}$	Framework density $kg\ m^{-3}$	Data sources for unary isotherm fits	Comment
LTA-4A	900	0.25	1529	[55]	Diffusional effects are significant. Inter-cage hopping occurs one-molecule-at-a-time

LTA consists of 743.05 $Å^3$ size cages separated by 4 Å windows.

The simulation details are provided in our earlier work.[5] In these simulations the published data on unary isotherms and diffusivities[55] are used.

17. Separation of hexane isomers

MOF	Surface area $m^2\ g^{-1}$	Pore volume $cm^3\ g^{-1}$	Framework density $kg\ m^{-3}$	Data sources for unary isotherm fits	Comment
MFI	658	0.165	1796	CBMC simulations of isotherms at 433 K.[5]	Diffusional effects are significant for guest diffusion in the 5.5 Å channels.
ZIF-77	541	0.189	1553		Diffusional effects are significant for guest diffusion in the 4.5 Å channels.
$Fe_2(BDP)_3$		0.25	1145	Experimental data of Herm at 403 K, 433 K, and 473 K. These data are fitted with *T*-dependent parameters.[5]	Diffusional effects are significant for guest diffusion in the 4.9 Å triangular channels.

The simulation details are provided in our earlier work.[5]

MFI zeolite consists of 10-ring intersecting channels of 5.1 Å – 5.5 Å and 5.3 Å – 5.6 Å size.

The modelling of diffusion within the intersecting channels of MFI zeolite need to take proper account of synergy between adsorption and diffusion. For this purpose, the thermodynamic correction factors need to be accounted for, as described in detail in our earlier work.

$Fe_2(BDP)_3$ has one-dimensional triangular-shaped channels with free internal diameter of ca. 4.9 Å.

The main manuscript presents calculations of the RON of the gas exiting the fixed bed adsorber. These calculations are bassed on the transient breakthrough characteristics (cf Figure 14), with inclusion of diffusional limitations, for 5-component nC6/2MP/3MP/22DMB/23DMB mixture in a fixed bed adsorber packed with (a) Fe2(BDP)3, (b) ZIF-77, and (c) MFI zeolite a total pressure of 100 kPa and 433 K. The partial pressures of the components in the bulk gas phase operating at the inlet are $p_1 = p_2 = p_3 = p_4 = p_5 = 20$ kPa.

18. Separations of xylene isomers

MOF	Surface area $m^2\ g^{-1}$	Pore volume $cm^3\ g^{-1}$	Framework density $kg\ m^{-3}$	Data sources for unary isotherm fits	Comment
MAF-X8	1465	0.4947	954.29	CBMC simulated isotherms at 433 K.[56]	
BaX zeolite			1480	Experimental data at 393 K and 453 K. [57, 58]	
DynaMOF-100		0.626	1105	Experimental data on pure component isotherms at 298 K.[59]	
Mg-CUK-1	602	0.626	1142	Experimental data on pure component isotherms at 323 K.[60]	

MAF-X8 is a Zn(II) pyrazolate-carboxylate framework whose synthesis has been reported by He et al. [61] Within the one-dimensional 10 Å channels of MAF-X8, we have commensurate stacking of p-xylene.[56]

BaX is a cation-exchanged Faujasite zeolite. The FAU topology consists of 785.7 Å3 size cages separated by 7.4 Å size windows. Cage size is calculated on the basis of the equivalent sphere volume.

DynaMOF-100 consists of a Zn(II)-based dynamic coordination framework, [Zn4O(L)3] where the ligand L = 4, 4'- ((4-(tert-butyl) - 1,2- phenylene)bis(oxy))dibenzoate)

Mg-CUK-1 is the Mg(II) version of the porous coordination polymer CUK-1, synthesized by Saccoccia et al. [60] It has 1D pores of 8 Å size. It is to be noted that the isotherm data for Mg-CUK-1 is not available for ethylbenzene. In this case we adopt the following definition of selectivity for o-xylene(1)/m-xylene(2)/p-xylene(3) mixtures

$$S_{ads} = \frac{(q_3)/(q_1+q_2)}{(p_3)/(p_1+p_2)} = 2\frac{(q_3)}{(q_1+q_2)}$$

19. Styrene/ethylbenzene separations

MOF	Surface area $m^2\ g^{-1}$	Pore volume $cm^3\ g^{-1}$	Framework density $kg\ m^{-3}$	Data sources for unary isotherm fits	Comment
MIL-47(V)			1004	Experimental data at 298 K.[62] The original experiment data has been refitted; these parameters are used. [59]	The original experiment data has been refitted; [59] these parameters are used.
MIL-53(Al)			1041		
DynaMOF-100		0.626	1105	Experimental data on pure component isotherms at 298 K.[59]	

DynaMOF-100 consists of a Zn(II)-based dynamic coordination framework, [Zn4O(L)3] where the ligand L = 4, 4'- ((4-(tert-butyl) - 1,2- phenylene)bis(oxy))dibenzoate)

MIL-47 has one-dimensional diamond-shaped channels with free internal diameter of ca 8.5 Å

MIL-53 has one-dimensional diamond-shaped channels with free internal diameter of ca 8.5 Å

20. Benzene/cyclohexane separations

MOF	Surface area $m^2\ g^{-1}$	Pore volume $cm^3\ g^{-1}$	Framework density $kg\ m^{-3}$	Data sources for unary isotherm fits	Comment
AgY zeolite			1400	Data is available at 393 K;[63]	The experiment data has been refitted; these parameters are used.
PAF-2			740	Ren et al.[64]	
MnTriazolate			1422	Lin et al.[65]	

Cyclohexane, and important industrial chemical, is produced by catalytic hydrogenation of benzene. The unreacted benzene is present in the effluent from the reactor must be removed from the desired product. The separation of benzene and cyclohexane is difficult because the differences in the boiling points is only 0.6 K (cf. Figure 15). Currently technologies use extractive distillation with entrainers such as sulpholane, dimethylsulfoxide, N-methylpyrrolidone, and N-formylmorpholine; such processes are energy intensive. Adsorptive separations offer the energy-efficient alternatives to extractive distillation, especially for mixtures containing small percentage of benzene, as is commonly encountered.

Takahashi and Yang[63] have presented pure component isotherm data for benzene and cyclohexane to show that cation-exchange Faujasites Na-Y, Pd-Y, and Ag-Y zeolites have high selectivity for adsorption of benzene, due to π-complexation; cyclohexane does not form π-complexes.

An alternative to cation-exchange Faujasites, as suggested by Ren et al.[64] is to use a porous aromatic framework, PAF-2. The pure component isotherm data for PAF-2 shown in Figure 2b of Ren et al.[64] indicate that the saturation capacity of benzene is much higher than that of cyclohexane; this is perhaps due to molecular packing effects. Figure 15 shows the molecular structures of benzene and cyclohexane; it appears that stacking of flat benzene molecules is easier than stacking cyclohexanes in either the boat or chair configurations. In addition to molecular packing effects, the higher π–π interaction between the benzene molecule and the aromatic framework of PAF-2 also contributes to good separations.

Lin et al.[65] present the pure component isotherm data for benzene and cyclohexane for Mn triazolate MOF that also indicates a sign indicate that the saturation capacity of benzene is much higher than that of cyclohexane.

Figure 16 compares the transient breakthrough characteristics, for benzene/cyclohexane mixtures in fixed bed adsorbers packed with (a) AgY zeolite operating at 393 K, (b) PAF-2 operating at 298 K, and (c) MnTriazolate operating at 298 K. Since the data are not at the same temperatures it is difficult to compare these in a proper manner. Of the two MOFs investigated, MnTriazolate appears to have superior separation capabilities.

21. Notation

A	cross-sectional area of breakthrough tube, m^2
c_i	molar concentration of species i in gas mixture, mol m^{-3}
c_{i0}	molar concentration of species i in gas mixture at inlet to adsorber, mol m^{-3}
d	internal diameter of breakthrough tube, m
$Đ_i$	Maxwell-Stefan diffusivity, m^2 s^{-1}
L	length of packed bed adsorber, m
m_{ads}	mass of adsorbent packed into the breakthrough apparatus, kg
n	number of species in the mixture, dimensionless
N_i	molar flux of species i, mol m^{-2} s^{-1}
p_i	partial pressure of species i in mixture, Pa
p_t	total system pressure, Pa
q_i	component molar loading of species i, mol kg^{-1}
$q_{i,sat}$	molar loading of species i at saturation, mol kg^{-1}
q_t	total molar loading in mixture, mol kg^{-1}
$q_{sat,A}$	saturation loading of site A, mol kg^{-1}
$q_{sat,B}$	saturation loading of site B, mol kg^{-1}
$\bar{q}_i(t)$	*spatially averaged* component molar loading of species i, mol kg^{-1}
Q_{He}	volumetric flow rate of inert gas He, m^3 s^{-1}
Q_{st}	isosteric heat of adsorption, J mol^{-1}
Q_t	total volumetric flow rate, m^3 s^{-1}
r	radial direction coordinate, m
r_c	radius of crystallite, m
R	gas constant, 8.314 J mol^{-1} K^{-1}
t	time, s
T	absolute temperature, K

u	superficial gas velocity in packed bed, m s^{-1}
V_{ads}	volume of adsorbent packed into the breakthrough apparatus, m^3
y_i	mole fraction of species *i* in gas mixture, mol m^{-3}
z	distance along the adsorber, and along membrane layer, m

Greek letters

ε	voidage of packed bed, dimensionless
ρ	framework density, kg m^{-3}
τ	time, dimensionless
v	interstitial gas velocity in packed bed, m s^{-1}

22. References

(1) Bloch, E. D.; Queen, W. L.; Krishna, R.; Zadrozny, J. M.; Brown, C. M.; Long, J. R. Hydrocarbon Separations in a Metal-Organic Framework with Open Iron(II) Coordination Sites, *Science* **2012**, *335*, 1606-1610.

(2) Herm, Z. R.; Wiers, B. M.; Van Baten, J. M.; Hudson, M. R.; Zajdel, P.; Brown, C. M.; Maschiocchi, N.; Krishna, R.; Long, J. R. Separation of Hexane Isomers in a Metal-Organic Framework with Triangular Channels *Science* **2013**, *340*, 960-964.

(3) Gücüyener, C.; van den Bergh, J.; Gascon, J.; Kapteijn, F. Ethane/Ethene Separation Turned on Its Head: Selective Ethane Adsorption on the Metal-Organic Framework ZIF-7 through a Gate-Opening Mechanism, *J. Am. Chem. Soc.* **2010**, *132*, 17704-17706.

(4) Yang, J.; Krishna, R.; Li, J.; Li, J. Experiments and Simulations on Separating a CO_2/CH_4 Mixture using K-KFI at Low and High Pressures, *Microporous Mesoporous Mater.* **2014**, *184*, 21-27.

(5) Krishna, R. The Maxwell-Stefan Description of Mixture Diffusion in Nanoporous Crystalline Materials, *Microporous Mesoporous Mater.* **2014**, *185*, 30-50.

(6) Krishna, R.; Long, J. R. Screening metal-organic frameworks by analysis of transient breakthrough of gas mixtures in a fixed bed adsorber, *J. Phys. Chem. C* **2011**, *115*, 12941-12950.

(7) Krishna, R.; Baur, R. Modelling issues in zeolite based separation processes, *Sep. Purif. Technol.* **2003**, *33*, 213-254.

(8) Krishna, R. Separating Mixtures by Exploiting Molecular Packing Effects in Microporous Materials, *Phys. Chem. Chem. Phys.* **2015**, *17*, 39-59.

(9) Gu, Z.-Y.; Yang, C.-X.; Chang, N.; Yan, X.-P. Metal-Organic Frameworks for Analytical Chemistry: From Sample Collection to Chromatographic Separation, *Acc. Chem. Res.* **2012**, *45*, 734-745.

(10) Chang, N.; Gu, Z.-Y.; Yan, X.-P. Zeolitic Imidazolate Framework-8 Nanocrystal Coated Capillary for Molecular Sieving of Branched Alkanes from Linear Alkanes along with High-Resolution Chromatographic Separation of Linear Alkanes, *J. Amer. Chem. Soc.* **2010**, *132*, 13645-13647.

(11) Gu, Z. Y.; Yan, X. P. Metal–Organic Framework MIL-101 for High-Resolution Gas-Chromatographic Separation of Xylene Isomers and Ethylbenzene, *Angew. Chem. Int. Ed.* **2010**, *49*, 1477-1480.

(12) Gu, Z. Y.; Jiang, D. Q.; Wang, H. F.; Cui, X. Y.; Yan, X. P. Adsorption and Separation of Xylene Isomers and Ethylbenzene on Two Zn-Terephthalate Metal-Organic Frameworks, *J. Phys. Chem. C* **2010**, *114*, 311-316.

(13) Myers, A. L.; Prausnitz, J. M. Thermodynamics of Mixed Gas Adsorption, *A.I.Ch.E.J.* **1965**, *11*, 121-130.

(14) Chen, D.-L.; Shang, H.; Zhu, W.; Krishna, R. Transient Breakthroughs of CO_2/CH_4 and C_3H_6/C_3H_8 Mixtures in Fixed Beds packed with Ni-MOF-74, *Chem. Eng. Sci.* **2014**, *117*, 407-415.

(15) Yu, H.; Wang, X.; Xu, C.; Chen, D.-L.; Zhu, W.; Krishna, R. Utilizing transient breakthroughs for evaluating the potential of Kureha carbon for CO_2 capture, *Chem. Eng. J.* **2015**, *269*, 135-147.

(16) Li, P.; He, Y.; Zhao, Y.; Weng, L.; Wang, H.; Krishna, R.; Wu, H.; Zhou, W.; O'Keeffe, M.; Han, Y.; Chen, B. A Rod-Packing Microporous Hydrogen-Bonded Organic Framework for Highly Selective Separation of C_2H_2/CO_2 at Room Temperature, *Angew. Chem. Int. Ed.* **2015**, *54*, 574-577.

(17) Duan, X.; Zhang, Q.; Cai, J.; Yang, Y.; Cui, Y.; He, Y.; Wu, C.; Krishna, R.; Chen, B.; Qian, G. A New Metal–Organic Framework with Potential for Adsorptive Separation of Methane from

Carbon Dioxide, Acetylene, Ethylene, and Ethane Established by Simulated Breakthrough Experiments, *J. Mater. Chem. A* **2014**, *2*, 2628-2633.

(18) He, Y.; Krishna, R.; Chen, B. Metal-Organic Frameworks with Potential for Energy-Efficient Adsorptive Separation of Light Hydrocarbons, *Energy Environ. Sci.* **2012**, *5*, 9107-9120.

(19) Kong, G. Q.; Han, Z. D.; He, Y.; Qu, S.; Zhou, W.; Yildirim, T.; Krishna, R.; Zou, C.; Wu, C. D.; Chen, B. Expanded Organic Building Units for the Construction of Highly Porous Metal-Organic Frameworks, *Chem. Eur. J.* **2013**, *19*, 14886-14894.

(20) Duan, J.; Jin, W.; Krishna, R. Natural Gas Purification Using a Porous Coordination Polymer with Water and Chemical Stability, *Inorg. Chem.* **2015**, *54*, 4279-4284.

(21) Xia, T.; Cai, J.; Wang, H.; Duan, X.; Cui, Y.; Yang, Y.; Qian, G. Microporous Metal-Organic Frameworks with Suitable Pore Spaces for Acetylene Storage and Purification, *Microporous Mesoporous Mater.* **2015**, *XXX*, XXX-XXX. http://dx.doi.org/doi:10.1016/j.micromeso.2015.05.036.

(22) Liu, J.; Strachan, D. M.; Thallapally, P. K. Enhanced noble gas adsorption in Ag@MOF-74Ni, *Chem. Commun.* **2014**, *50*, 466-468.

(23) Liu, J.; Thallapally, P. K.; Strachan, D. Metal−Organic Frameworks for Removal of Xe and Kr from Nuclear Fuel Reprocessing Plants, *Langmuir* **2012**, *28*, 11584-11589.

(24) Gurdal, Y.; Keskin, S. Atomically Detailed Modeling of Metal Organic Frameworks for Adsorption, Diffusion, and Separation of Noble Gas Mixtures, *Ind. Eng. Chem. Res.* **2012**, *51*, 7373-8382.

(25) Chen, X.; Plonka, A. M.; Banerjee, D.; Krishna, R.; Schaef, H. T.; Ghose, D.; Thallapally, P. K.; Parise, J. B. Direct Observation of Xe and Kr Adsorption in a Xe-selective Microporous Metal Organic Framework, *J. Am. Chem. Soc.* **2015**, *XX*, XXX-XXX. http://dx.doi.org/doi:10.1021/jacs.5b02556.

(26) Wang, H.; Yao, K.; Zhang, Z.; Jagiello, J.; Gong, Q.; Han, Y.; Li, J. The First Example of Commensurate Adsorption of Atomic Gas in a MOF and Effective Separation of Xenon from Other Noble Gases, *Chem. Sci.* **2014**, *5*, 620-624.

(27) Mason, J. A.; Sumida, K.; Herm, Z. R.; Krishna, R.; Long, J. R. Evaluating Metal-Organic Frameworks for Post-Combustion Carbon Dioxide Capture via Temperature Swing Adsorption, *Energy Environ. Sci.* **2011**, *4*, 3030-3040.

(28) Dietzel, P. D. C.; Besikiotis, V.; Blom, R. Application of metal–organic frameworks with coordinatively unsaturated metal sites in storage and separation of methane and carbon dioxide, *J. Mater. Chem.* **2009**, *19*, 7362-7370.

(29) Krishna, R.; van Baten, J. M. Investigating the Relative Influences of Molecular Dimensions and Binding Energies on Diffusivities of Guest Species Inside Nanoporous Crystalline Materials *J. Phys. Chem. C* **2012**, *116*, 23556-23568.

(30) Belmabkhout, Y.; Pirngruber, G.; Jolimaitre, E.; Methivier, A. A complete experimental approach for synthesis gas separation studies using static gravimetric and column breakthrough experiments, *Adsorption* **2007**, *13*, 341-349.

(31) Hudson, M. R.; Murray, L.; Mason, J. A.; Fickel, D. W.; Lobo, R. F.; Queen, W. L.; Brown, C. M. Unconventional and Highly Selective CO_2 Adsorption in Zeolite SSZ-13, *J. Am. Chem. Soc.* **2012**, *134*, 1970-1973.

(32) Xiang, S. C.; He, Y.; Zhang, Z.; Wu, H.; Zhou, W.; Krishna, R.; Chen, B. Microporous Metal-Organic Framework with Potential for Carbon Dioxide Capture at Ambient Conditions, *Nat. Commun.* **2012**, *3*, 954. http://dx.doi.org/doi:10.1038/ncomms1956.

(33) Yang, S.; Sun, J.; Ramirez-Cuesta, A. J.; Callear, S. K.; David, W. I. F.; Anderson, D. P.; Newby, R.; Blake, A. J.; Parker, J. E.; Tang, C. C.; Schröder, M. Selectivity and direct visualization of carbon dioxide and sulfur dioxide in a decorated porous host, *Nature Chemistry* **2012**, *4*, 887-894.

(34) Krishna, R. Adsorptive separation of $CO_2/CH_4/CO$ gas mixtures at high pressures, *Microporous Mesoporous Mater.* **2012**, *156*, 217-223.

(35) Wu, H.; Yao, K.; Zhu, Y.; Li, B.; Shi, Z.; Krishna, R.; Li, J. Cu-TDPAT, an *rht*-type Dual-Functional Metal–Organic Framework Offering Significant Potential for Use in H_2 and Natural Gas Purification Processes Operating at High Pressures, *J. Phys. Chem. C* **2012**, *116*, 16609-16618.

(36) Chavan, S.; Bonino, F.; Valenzano, L.; Civalleri, B.; Lamberti, C.; Acerbi, N.; Cavka, J. H.; Leistner, M.; Bordiga, S. Fundamental Aspects of H_2S Adsorption on CPO-27-Ni, *J. Phys. Chem. C* **2013**, *117*, 15615-15622.

(37) Vaesen, S.; Guillerm, V.; Yang, Q.; Wiersum, A. D.; Marszalek, B.; Gil, B.; Vimont, A.; Daturi, M.; Devic, T.; Llewellyn, P. L.; Serre, C.; Maurin, G.; De Weireld, G. A robust amino-functionalized titanium(IV) based MOF for improved separation of acid gases, *Chem. Commun.* **2013**, *49*, 10082-10084.

(38) Agueda, V. I.; Delgado, J. A.; Uguina, M. A.; Brea, P.; Spjelkavik, A. I.; Blom, R.; Grande, C. Adsorption and diffusion of H_2, N_2, CO, CH_4 and CO_2 in UTSA-16 metal-organic framework extrudates, *Chem. Eng. Sci.* **2015**, *124*, 159-169.

(39) Moellmer, J.; Moeller, A.; Dreisbach, F.; Glaeser, R.; Staudt, R. High pressure adsorption of hydrogen, nitrogen, carbon dioxide and methane on the metal–organic framework HKUST-1, *Microporous Mesoporous Mater.* **2011**, *138*, 140-148.

(40) Banu, A. M.; Friedrich, D.; Brandani, S.; Düren, T. A Multiscale Study of MOFs as Adsorbents in H_2 PSA Purification, *Ind. Eng. Chem. Res.* **2013**, *52*, 9946-9957.

(41) Silva, B.; Salomon, I.; Ribeiro, A. M.; Chang, J. S.; Loureiro, J. M.; Rodrigues, A. E. H_2 purification by Pressure Swing Adsorption using CuBTC, *Sep. Purif. Technol.* **2013**, *118*, 744-756.

(42) Majlan, E. H.; Daud, W. R. W.; Iyuke, S. E.; Mohamad, A. B.; Kadhum, A. H.; Mohammad, A. W.; Takriff, M. S.; Bahaman, N. Hydrogen purification using compact pressure swing adsorption system for fuel cell, *Int. J. Hydrogen Energy* **2009**, *34*, 2771-2777.

(43) Yang, S.; Ramirez-Cuesta, A. J.; Newby, R.; Garcia-Sakai, V.; Manuel, P.; Callear, S. K.; Campbell, S. I.; Tang, C. C.; Schröder, M. Supramolecular binding and separation of hydrocarbons within a functionalized porous metal–organic framework, *Nature Chemistry* **2014**, *7*, 121-129.

(44) Hu, T.-L.; Wang, H.; Li, B.; Krishna, R.; Wu, H.; Zhou, W.; Zhao, Y.; Han, Y.; Wang, X.; Zhu, W.; Yao, Z.; Xiang, S. C.; Chen, B. A microporous metal-organic framework with dual functionalities for highly efficient removal of acetylene from ethylene/acetylene mixtures at room temperature, *Nat. Commun.* **2015**, *6*, 7328. http://dx.doi.org/doi:10.1038/ncomms8328.

(45) Das, M. C.; Guo, Q.; He, Y.; Kim, J.; Zhao, C. G.; Hong, K.; Xiang, S.; Zhang, Z.; Thomas, K. M.; Krishna, R.; Chen, B. Interplay of Metalloligand and Organic Ligand to Tune Micropores within Isostructural Mixed-Metal Organic Frameworks (M'MOFs) for Their Highly Selective Separation of Chiral and Achiral Small Molecules, *J. Am. Chem. Soc.* **2012**, *134*, 8703-8710.

(46) Geier, S. J.; Mason, J. A.; Bloch, E. D.; Queen, W. L.; Hudson, M. R.; Brown, C. M.; Long, J. R. Selective adsorption of ethylene over ethane and propylene over propane in the metal–organic frameworks M_2(dobdc) (M = Mg, Mn, Fe, Co, Ni, Zn), *Chem. Sci.* **2013**, *4*, 2054-2061.

(47) Li, B.; Zhang, Y.; Krishna, R.; Yao, K.; Han, Y.; Wu, Z.; Ma, D.; Shi, Z.; Pham, T.; Space, B.; Liu, J.; Thallapally, P. K.; Liu, J.; Chrzanowski, M.; Ma, S. Introduction of Π-Complexation into Porous Aromatic Framework for Highly Selective Adsorption of Ethylene over Ethane, *J. Am. Chem. Soc.* **2014**, *136*, 8654-8660.

(48) Zhang, Y.; Li, B.; Krishna, R.; Wu, Z.; Ma, D.; Shi, Z.; Pham, T.; Forrest, K.; Space, B.; Ma, S. Highly Selective Adsorption of Ethylene over Ethane in a MOF Featuring the Combination of Open Metal Site and π-Complexation, *Chem. Commun.* **2015**, *51*, 2714-2717.

(49) Farooq, S.; Rathor, M. N.; Hidajat, K. A Predictive Model for a Kinetically Controlled Pressure Swing Adsorption Separation Process, *Chem. Eng. Sci.* **1993**, *48*, 4129-4141.

(50) Farooq, S. Sorption and Diffusion of Oxygen and Nitrogen in Molecular- Sieve RS-10, *Gas Sep. Purif.* **1995**, *9*, 205-212.

(51) Rama Rao, V.; Farooq, S.; Krantz, W. B. Design of a Two-Step Pulsed Pressure-Swing Adsorption-Based Oxygen Concentrator, *A.I.Ch.E.J.* **2010**, *56*, 354-370.

(52) Rama Rao, V. Adsorption based portable oxygen concentrator for personal medical applications, Ph.D. Dissertation, National University of Singapore, Singapore, 2011.

(53) Farooq, S.; Ruthven, D. M.; Boniface, H. A. Numerical-Simulation of a Pressure Swing Adsorption Oxygen Unit, *Chem. Eng. Sci.* **1989**, *44*, 2809-2816.

(54) Bloch, E. D.; Murray, L.; Queen, W. L.; Chavan, S. M.; Maximoff, S. N.; Bigi, J. P.; Krishna, R.; Peterson, V. K.; Grandjean, F.; Long, G. J.; Smit, B.; Bordiga, S.; Brown, C. M.; Long, J. R. Selective Binding of O_2 over N_2 in a Redox-Active Metal-Organic Framework with Open Iron(II) Coordination Sites, *J. Am. Chem. Soc.* **2011**, *133*, 14814-14822.

(55) Habgood, H. W. The Kinetics of Molecular Sieve Action. Sorption of Nitrogen-Methane Mixtures by Linde Molecular Sieve 4A, *Canad. J. Chem.* **1958**, *36*, 1384-1397.

(56) Torres-Knoop, A.; Krishna, R.; Dubbeldam, D. Separating Xylene Isomers by Commensurate Stacking of p-Xylene within Channels of MAF-X8, *Angew. Chem. Int. Ed.* **2014**, *53*, 7774-7778.

(57) Minceva, M.; Rodrigues, A. E. Understanding and Revamping of Industrial Scale SMB Units for p-Xylene Separation, *A.I.Ch.E.J.* **2007**, *53*, 138-149.

(58) Minceva, M.; Rodrigues, A. E. Adsorption of xylenes on Faujasite-type zeolite. Equilibrium and Kinetics in Batch Adsorber, *Chem. Eng. Res. Des.* **2004**, *82*, 667-681.

(59) Mukherjee, S.; Joarder, B.; Desai, A. V.; Manna, B.; Krishna, R.; Ghosh, S. K. Exploiting Framework Flexibility of a Metal-Organic Framework for Selective Adsorption of Styrene over Ethylbenzene, *Inorg. Chem.* **2015**, *54*, 4403-4408.

(60) Saccoccia, B.; Bohnsack, A. M.; Waggoner, N. W.; Cho, K. H.; Lee, J. S.; Hong, D.-Y.; Lynch, V. M.; Chang, J.-S.; Humphrey, S. M. Separation of p-Divinylbenzene by Selective Room-Temperature Adsorption Inside Mg-CUK-1 Prepared by Aqueous Microwave Synthesis, *Angew. Chem. Int. Ed.* **2015**, *54*, 5394-5398.

(61) He, C.-T.; Tian, J. Y.; Liu, S. Y.; Ouyang, G.; Zhang, J.-P.; Chen, X. M. A porous coordination framework for highly sensitive and selective solid-phase microextraction of non-polar volatile organic compounds, *Chem. Sci.* **2013**, *4*, 351-356.

(62) Maes, M.; Vermoortele, F.; Alaerts, L.; Couck, S.; Kirschhock, C. E. A.; Denayer, J. F. M.; De Vos, D. E. Separation of Styrene and Ethylbenzene on Metal-Organic Frameworks: Analogous Structures with Different Adsorption Mechanisms, *J. Am. Chem. Soc.* **2010**, *132*, 15277-15285.

(63) Takahashi, A.; Yang, R. T. New Adsorbents for Purification: Selective Removal of Aromatics, *A.I.Ch.E.J.* **2002**, *48*, 1457-1468.

(64) Ren, H.; Ben, T.; Wang, E.; Jing, X.; Xue, M.; Liu, B.; Cui, Y.; Qui, S.; Zhu, G. Targeted synthesis of a 3D porous aromatic framework for selective sorption of benzene, *Chem. Commun.* **2010**, *46*, 291-293.

(65) Lin, J.-B.; Zhang, J.-P.; Zhang, W.-X.; Wei Xue, W.; Xue, D.-X.; Chen, X.-M. Porous Manganese(II) 3-(2-Pyridyl)-5-(4-Pyridyl)-1,2,4-Triazolate Frameworks: Rational Self-Assembly, Supramolecular Isomerism, Solid-State Transformation, and Sorption Properties, *Inorg. Chem.* **2009**, *46*, 6852-6660.

23. Caption for Figures

Figure 1. Schematic of a packed bed adsorber.

Figure 2. Schematic of the breakthrough tube. The tube diameter is 4.65 mm, and tube length L = 100 mm. The mass of adsorbent used in the bed is: NiMOF-74 = 576.1 mg, and Kureha carbon = 760 mg. The gas phase used in the experiments consisted of CO_2/CH_4/He mixtures. The gas phase compositions at the inlet were maintained at 25/25/50.The flow rate of He was maintained constant at 4 mL min^{-1} at STP conditions.

Figure 3. Experimental breakthroughs of Chen et al.[14] and Yu et al.[15] for CO_2(1)/CH_4(2)/He(3) mixtures in packed bed with NiMOF-74, and Kureha carbon at 298 K. The partial pressures at the inlet are $p_1 = p_2$ = 50 kPa; p_3 = 100 kPa. In (a) the y-axis represents the % CO_2 in the exit gas phase, excluding the presence of inert gas He. In (b) the y-axis represents the % CH_4 in the exit gas phase, excluding the presence of inert gas He. As indicated for NiMOF-74, it is possible to produce CH_4 with 99% purity during the time interval between t_1, and t_2. (c) The CO_2 captured is plotted against the dimensionless breakthrough time.

Figure 4. (a, b) Calculations using the Ideal Adsorbed Solution Theory (IAST) of (a) adsorption selectivity, S_{ads}, and (b) uptake capacity of C_2H_2, for separation of 50/50 C_2H_2/CO_2 mixture at 296 K

using HOF-3, CuBTC, ZJU-60a, PCP-33, and Cu_2TPTC-Me. (c) Comparison of % C_2H_2 in the exit gas for beds packed with HOF-3, CuBTC, ZJU-60a, and PCP-33 plottted as a function of the dimensionless breakthrough time.

Figure 5. Comparison of % CO_2 in the exit gas for fixed bed adsorber beds packed with different adsorbents, fed with 50/50 CO_2/CH_4 mixture, operating at 298 K and (a) p_t = 100 kPa, (b) p_t = 600 kPa, (c) p_t = 2 MPa.

Figure 6. Plots of the amount of CO_2 captured during the time interval 0 - τ_{break} as function of the dimensionless breakthrough time, τ_{break}, for fixed bed adsorber beds packed with different adsorbents, fed with 50/50 CO_2/CH_4 mixture, operating at 298 K and (a) p_t = 100 kPa, (b) p_t = 600 kPa, (c) p_t = 2 MPa. (c) 100 kPa, and (b) 2 MPa.

Figure 7. Adsorption/desorption breakthrough characteristics of 3-component 35.5/47/17.5 $H_2/CO_2/CH_4$ mixture in adsorber packed with CuBTC at 303 K operating at a total pressure of 0.2 MPa. The desorption phase is initiated at time t = 6550 s, the 3-component mixture is switched to pure H_2. The experimental data of Silva et al.[41] (symbols) are compared with breakthrough simulations (continuous solid lines) assuming thermodynamic equilibrium, i.e. invoking Equation (10). The experimental conditions correspond to Run 5 of Silva et al[41]: L = 0.31 m; voidage of bed, ε = 0.52; interstitial gas velocity, v = 0.0305 m/s. The isotherm data for CuBTC are from the Silva paper.

Figure 8. (a) Ppm (CO_2 + CO) in outlet gas as a function of the dimensionless time for separation of 3-component 73/16/11 $H_2/CO_2/CO$ mixtures using five different adsorbent materials. (b) Plot of the amount of H_2 produced (< 10 ppm impurities) per L of material during the time interval 0 - τ_{break} as function of the dimensionless breakthrough time, τ_{break} for separation of 3-component 73/16/11 $H_2/CO_2/CO$ mixtures.

Figure 9.(a) Ppm CO_2 in outlet gas as a function of the dimensionless time for separation of binary 50/50 CO_2/CO mixtures using five different adsorbent materials. (b) Plots of the amount of CO_2 captured (< 500 ppm impurities) per L of material during the time interval 0 - τ_{break} as function of the dimensionless breakthrough time, τ_{break}.

Figure 10. (a) IAST calculations of the adsorption selectivity, S_{ads}, of 50/50 C_2H_2/C_2H_4 mixtures using four different MOFs. (b) C_2H_2 uptake capacity of 50/50 C_2H_2/C_2H_4 mixtures. (c) Comparison of % C_2H_2 in the exit gas from adsorber beds. (d) Plot of the amount of C_2H_2 captured during the time interval 0 - τ_{break} as function of the dimensionless breakthrough time, τ_{break}.

Figure 11. (a, b) IAST calculations of (a) adsorption selectivity, S_{ads}, and (b) C_3H_6 uptake capacity in 50/50 C_2H_4/C_2H_6 mixtures at 318 K using six different M-MOF-74 with M = Fe, Co, Ni, Zn, and Mn. (c) Comparison of C_2H_4 in the exit gas from adsorber beds. (d) Plot of the amount of C_2H_4 captured during the time interval 0 - τ_{break} as function of the dimensionless breakthrough time, τ_{break}.

Figure 12. (a, b) IAST calculations of (a) adsorption selectivity, S_{ads}, and (b) C_3H_6 uptake capacity in 50/50 C_3H_6/C_3H_8 mixtures at 318 K using six different M-MOF-74 with M = Fe, Co, Ni, Zn, and Mn. (c) Comparison of % C_3H_6 in the exit gas from adsorber beds. (d) Plot of the amount of C_3H_6 captured during the time interval 0 - τ_{break} as function of the dimensionless breakthrough time, τ_{break}.

Figure 13. Isosteric heat of adsorption of (a, b) C_2H_4, and (c) C_3H_6 in a variety of MOFs.

Figure 14. Transient breakthrough characteristics, with inclusion of diffusional limitations, for 5-component nC6/2MP/3MP/22DMB/23DMB mixture in a fixed bed adsorber packed with (a) $Fe_2(BDP)_3$, (b) ZIF-77, and (c) MFI zeolite a total pressure of 100 kPa and 433 K. The partial pressures of the components in the bulk gas phase operating at the inlet are $p_1 = p_2 = p_3 = p_4 = p_5 = 20$ kPa.

Figure 15. Molecular structures of benzene and cyclohexane. Also indicated are the boiling points and freezing points.

Figure 16. Transient breakthrough characteristics, for benzene/cyclohexane mixtures in fixed bed adsorbers packed with (a) AgY zeolite operating at 393 K, (b) PAF-2 operating at 298 K, and (c) MnTriazolate operating at 298 K. The total pressure is 100 kPa.

ESI Figure 1

Fixed bed adsorber

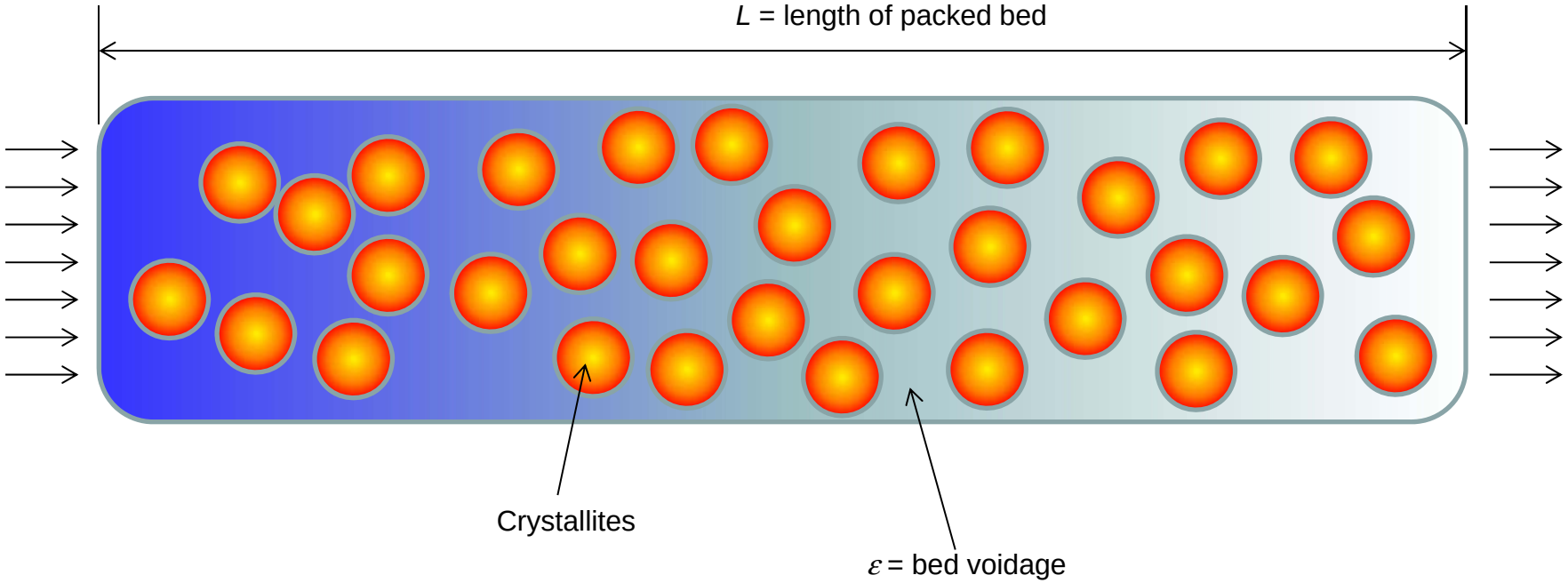

u =
superficial
gas
velocity

v = *u*/*ε* = interstitial gas velocity

L/*v* =
Characteristic time of contact between gas and liquid

ESI Figure 2

Breakthrough apparatus

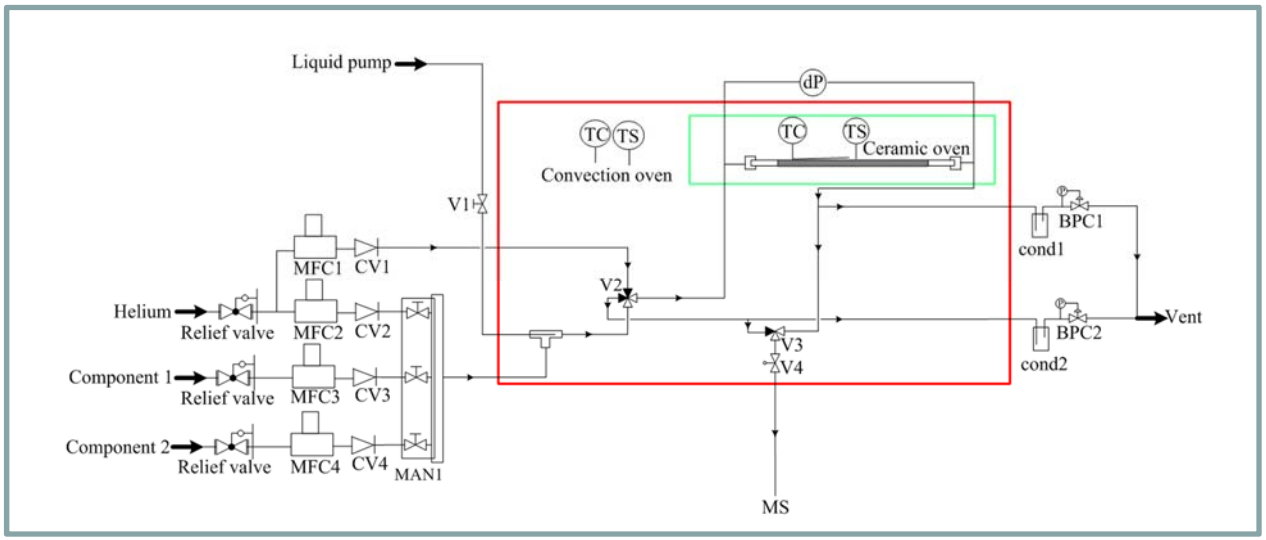

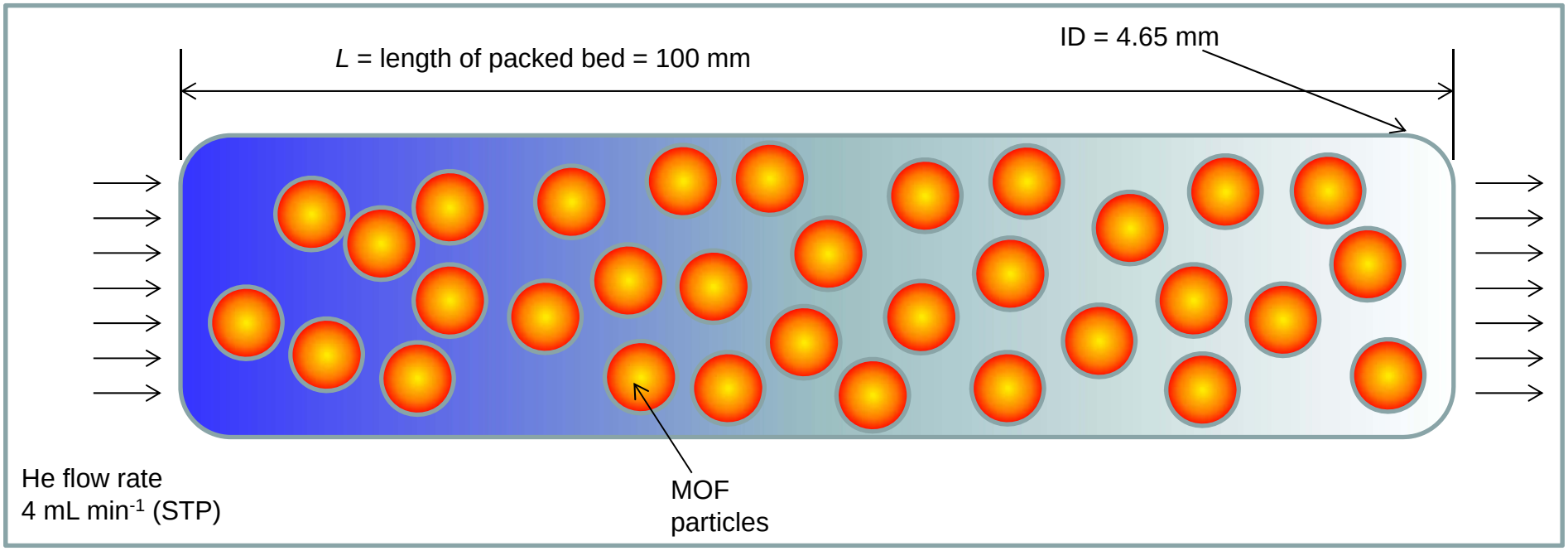

Breakthrough experiments

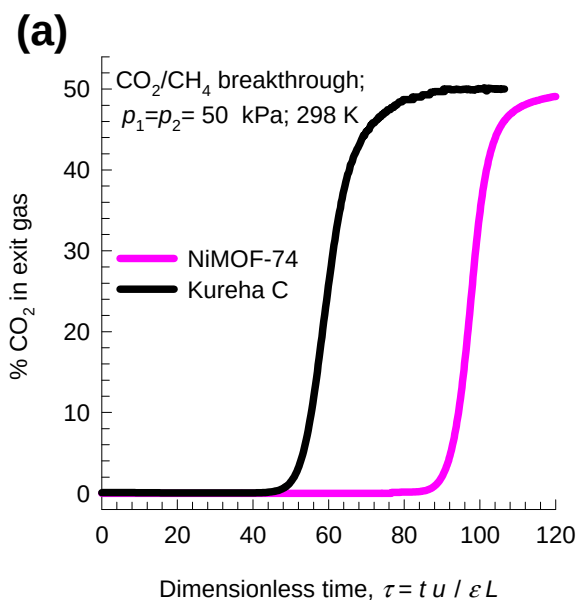

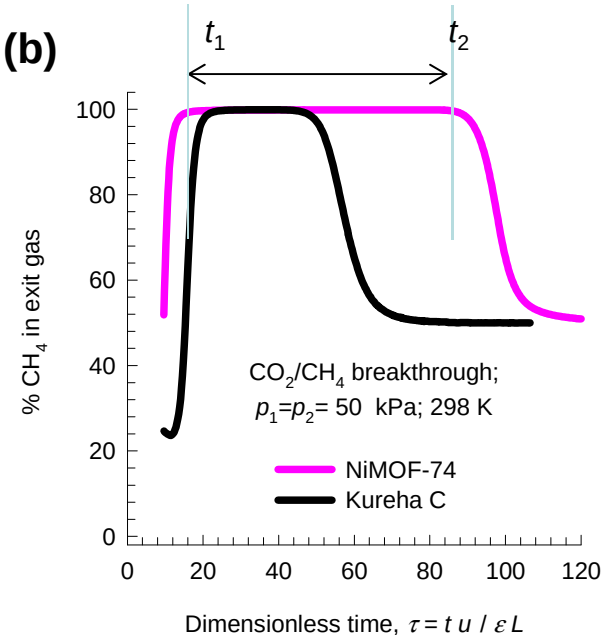

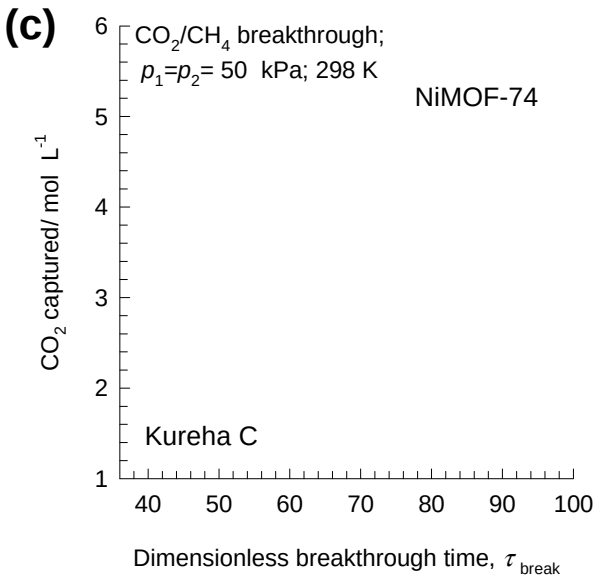

ESI Figure 4

C_2H_2/CO_2 separations: comparisons including Cu_2TPTC-Me

(a)

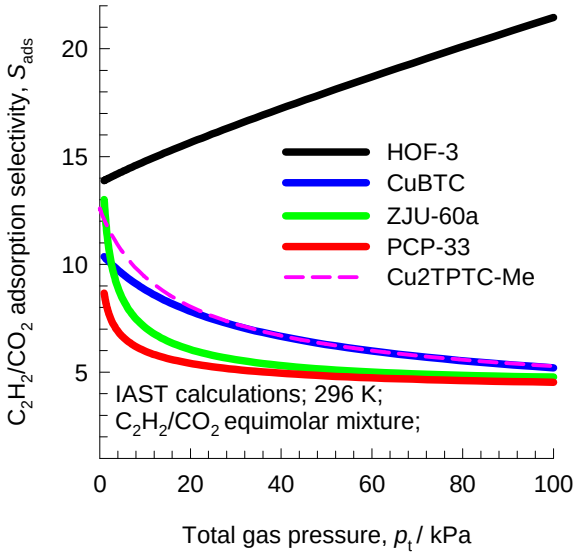

(b)

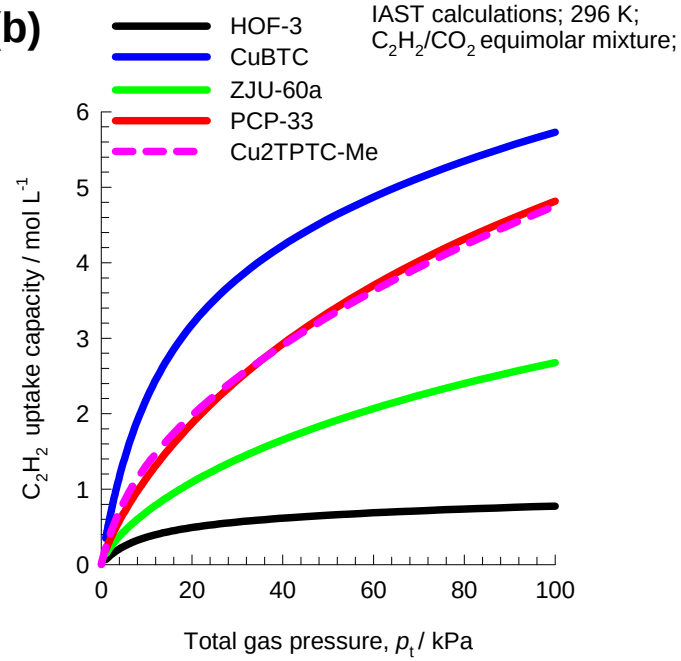

(c)

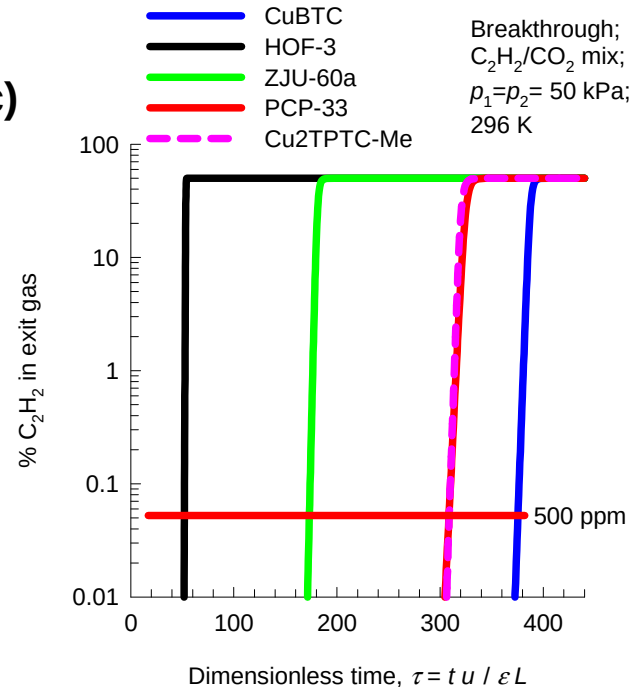

ESI Figure 5

CO_2/CH_4 separations at three different pressures

(a)

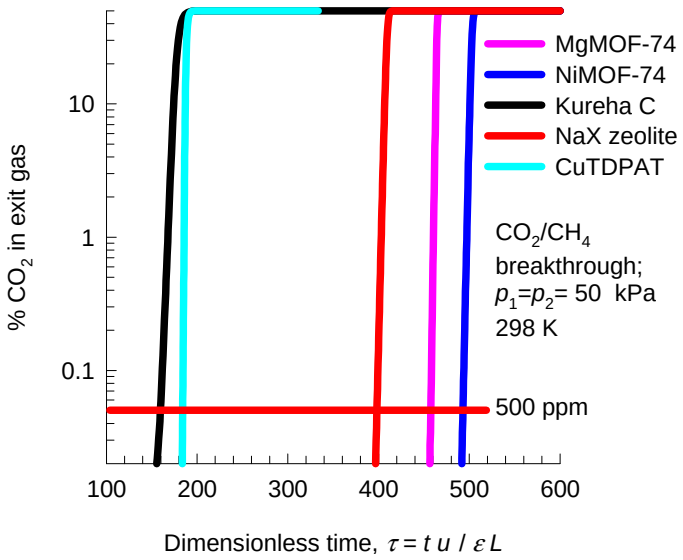

(b)

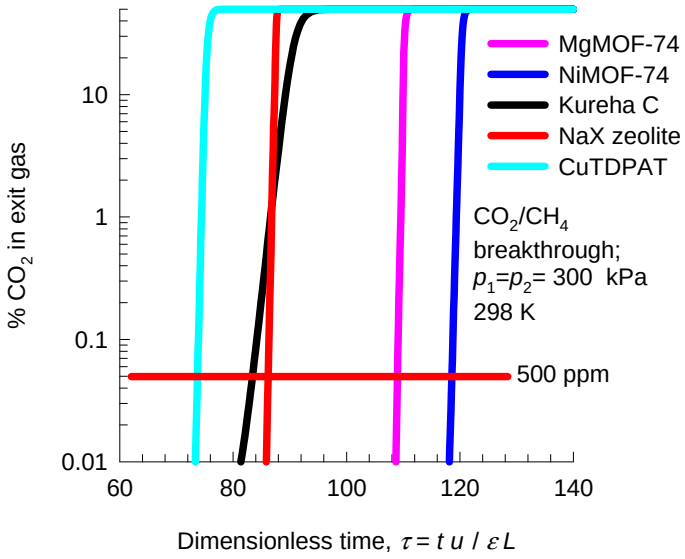

(c)

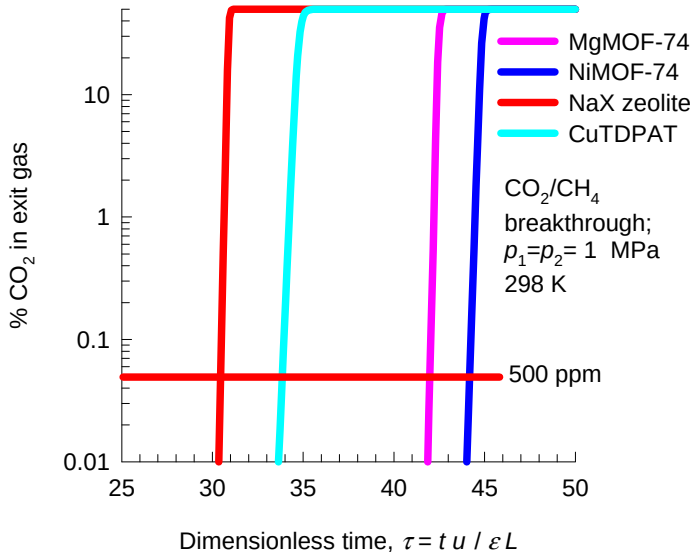

ESI Figure 6

CO_2/CH_4 separations at three different pressures

(a)

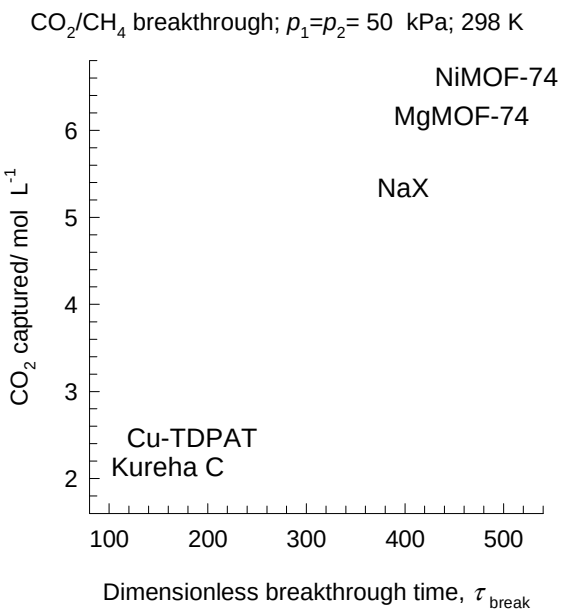

(b)

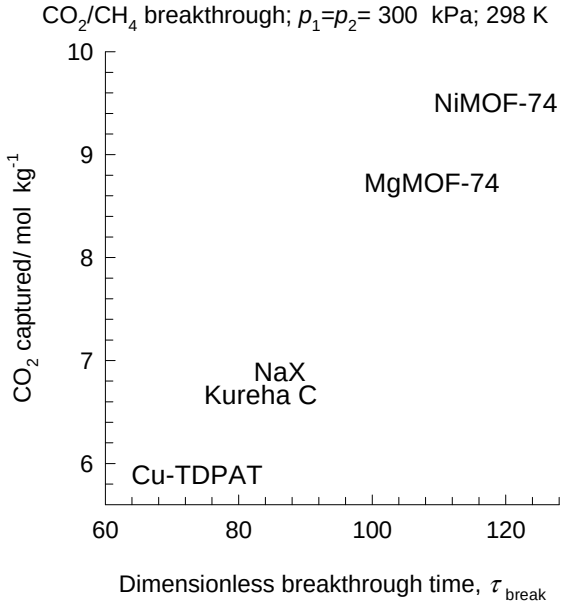

(c)

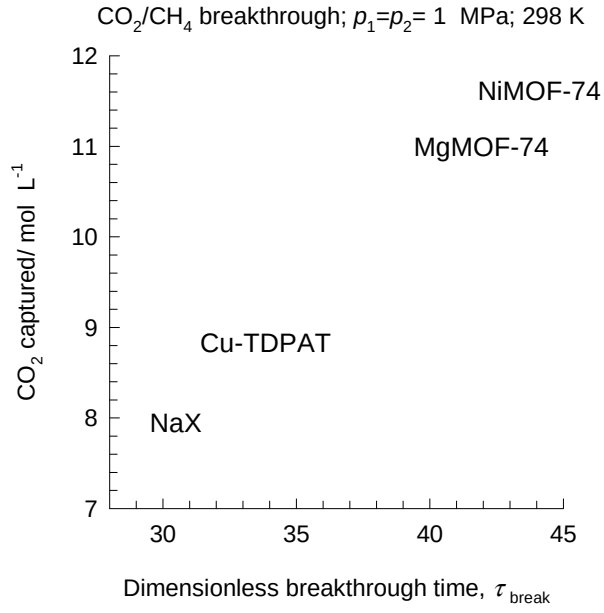

Breakthrough H_2 purification CuBTC

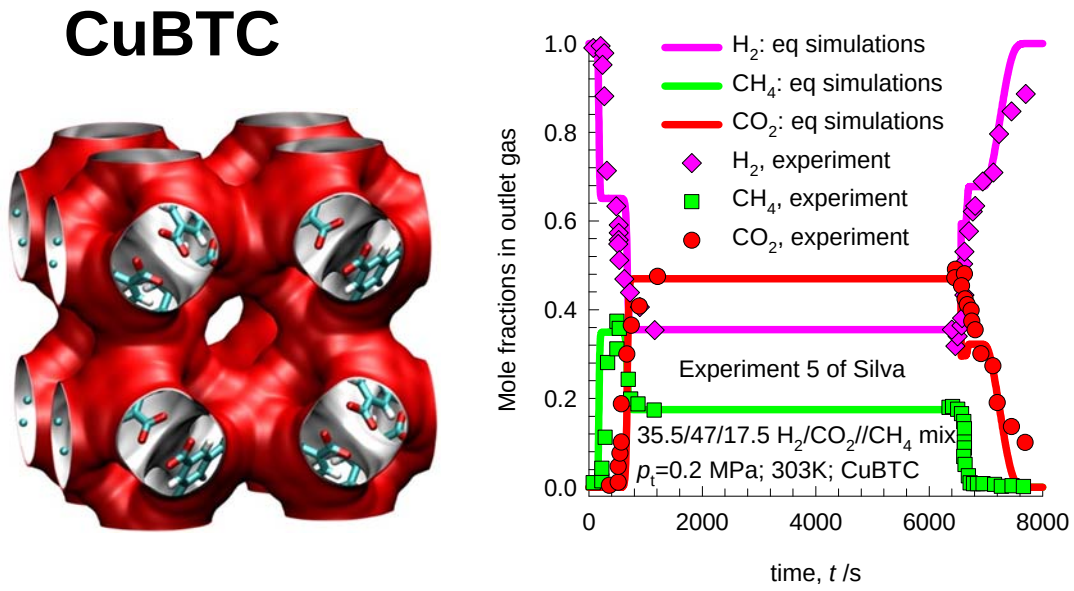

Fuel-cell grade H_2 production

ESI Figure 8

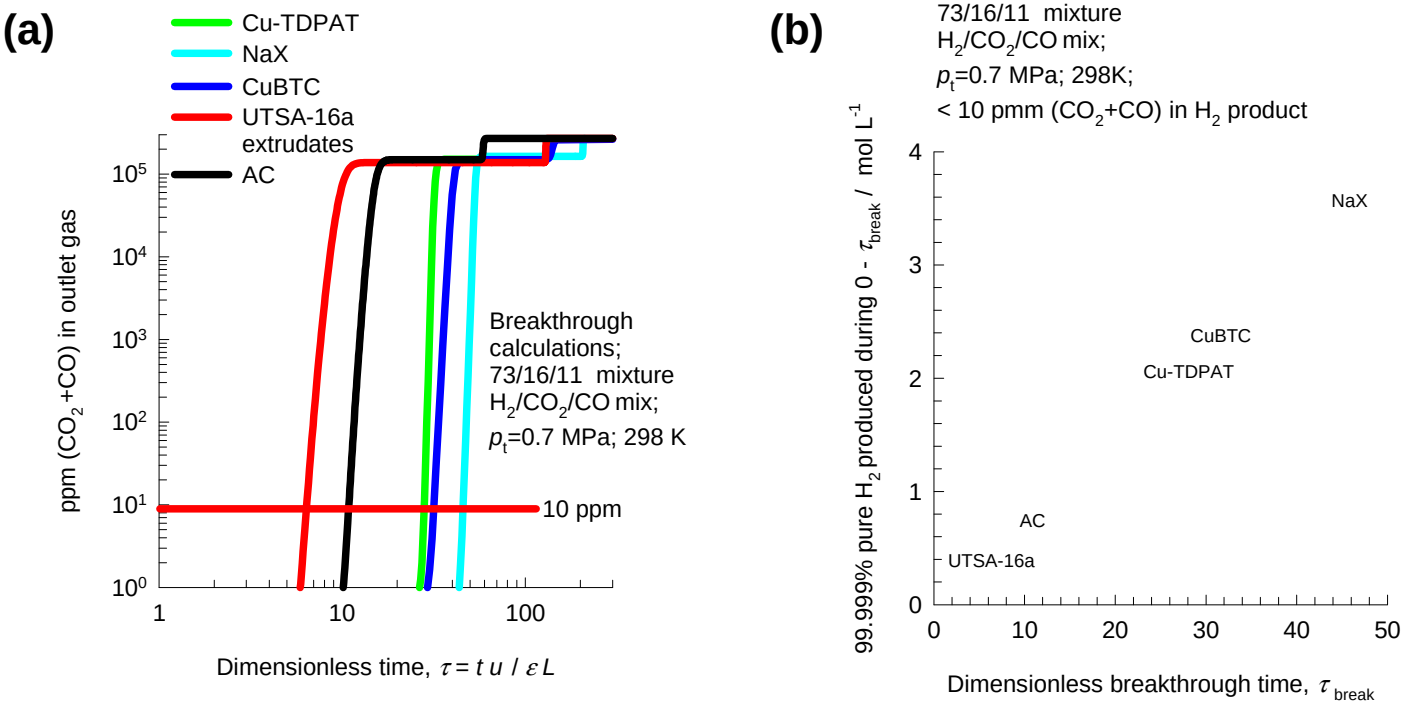

CO_2/CO mixture separations

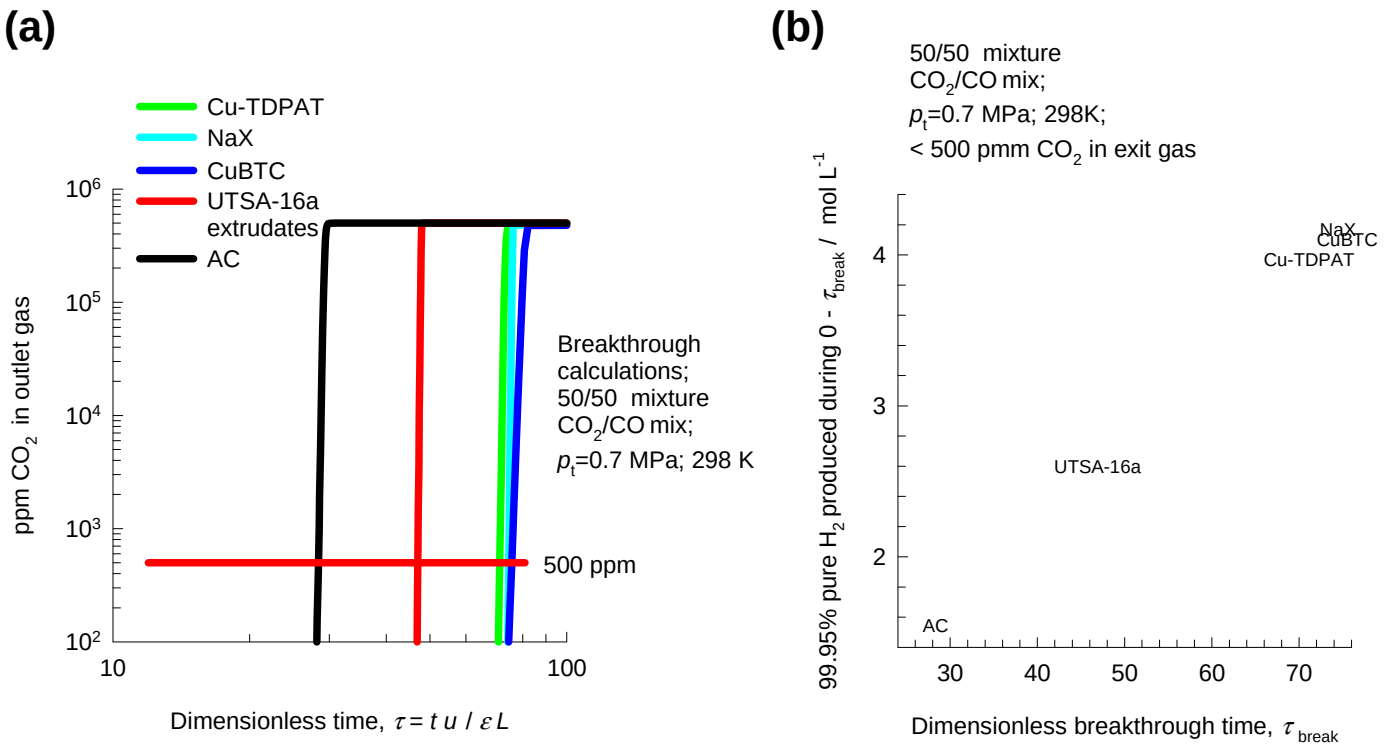

ESI Figure 10

C_2H_2/C_2H_4 separations for 50/50 mixtures

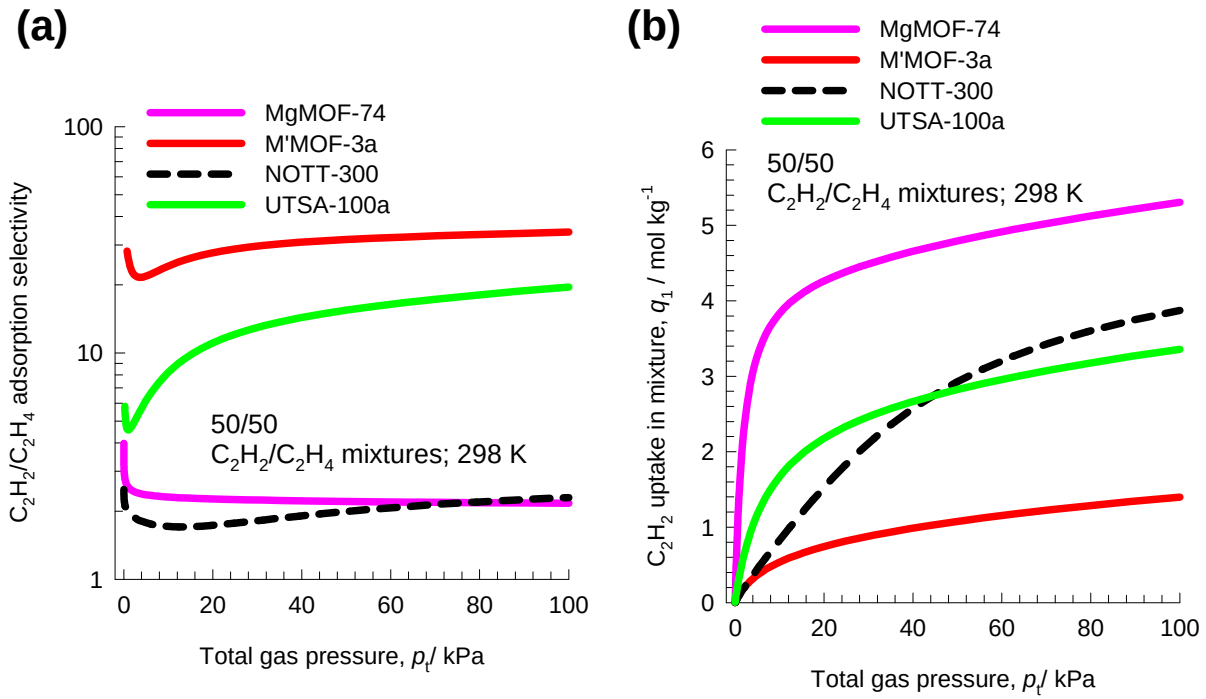

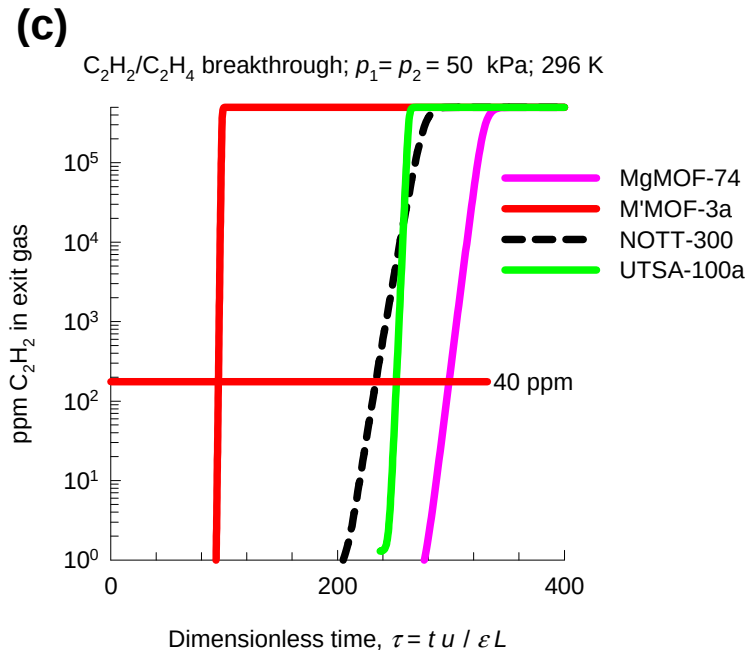

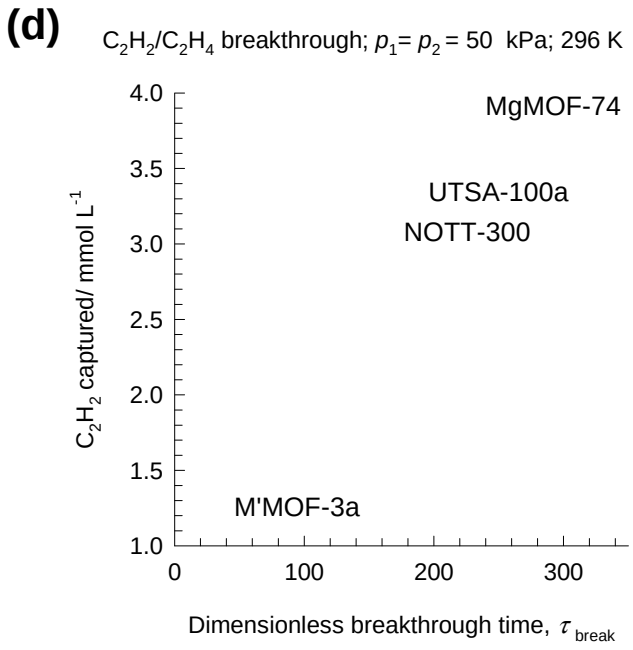

ESI Figure 11

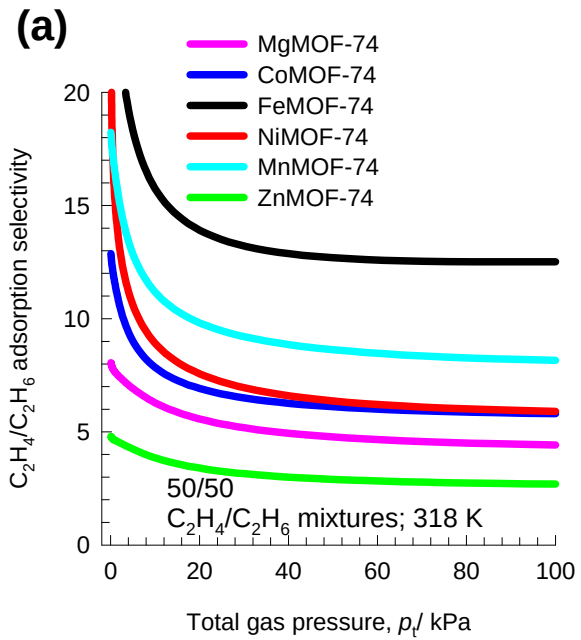

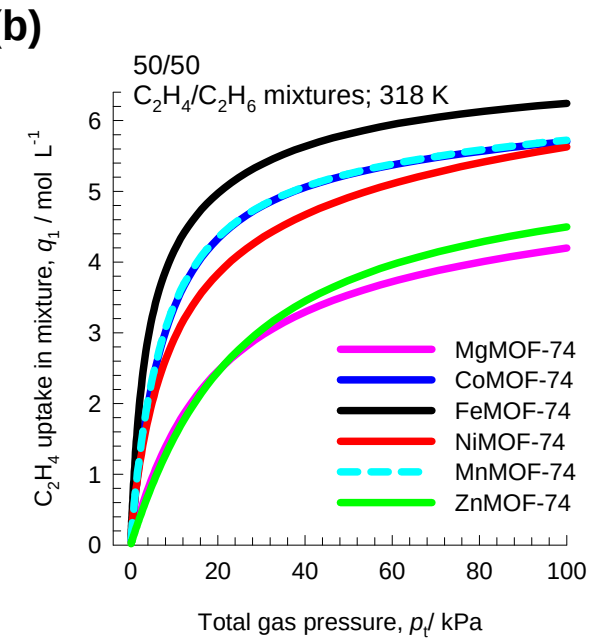

C_2H_4/C_2H_6 separations for 50/50 mixtures

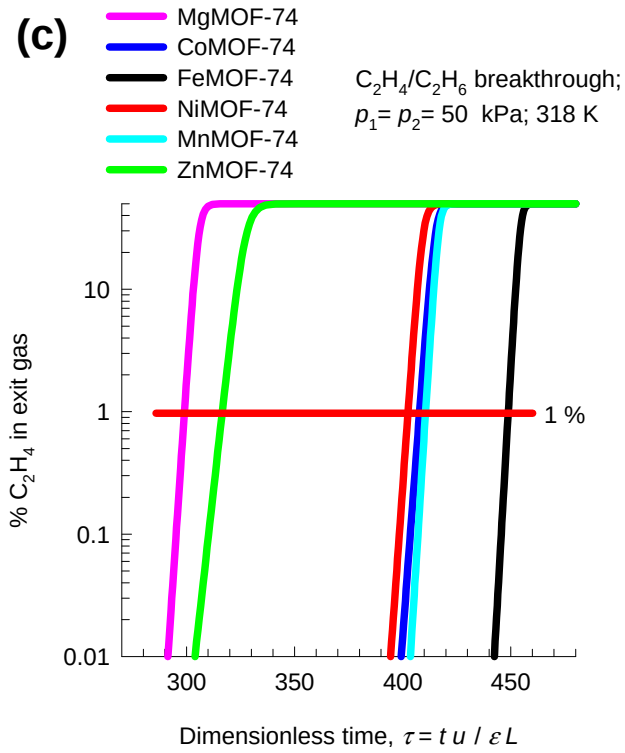

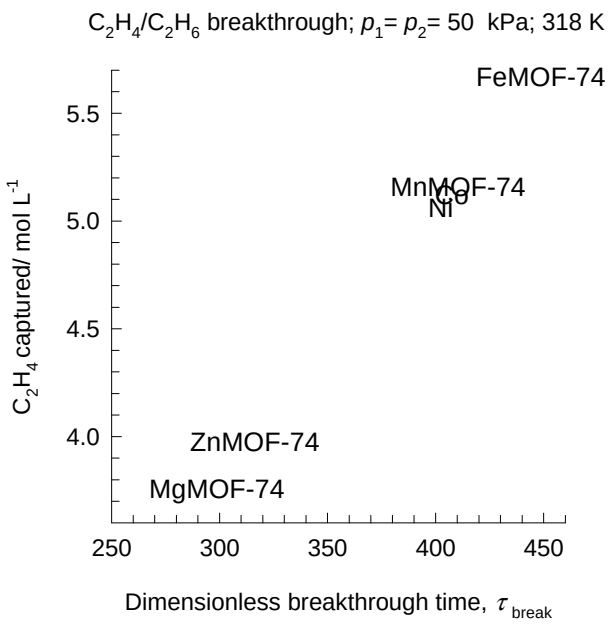

ESI Figure 12

C_3H_6/C_3H_8 separations for 50/50 mixtures

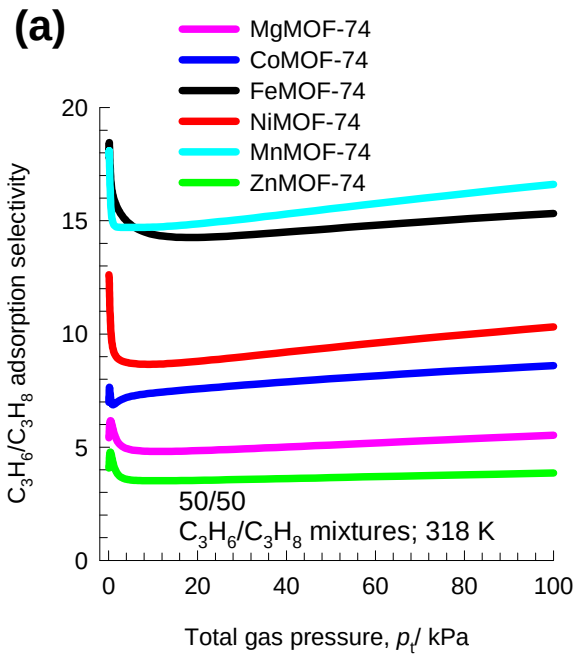

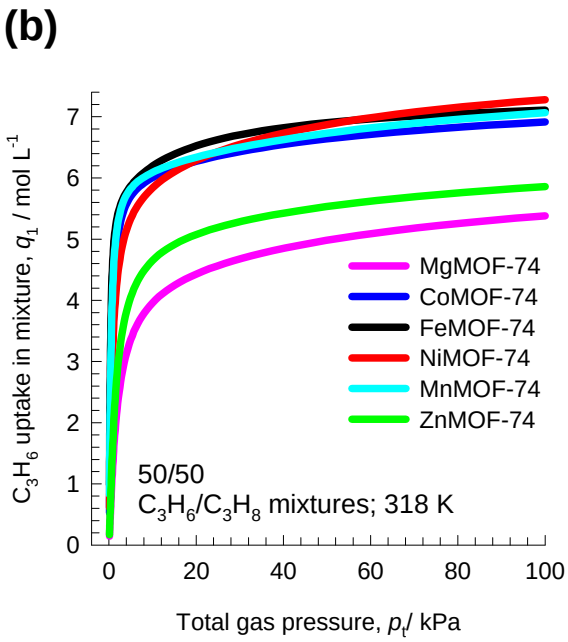

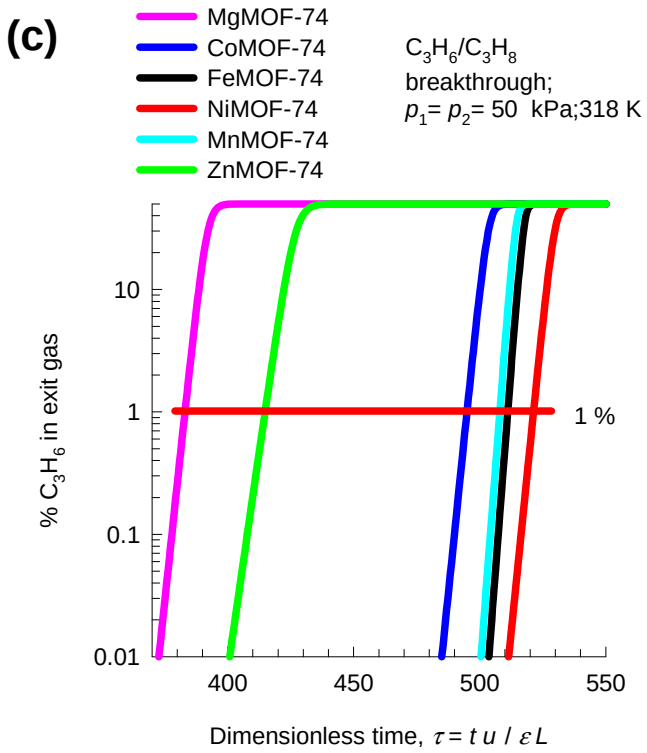

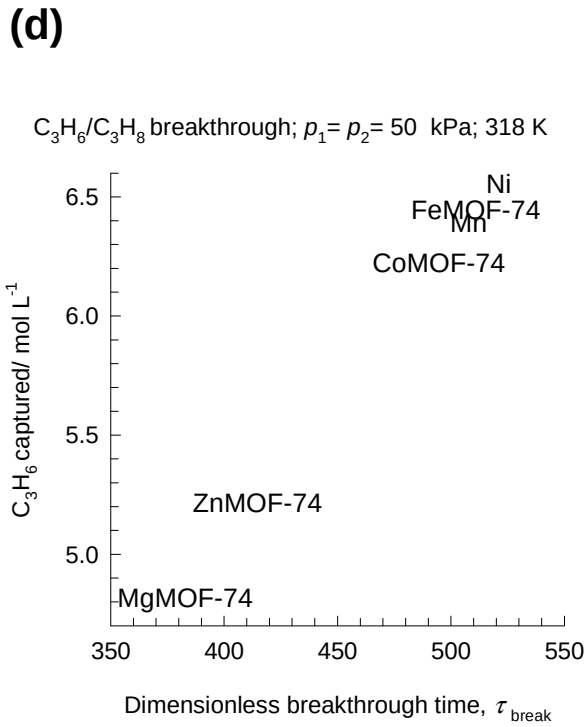

ESI Figure 13

Isosteric heats of adsorption for alkene/MOFs

(a)

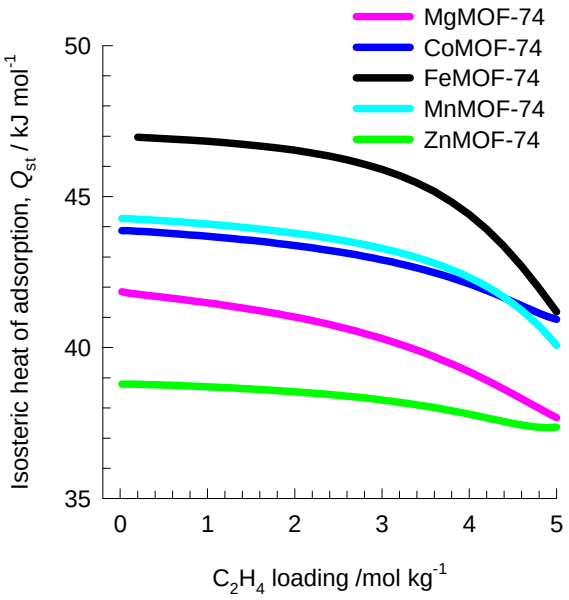

(b)

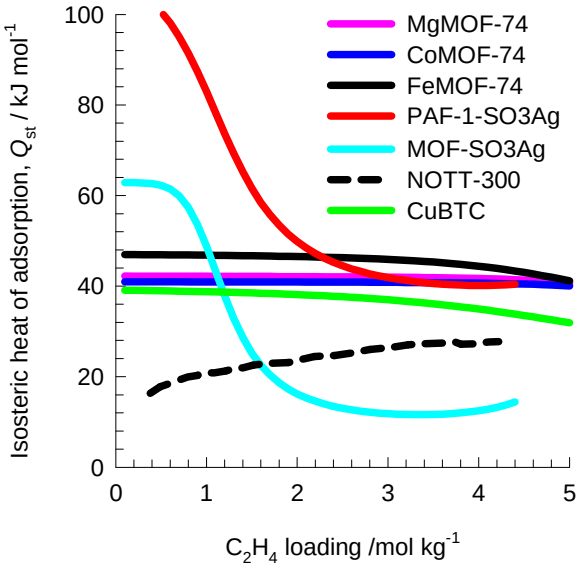

(c)

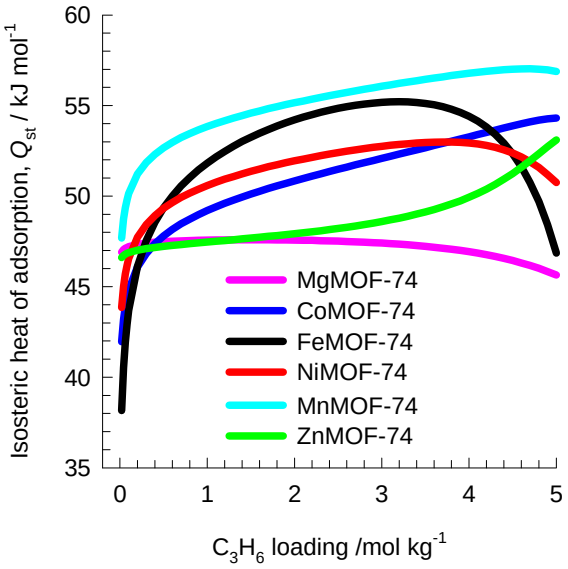

ESI Figure 14

Separations for hexane isomers

(a)

nC6-2MP-3MP-
22DMB-23DMB mixture;
Fe2(BDP)3; 433 K;
$f_1=f_2=f_3=f_4=f_5$ = 20 kPa;
with diffusion

(D_{nC6}/r_c^2) = 0.002 s^{-1}
(D_{nC6}/D_{2MP}) = 5
(D_{nC6}/D_{3MP}) = 5
(D_{nC6}/D_{22DMB}) = 10
(D_{nC6}/D_{23DMB}) = 10

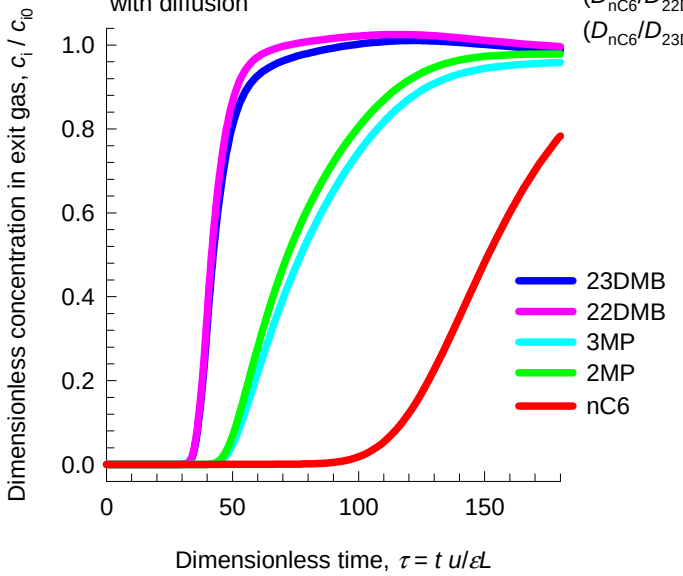

(b)

nC6-2MP-3MP-
22DMB-23DMB mixture;
ZIF-77; 433 K;
$f_1=f_2=f_3=f_4=f_5$ = 20 kPa

(D_{nC6}/r_c^2) = 0.0004 s^{-1}
(D_{nC6}/D_{2MP}) = 5
(D_{nC6}/D_{3MP}) = 5
(D_{nC6}/D_{22DMB}) = 10
(D_{nC6}/D_{23DMB}) = 10

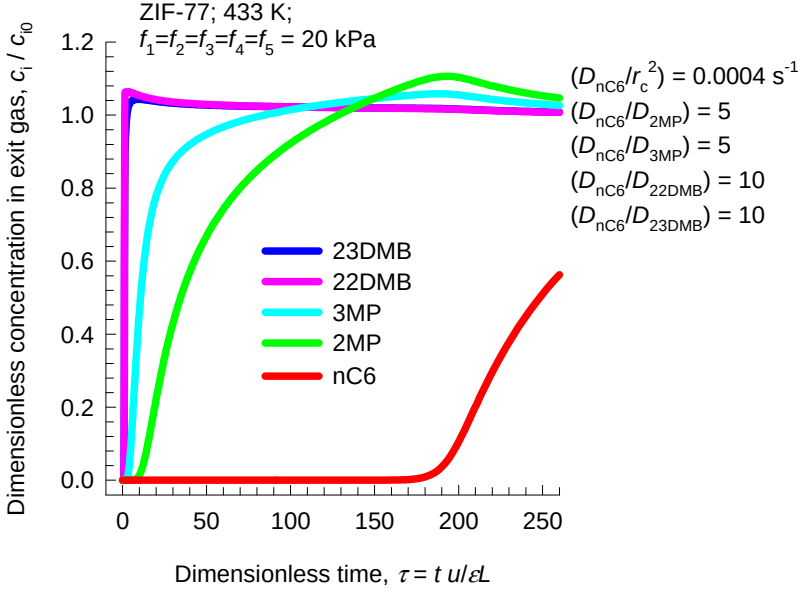

(c)

nC6-2MP-3MP-
22DMB-23DMB mixture;
MFI; 433 K;
$f_1=f_2=f_3=f_4=f_5$ = 20 kPa;
Including diffusion;
with thermo coupling

Dimensionless time, $\tau = t\,u/\varepsilon L$
(D_{nC6}/r_c^2) = 0.002 s^{-1};
(D_{nC6}/D_{2MP}) = 5
(D_{nC6}/D_{3MP}) = 5
(D_{nC6}/D_{22DMB}) = 25
(D_{nC6}/D_{23DMB}) = 25

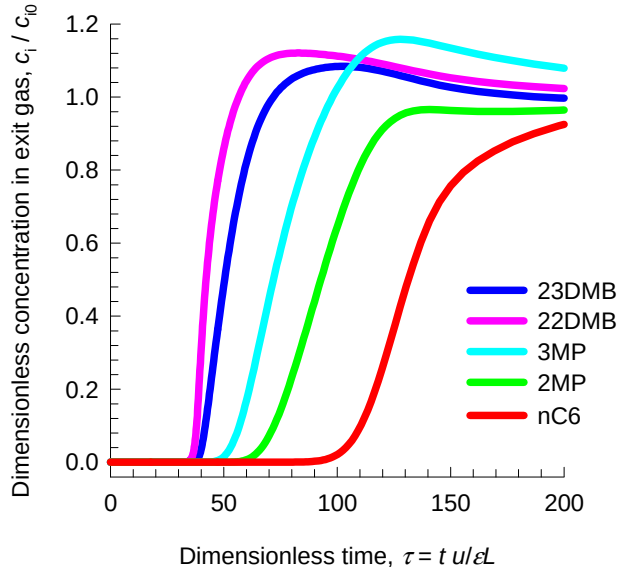

ESI Figure 15

Benzene, Cylcohexane structures

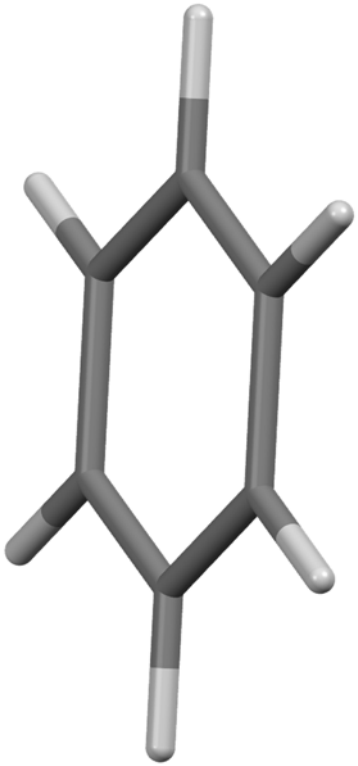

benzene

b.p.= 353.3 K

f.p. = 278.7 K

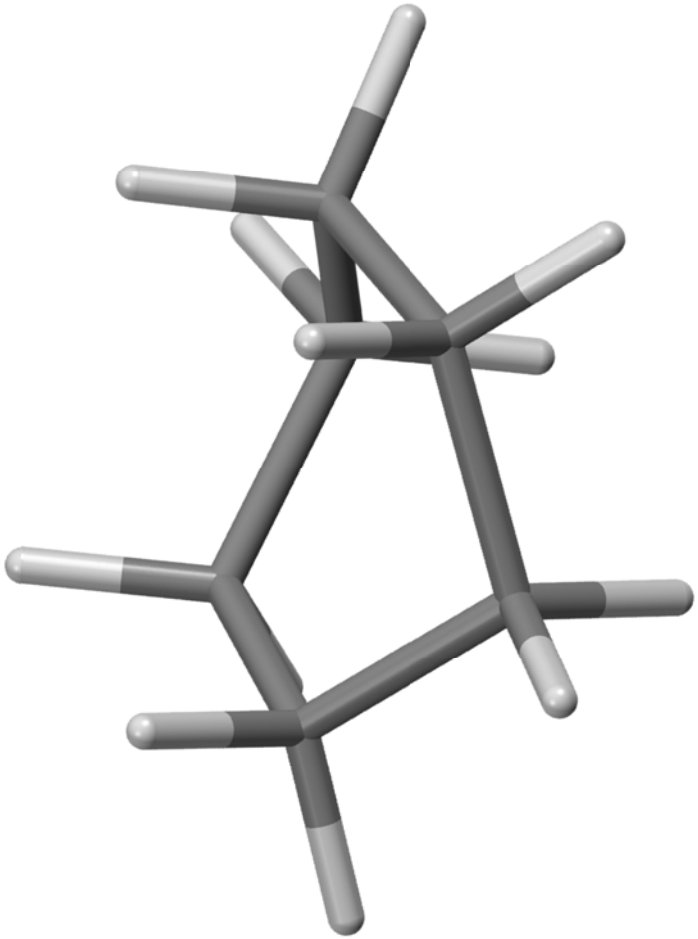

Cyclohexane boat

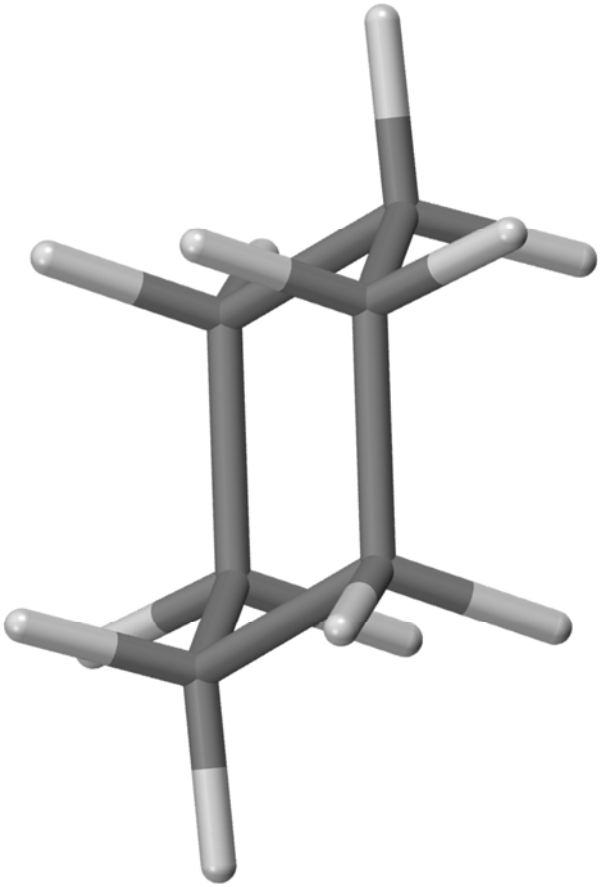

Cyclohexane chair

b.p.= 353.9 K

f.p. = 279.6 K

Benzene/Cylcohexane separations

(a)

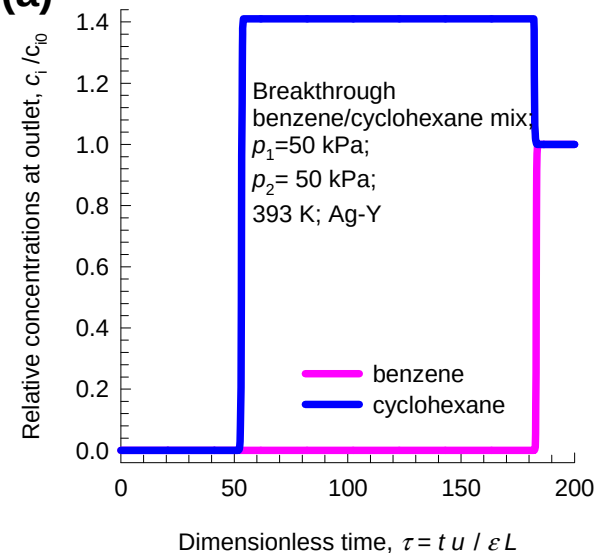

(b)

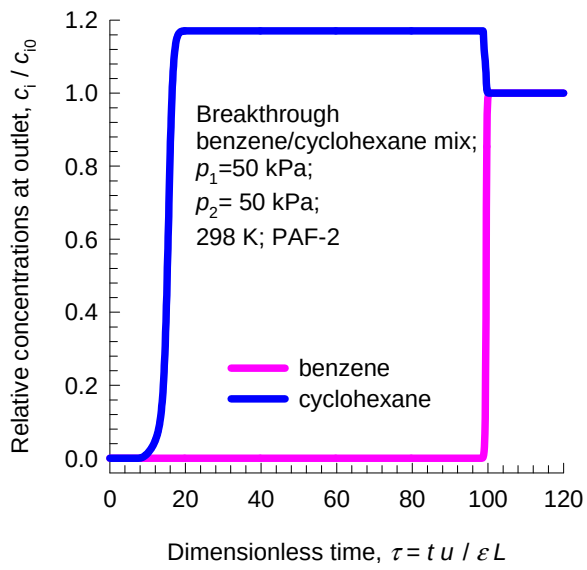

(c)